The Dissertation Committee for Tobias Fabian Bartsch
certifies that this is the approved version of the following dissertation:

Submicroscopic characterization of biopolymer networks in solution by Thermal Noise Imaging

Committee:

Ernst-Ludwig Florin, Supervisor

George Shubeita

Richard Aldrich

Alex Demkov

Manfred Fink

Submicroscopic characterization of biopolymer networks in solution by Thermal Noise Imaging

by

Tobias Fabian Bartsch, M.A.

DISSERTATION

Presented to the Faculty of the Graduate School of
The University of Texas at Austin
in Partial Fulfillment
of the Requirements
for the Degree of

DOCTOR OF PHILOSOPHY

THE UNIVERSITY OF TEXAS AT AUSTIN
May 2013

Dedicated to my parents.

I learned very early the difference between knowing the name of something and knowing something.

- Richard P. Feynman

Acknowledgments

I have never been afraid to take on the unknown, and in Dr. Florin I had an advisor who allowed and encouraged me to follow my own interests. I am very thankful for his friendship, his support, and his advice. Under his guidance I worked on challenging projects – some of which neither of us had much or any experience with. Especially from the latter I learned the most.

Much progress was made while working in collaboration with Martin Kochanczyk, who is both a brilliant scientist and one of my closest friends. I have known few people as reliable as Martin, and fewer still whose advice I value more. It is (almost) impossible to faze him, and I did my best to learn from his systematic and calm approach to science.

From the members of my Dissertation Committee I have received much support during my research. Dr. Shubeita has been a close collaborator on the work on lipid droplets. He was always available to help with words and deeds, and has given me valuable feedback on countless occasions. From Dr. Aldrich I have learned much about biology and interdisciplinary approaches to research. Through him I have become interested in neuroscience, a field of research I hope to pursue in the future. I highly value his advice and am thankful for his guidance. I am grateful to Dr. Demkov and Dr. Fink for insightful discussions of my research.

Rafael Longoria is a good friend with whom I worked on the molecular motor driven transport of lipid droplets. I am very grateful for the many evenings he stayed to purify lipid droplets and prepare the experimental assay. I greatly value his attention to detail in everything he does.

I am deeply thankful to the remaining members of the Florin lab – Avraham Be'er, Vassili Demergis, Michael Himmelsbach, Rongxin Huang, Katie Hinko, Janelle Korf, Chieze Ibeneche, Andrea Keidel, Emanuel Lissek, Gabriel Moreno, Katja Taute, and Pinyu Thrasher – and to all members of the Center for Nonlinear Dynamics for their support and for making me feel at home during the last years.

Janina Lange visited the Florin lab for one summer and showed me how to polymerize collagen networks. Her drive and motivation were missed when she returned to Germany. She remains a good friend and collaborator.

My high school physics teacher, Gerhard Motschmann, taught me to seek a deep understanding of physical phenomena. He inspired and encouraged me to study physics, and his impact on my chosen career cannot be overstated.

Finally, I thank my parents for their encouragement and guidance through my life. The most important lesson I learned from them is that anything can be achieved and nothing is too difficult when approached with enough motivation, creativity and self discipline. They shaped me into who I am, and without them this work would be impossible.

Submicroscopic characterization of biopolymer networks in solution by Thermal Noise Imaging

Publication No. ____________________

Tobias Fabian Bartsch, Ph.D.
The University of Texas at Austin, 2013

Supervisor: Ernst-Ludwig Florin

Biopolymer networks display a wide range of interesting mechanical properties that are essential for living organisms. For example, a highly nonlinear elastic response to strain gives biopolymer networks the ability to comply with small stresses but to resist large ones. These macroscopic mechanical properties have their origin in the properties of the individual filaments and their connectedness, like cross-linking geometry and pore size distribution. While the macroscopic properties of biopolymer networks have been extensively studied, there has been a lack of experimental techniques that can simultaneously determine mechanical and architectural properties of networks *in situ* with single filament resolution. This work introduces Thermal Noise Imaging (TNI) as a novel quantitative method to address these issues. TNI is a three-dimensional scanning probe technique that utilizes the confined thermal motion of an optically trapped particle as a three-dimensional, noninvasive scanner for soft, biological material. Using a photonic force microscope (PFM) custom built for this research, the position of the probe can be detected with nanometer precision and megahertz bandwidth. Two sets of single molecule experiments are described that demonstrate the microscope's exceptional precision and stability. Micrometer scale thermal noise images inside a collagen network are shown and quantitative information about cross-linking geometry is extracted from the data. Further, by imaging microtubules grafted to a support it is shown that the acquired data yield information about the transversal fluctuations of the imaged fibers and about fiber elasticity. These results pave the way for an investigation of force distributions inside biopolymer networks on the single filament level.

Table of Contents

List of Figures

Chapter 1

An introduction to networks of biopolymers

Networks made from biopolymers are materials with unique properties that play a major role in nature. Intracellular networks give cells mechanical stability, form tracks for molecular motor based transport, and generate force through polymerization [61, 62]. Fibers cross-linked by molecular motors form active gels whose mechanical properties depend on the state of the motor proteins [85].

Intracellular networks are mechanically coupled to extracellular networks (also called the "extracellular matrix"), allowing the transduction of mechanical signals between the extracellular space and the inside of each cell. By such mechanosensing, cells react to the stiffness of the substrate they grow on [27, 62]: For example, fibroblasts grown on collagen gels feature an irregular morphology and are highly motile compared to fibroblasts grown on solid substrates [97]. Brain and breast cancer cells can invade tissue depending on its mechanical properties rather than on chemical cues [68]. The mechanical properties of the extracellular matrix also facilitate cell-cell communication [108]: Contractile stresses exerted on the extracellular network by one cell can be sensed by other cells in its vicinity if the network is compliant enough, impacting their relative motility and facilitating the formation of cell-cell contacts.

It is therefore clear that the mechanical properties of biopolymer networks are important for diverse biological functions. A detailed understanding of the design principles of the networks is necessary to enable the creation of novel biomimetic materials, for example for the control of three-dimensional cell cultures. In the following the structure of intracellular and extracellular biopolymer networks is reviewed in more detail, and the essentials of their mechanics are discussed.

1.1 The cytoskeleton

The intracellular biopolymer network of a cell is called the cell's cytoskeleton (figure 1.1). Ordered by decreasing stiffness it consists of microtubules, actin filaments, and intermediate filaments [44, 67, 88, 95, 135]. The structures formed by each of these components are very diverse. Microtubules are hollow tubes which can be tens of microns in length, and have a high bending stiffness. Actin forms thin filaments with a helical structure which are usually cross-linked to a network best known for facilitating cell motility. Intermediate filaments form a variety of structures, from strong cytoplasmic cables that hold epithelial cell sheets together, to lining the inside of the nuclear envelope [1].

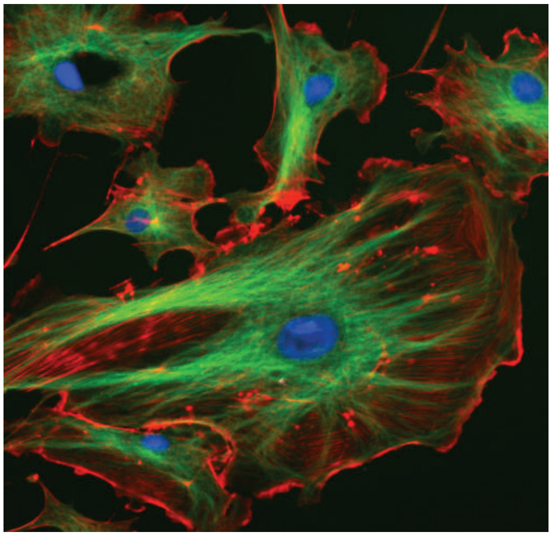

Figure 1.1: Fluorescently labeled cytoskeleton of a bovine pulmonary artery endothelial cell. Microtubules are shown in green, actin filaments in red, and nuclei in blue. This image was released by the NIH in the public domain, and can be found in the ImageJ Software Package [118].

1.1.1 Microtubules

Microtubules are made up of $9-16$ protofilaments that align to form a hollow cylinder with an inner diameter of $\sim$15 nm and an outer diameter of $\sim$25 nm, and can be several tens of micrometers long [95]. The protofilaments are made up of head-to-tail polymerized $\alpha\beta$-tubulin dimers, each 8 nm in length (figure 1.2). This gives microtubules an asymmetric structure: One end has β- and the other end α-tubulin exposed. Additional dimers can attach to both ends of the microtubule; however the attachment rate is much faster on the β-tubulin end. Thus, the microtubule grows almost exclusively from this end, and one typically refers to it as the “plus end” of the microtubule. The other slowly polymerizing end with exposed α-tubulin is called the “minus end”.

During interphase, the minus ends of microtubules are typically attached to

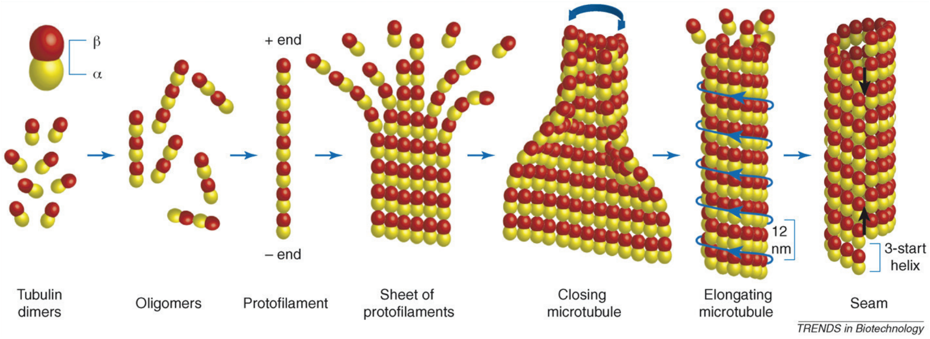

Figure 1.2: Polymerization of microtubules from $\alpha\beta$-tubulin dimers. $\alpha\beta$-tubulin dimers polymerize head-to-tail to form protofilaments, which then assemble into hollow cylinders. Reprinted with permission from [95].

the microtubule organizing center (MTOC) and their plus ends grow outwards towards the periphery of the cell (figure 1.1).

Microtubules feature an interesting dynamic instability [41]: On the time scale of seconds to minutes they switch back and forth between a state of elongation and a state of shrinkage. The rate of switching from growing to shrinking is called the “catastrophe” rate, while the rate of switching from shrinking to growing is the “rescue” rate. This instability can be understood on a molecular level (figure 1.3): For a microtubule to elongate, the β-tubulin of the attaching dimer has to be bound to guanosine triphosphate (GTP, purple β-tubulin in figure 1.3). Once the dimer has attached to the microtubule, its GTP hydrolyzes to guanosine diphosphate (GDP, green β-tubulin in figure 1.3) at a certain rate. Therefore, if the rate of attachment of new dimers is larger than the hydrolyzation rate, there is a cap of GTP bound dimers at the microtubule's end. GTP and GDP bound dimers attach to the protofilaments in slightly different orientations: While GTP bound dimers attach in a straight line, GDP bound dimers exposed at the microtubule's tip curl outwardly, which leads to catastrophe and shrinking. Therefore, as long as a GTP cap is present, the microtubule grows. If the GTP cap hydrolyzes to GDP, the protofilaments curl outwardly and the microtubule undergoes catastrophe. The catastrophe rate thus depends on the concentration of GTP bound $\alpha\beta$-tubulin dimers in solution, since this concentration determines whether GTP bound dimers bind to the microtubule quickly enough to sustain the GTP cap. The dynamic instability results in a cell's ability to rapidly reorganize its cytoskeleton [1], which is exploited by many biological functions [24].

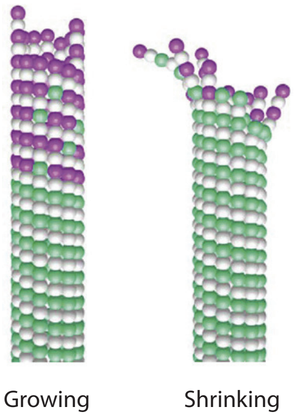

Figure 1.3: Dynamic instability of microtubules. Microtubules consist of α- (white) and β-tubulin dimers, where the β-tubulin can be either bound to GTP (purple), or after the GTP has been hydrolyzed, GDP (green). If the GTP in the microtubule's GTP cap hydrolyzes to GDP the microtubule undergoes catastrophe. Reprinted with permission from [41].

The dynamic instability can be suppressed by the drug taxol [3]. Taxol binds to the microtubule's inside, and counteracts the conformational change induced in the $\alpha\beta$-tubulin dimer by the hydrolysis of GTP. Taxol stabilized microtubules do not undergo catastrophe and only stop growing in the absence of GTP bound $\alpha\beta$-tubulin dimers.

Microtubules fulfill a diverse set of biological functions: Due to their stiffness (see chapter 5) they provide mechanical strength against compression or stretching of a cell [1]. During mitosis, microtubules of the mitotic spindle apparatus separate identical daughter chromosomes into two separate cells. The unidirectional molecular motors kinesin and dynein transport cargos by walking along microtubules, towards the microtubule's plus ended and minus ended directions respectively. During active cell migration, microtubules interact with the actin network (see section 1.1.2) to maintain the cell's polarization, i.e. to maintain the cell's protruding front and retracting rear [153]. Together with actin filaments, microtubules couple to the extracellular matrix (see section 1.2) and enable the transduction of mechanical signals between the inside of the cell and its outside [4, 61].

1.1.2 Actin filaments

Actin exists in two forms inside of eukaryotic cells, either as a monomer called G-actin, or as a polymer microfilament referred to as F-actin, which is mostly localized at the cortex of cells (figure 1.1, red filaments). F-actin has a diameter of approximately 8 nm [1] and individual filaments typically have a length of several micrometers [31]. While it has been known for many years that F-actin is a helical aggregate of G-actin [94], and models exist that explain this aggregation [1], the precise molecular mechanism by which G-actin polymerizes to F-actin had not been elucidated until recently: Cryo-EM data resolving the F-actin structure with a resolution of better than 5Å was reported by Murakami *et al.* in 2010, supporting the polymerization mechanism shown in figure 1.4 [89]. Adenosine triphosphate (ATP) bound G-actin (G-ATP-actin) nucleates, forming F-ATP-actin (white). This F-ATP-actin forms a nucleation site for further G-ATP-actin monomers. After an ATP bound G-actin monomer has been integrated into the filament, the bound ATP hydrolyzes to ADP, and the released phosphate group (Pi) is trapped in the F-actin lattice (F-ADP+Pi-actin, grey). After some time, the phosphate group is

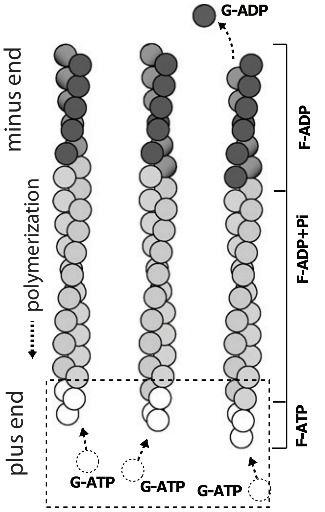

Figure 1.4: Polymerization of F-actin. See page 7 for a detailed description. Reprinted with permission from [89].

released from the filament, leaving F-ADP-actin subunits behind (dark grey). Thus, elongation mainly takes place at the F-ATP-actin end of the filament, which is therefore designated the plus end. The other end of the filament is called the minus end.

A host of at least 162 distinct proteins binds to actin filaments (actin binding proteins, ABPs) and can regulate the formation of networks. Several ABPs have been identified to cross-link actin, and link actin to microtubules and intermediate filaments. Others aid in actin attachment to membranes, in polymerization, depolymerization, branching, and so on [29].

Actin networks fulfill several important functions. The cortical actin network contributes to a cell's ability to withstand deformation [1]. Through focal adhesion complexes actin filaments are linked to the extracellular matrix, allowing the cell to control its movement by remodeling of its actin network [16], and sense the mechanical properties of its environment [27, 62]. Further, actin filaments serve as tracks for transport by motors of the myosin family. Actin filaments cross-linked to a network by myosin motors form active gels under the presence of ATP. The motors actively slide filaments against each other, thereby adjusting the mechanical properties of the network. This is the underlying mechanism for muscle contraction [58]. Such active networks have recently been found to violate the fluctuation-dissipation theorem of equilibrium statistical mechanics and are thus a convenient model system for networks far from equilibrium [85].

1.1.3 Intermediate filaments

While all eucaryotic cells contain microtubules and actin, intermediate filaments exist only in some animals (including all vertebrates). Not all metazoan cell types contain intermediate filaments though. They are however prevalent in all cells that must withstand large stresses [1]. Intermediate filaments are formed from a variety of related proteins, the most common being the family of keratins [1]. They have a diameter of approximately 10 nm, in between that of actin filaments and microtubules. Networks formed from intermediate filaments fulfill a diverse set of functions, such as contributing to the mechanical stability of sheets of epithelial cells, and lining the inside of the nuclear envelope of certain cell types.

1.2 Collagen and the extracellular matrix

Networks in a cell's extracellular space (the extracellular matrix, ECM) are made up of polysaccharides and the fibrous proteins collagen, elastin, laminin, and fibronectin. Collagen is the most abundant protein in animal tissues [25]. It provides the main biomechanical scaffold for cell attachment (figure 1.5), and by its mechanics influences the growth and fate of cells [4, 62]. Elastin forms networks responsible for tissue extensibility and elastic recoil. It is in part responsible for the elastic properties of animal skin and arterial blood vessels, is mechanically resilient and can sustain billions of cycles of elastic extension and contraction [69]. Laminin and fibronectin are associated with basement membranes [136].

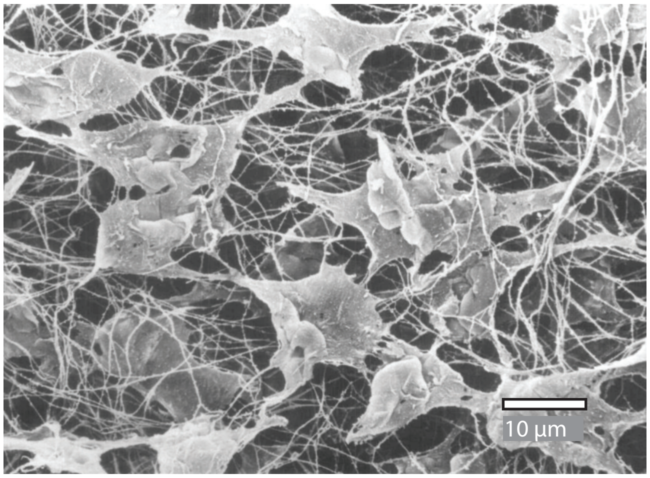

Figure 1.5: Connective tissue of the cornea of a rat. A scanning electron microscopy image of corneal fibroblasts attached to their extracellular matrix is shown. The visible fibers are made up of collagen. Reprinted with permission from [93].

In this work we will focus on collagen [66], whose structure is discussed in the following. A single collagen molecule is made up of a triple helix of polypeptide chains (α-chains), with a length of 300 nm and a diameter of 1.5 nm (figure 1.6). Over 20 genetically different forms of collagen exist, and most is known about collagen type I which is predominantly found in tendons and skin. Collagen type I molecules, on which we will focus in this work, self-assemble into cross-striated fibrils, with a repeat periodicity of $D = 67$ nm (see figure 1.6). Their N- and C-telopeptides are important for this assembly: Molecules typically align end to end, giving a collagen fibril an N and a C end (unidirectional fibril). Fibrils with two N ends can also form under certain conditions (bidirectional fibrils); in this case the alignment direction of the molecules switches somewhere along the fibril. Molecules without telopeptides

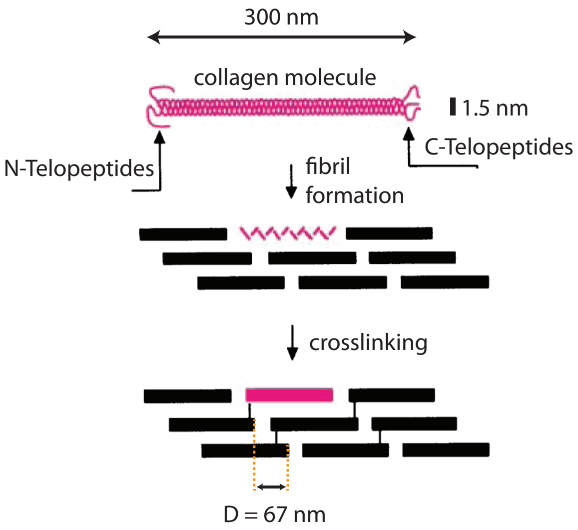

Figure 1.6: Synthesis of collagen fibrils. Collagen molecules spontaneously self-assemble into cross-striated fibrils, which *in vivo* are stabilized by covalent cross-linking. Reprinted from [66].

do not form filaments. Partial loss of the telopeptides impacts fibril diameter uniformity and loss of unidirectional packing of the molecules in the fibril. *In vivo*, the molecules within the fibrils are typically cross-linked biochemically [35]. During polymerization fibrils rapidly reach a maximum diameter, and then only grow at their ends [65, 66]. Fibrils that have reached their maximum diameter will be referred to as "mature". Several fibrils bundled together form higher order structures called "collagen fibers" [42].

For *in vitro* experiments, collagen molecules are typically extracted from tissue into cold dilute acidic solutions. In order to start polymerization *in vitro*, the solution is neutralized, and its temperature raised in between room temperature and 39 °C. The order in which the temperature is raised and the solution is neutralized has an impact on the structure of early fibrils [55]: If the solution is neutralized after raising the temperature, early aggregates are banded with a periodicity of $D = 67$ nm. However, if neutralization occurs in the cold, early aggregates do not show any bands. Either pathway results in cross-striated mature fibrils. Whether this difference in fibril assembly has any impact on the mechanics of the mature fibrils is not known to the author's knowledge. Fibrils polymerized from acidic solutions are typically unidirectional [66].

The ensemble of polymerized collagen fibrils and subsequently formed fibers form a network. Junctions in this network may be given by two filaments that are in contact but free to slide against each other, or by a collagen fiber that branches into individual fibrils [12].

The mean diameter of mature collagen type I fibrils depends on temperature, ionic strength and pH during polymerization, and can be adjusted between approximately 50 nm and 200 nm [154]. A change in the concentration of collagen molecules in solution during fibril assembly has little impact on the resulting mean fibril diameter. Rather, with increasing concentration of collagen, more fibrils are polymerized and the pore size of the formed network decreases, from $\sim 3\,\mu$m at a concentration of 1.2 mg/ml, to $\sim 1.3\,\mu$m at 2.4 mg/ml [84].

Collagen type V fibrils are much thinner (mean diameter 25 nm at a polymerization temperature of 37 °C) than fibrils made up of collagen type I, and non-striated in appearance. Fibrils can be formed from a mixture of type

I and type V collagen molecules, and their diameter can be tuned by adjusting the relative concentrations of the two collagen types during polymerization [11].

1.3 Mechanical properties

Above we have seen that the mechanical properties of biopolymer networks are important for many different biological functions. This has generated interest in understanding their mechanics in detail, and in this section we will review some of what is known.

Biopolymer networks in nature are heterogenous on several different length scales, which makes their study *in vivo* very challenging. A way to resolve this problem is to isolate functional modules from living cells, and reconstitute them *in vitro* [8], or to build *in vitro* model systems from scratch [85]. The mechanics of the networks can then be probed.

1.3.1 Strain hardening

An important mechanical property of a biopolymer network is its elasticity, which can be studied by rheology. The networks are sheared by a strain γ applied either as a static or as an oscillatory deformation. From the static experiment the shear modulus G, and from the oscillatory experiment the storage modulus G' is extracted. The relationship between applied strain γ and shear or storage modulus is shown in figure 1.7 for a variety of biopolymer networks and, as a control, of a polyacrylamide network. Evidently, polyacry-

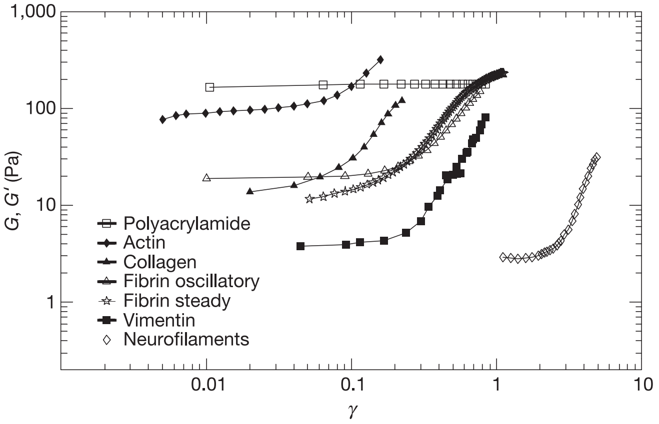

Figure 1.7: Shear moduli (G) for fibrin and neurofilaments, and storage moduli (G') for F-actin, fibrin, collagen, vimentin and polyacrylamide as a function of applied strain γ. Reprinted with permission from [132].

lamide networks behave like Hookean springs: Over the explored strain regime their storage modulus is a constant. The moduli of all other networks increase nonlinearly with increasing strain, a feature commonly referred to as "strain hardening". For example, strain hardening of the collagen network underlying the epithelial layer of skin allows compliance with small stresses to enable the unconstrained motion of joints, but resists large deformations so that skin does not easily tear apart. Strain hardening has its origin in the properties of the individual filaments of the network, and in their fashion and degree of connectedness.

1.3.2 The persistence length

The stiffness of an individual filament in a solution can be described by its persistence length l_p [115, 157]. It defines the distance over which the

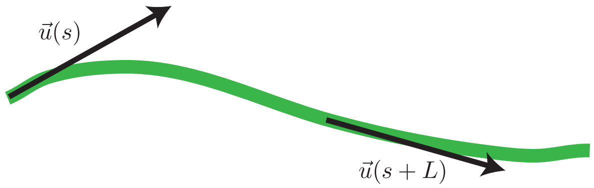

Figure 1.8: Geometry for the decay of tangent-tangent correlations along a fluctuating filament.

tangent-tangent correlation along a fluctuating filament decays away (figure 1.8), i.e.

$$\langle \vec{u}(s)\vec{u}(s+L)\rangle = \mathrm{e}^{-\frac{L}{l_p}}, \tag{1.1}$$

where $\vec{u}(s)$ is the tangent vector at position s of the filament's contour, and L is the distance along the contour between two such vectors. The persistence length is related to the flexural rigidity κ of the filament by [96]

$$l_p = \frac{\kappa}{k_B T}, \tag{1.2}$$

thus describing the combined effect of thermal and mechanical forces on the filament's fluctuations.

Filaments can be grouped into three different classes based on the ratio of their persistence to their contour length [67]. If the filament's persistence length is much larger than its contour length ($l_p \gg l_c$) then the filament is called "stiff" and can often be modeled as a stiff rod. Collagen type I fibrils (section 1.2) are an example of this regime [158]. Filaments that have comparable persistence and contour lengths ($l_p \approx l_c$) are referred to as "semi-flexible". Many biopolymers fall into this regime, with actin filaments (section 1.1.2) being a prominent example [67]. Finally, if the persistence length is much smaller than the contour length ($l_p \ll l_c$) the filament is called “flexible”. DNA can to a certain extent be treated as flexible [128].

We will now take a closer look at the mechanics of semi-flexible polymers.

1.3.3 Lateral fluctuations and end-to-end distance distribution

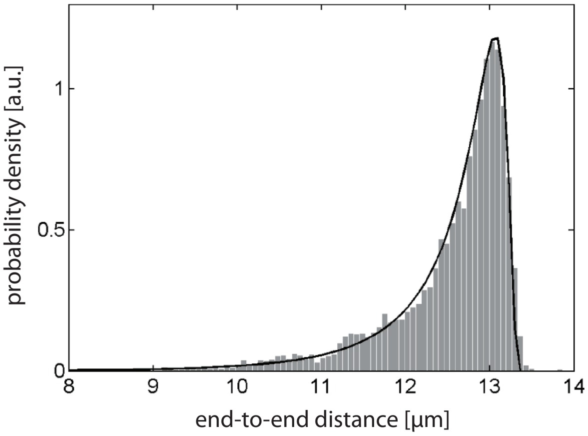

Figure 1.9: End-to-end distance distribution of a fluctuating actin filament with contour length $l_c = 13.4\,\mu$m and persistence length $l_p = 16.1\,\mu$m. This figure copyright 2002 by The American Physical Society. Reprinted with permission from [73].

A semi-flexible polymer in aqueous solution responds to thermal forces, which strive to bend the filament transversally, in competition with elastic forces, which attempt to straighten the filament. Therefore the filament’s end-to-end distance r, defined as the length of the straight line connecting the filament’s end points, is distributed around a most probable end-to-end distance r_0, which is shorter than its full contour length. The distribution of r can be computed for a given ratio of l_c/l_p [151], and agrees well with experimental results on actin filaments (figure 1.9 and ref. [73]). Boltzmann statistics can be used to convert this distribution to an energy landscape with an energy minimum located at r_0. Thus, for small extensions (or compressions) from this distance, there are restoring entropic forces and the filament acts as an entropic spring. For large extensions, when the transversal fluctuations are smoothed out and $r \approx l_c$, the bonds between the subunits of the filament begin to stretch, and the much stronger enthalpic response of the filament dominates. Thus semi-flexible filaments in a solution behave inherently non-linear: The response to small strains is entropic, and the filament easily complies. For large strains, the response becomes enthalpic, and stretching the filament becomes much harder.

It is important to emphasize that there is a relation between the filament's transversal fluctuations and its tension: The larger the tension that acts on the filament, the larger its end-to-end distance, and the smaller its transversal fluctuations. The magnitude of the transversal fluctuations thus can be used as a probe for the forces acting on the filament. A measurement of the transversal fluctuations of a semi-flexible biofilament constitutes a measurement of its tension.

1.3.4 Force distribution in networks of semi-flexible biopolymers

We will now consider a network of semi-flexible filaments, cross-linked in a random fashion, and attempt to motivate how the macroscopic properties of the network can arise from the properties of the single filaments. Assume that the network is at equilibrium, meaning that the position of junctions in the network are stationary[1]. The straight line distance between two adjacent junctions confines the filament between them to a fixed end-to-end distance r, which may be shorter or longer than the most probable end-to-end distance r_0 of this filament (see section 1.3.3). Thus, the entire network can be approximated as a network of pre-stretched (and pre-compressed) entropic springs [132], and each filament applies an entropic force on the junctions it is connected to. This force is contractive if $r > r_0$, or expansive if $r < r_0$. The forces on each junction are balanced, i.e. their sum is zero; otherwise the junction would not be at rest. In other words, there is a distribution of expansive and contractive forces acting on the filaments, and therefore on the junctions inside a network of semi-flexible filaments. Depending on the stiffness of the filaments, bending elasticity may also contribute to the force distribution in the network. In addition to the distance between junctions and bending elasticity, the forces are also expected to be influenced by local network architecture, like the cross-linking angle between filaments, and the stiffness of these cross-links, i.e. how easily they deform under an applied load.

The force distribution governs the macroscopic response of the network: An externally applied macroscopic load propagates along filaments and junctions through the network, smoothes out (or increases) the transversal

---

[1] There are, of course, thermal forces acting on each junction, resulting in small random extensions from its equilibrium position.

fluctuations of the individual filaments, or, more abstractly, stretches (or compresses) the entropic springs in the network, and deforms junctions. For large macroscopic strains, the enthalphic elasticity of each filament begins to dominate.

A recent theoretical model predicting the stress-strain relation of semiflexible biopolymer networks [132] takes their force distributions into account, and agrees well with the observed strain hardening behavior (section 1.3.1). Other models have focused on networks of stiff polymers and have found that details of the network architecture influence macroscopic properties [54, 152]. In order to validate these models, local network architecture such as a single junction must be imaged, and simultaneously the forces acting on the individual filaments connected to the junction must be measured. The architecture of junctions in a network is below the resolution limit of traditional light microscopy. Thus, gaining a detailed understanding of local network architecture requires three-dimensional super resolution imaging, such as 3D STORM [156], 3D STED [49], or electron microscopy. However, STORM and STED require integration times on the order of seconds for each acquired image frame, and cannot resolve the transversal fluctuations of a biopolymer filament. Thus, they cannot exploit the link between transversal fluctuations and tension as discussed above, and cannot measure the forces acting on individual filaments. Electron microscopy cannot be used to image biological material under physiological conditions, and the involved sample preparation procedures can shrink biopolymer networks to 70% of their original size [32], thus obviously altering their structure. A novel approach to imaging biopolymer networks is therefore necessary.

1.4 Research objectives and dissertation outline

It is the goal of this research to implement and build upon a recently introduced three-dimensional scanning probe technique called thermal noise imaging [137]. It will be demonstrated that thermal noise imaging can image the local network architecture of a biopolymer network under physiological conditions with super resolution, and that this technique can simultaneously measure the transversal fluctuations of the involved filaments, which are directly related to their tension (see section 1.3.3) and thus to the local force distribution in the network.

Thermal noise imaging relies on the high bandwidth and high precision tracking of a small colloidal particle using a photonic force microscope which was constructed for this research. Chapter 2 discusses various theoretical aspects necessary to understand photonic force microscopy and characterizes the microscope used in this work. It also introduces thermal noise imaging as a quantitative scanning probe technique. Chapters 3 and 4 detail initial experiments that demonstrate the stability of the microscope. The exceptional position detection precision and bandwidth are used to follow the formation of individual molecular bonds between two surfaces (chapter 3) and to study the transport of cargos by endogenous motor-cargo complexes along microtubules (chapter 4). Chapters 5 and 6 then describe thermal noise imaging experiments. First, we will discuss thermal noise imaging of grafted microtubules, and then elucidate the extraction of transversal fluctuations from the acquired images (chapter 5). This paves the way for the imaging of the local network architecture of collagen gels (chapter 6). Finally, this work concludes with an outlook on possible future experiments (chapter 7).

Chapter 2

The photonic force microscope

All experiments described in this dissertation utilized a custom built photonic force microscope (PFM). A PFM consists of an optical trap (section 2.1) which confines the Brownian motion (section 2.2) of a dielectric nanoparticle to a small volume, coupled to a three-dimensional position detector, which can measure the position of the trapped particle relative to the center of the optical trap. The detector used in this work (section 2.3) has a bandwidth of $\sim$1 MHz and can detect the particle's position with nanometer spatial resolution. The diffusing particle acts as a soft three-dimensional scanning probe, which can be used to investigate diverse phenomena, such as the elasticity of the molecular motors kinesin [64] and myosin [120], the local viscosity in a solution close to a boundary [100], and lipid rafts in the membranes of living cells [101]. Similar to imaging two-dimensional topologies with an atomic force microscope (AFM), the three-dimensionally diffusing probe can also be used to create three-dimensional images of scanned structures. Since the probe is driven by thermal motion, this imaging technique is called thermal noise imaging (section 2.4).

2.1 Optical tweezers

Stable confinement of dielectric nano-particles in the focus of a laser beam was first demonstrated by Ashkin *et al.* in 1986 [6]. Ashkin and coworkers showed that this single beam optical trap (optical tweezers) could confine particles ranging in diameter from $\sim$10 μm down to $\sim$25 nm, covering the regime of geometrical optics (particle radius $a \gg \lambda$, which is the wavelength of the trapping laser), the Mie regime ($a \approx \lambda$) and the Rayleigh regime ($a \ll \lambda$). In order to form a stable trap the refractive index of the particle n_1 must be sufficiently larger than the refractive index of the surrounding medium n_2.

For the geometrical optics regime one can consider the refraction of each individual light ray of the trapping beam as it passes through the trapped particle [5, 6]. Upon refraction, momentum is transferred from the ray to the particle, leading to a force on the particle. This force can be decomposed into two components [5]: The gradient force, acting perpendicularly to the light ray, and the typically much weaker scattering force, acting along the ray. For each of these forces one sums over all light rays in the beam, yielding the total gradient and scattering force respectively. For any arbitrary displacement of the particle from the focus of the beam, the gradient force drives the particle back into the direction of the focus. The scattering force, on the other hand, pushes the particle into the propagation direction of the beam, causing the equilibrium position of the particle to be not exactly at the focus, but slightly behind it.

In the Rayleigh regime, since $a \ll \lambda$, the particle may be treated as a point object with an induced dipole moment (see for example [51]). The induced dipole moment of such a particle with refractive index n_1, in a medium with refractive index n_2, in an electric field $\boldsymbol{E}(\boldsymbol{r}, t)$ is given by

$$\boldsymbol{p}(\boldsymbol{r}, t) = 4\pi n_2^2 \epsilon_0 a^3 \left(\frac{m^2 - 1}{m^2 + 2} \right) \boldsymbol{E}(\boldsymbol{r}, t), \tag{2.1}$$

where $m = \frac{n_1}{n_2}$, $m > 1$, ϵ_0 is the vacuum permittivity, and $\boldsymbol{r} = (x, y, z)$ is the position vector of the particle. The resulting force on the dipole can again be decomposed into a scattering force and a gradient force. Scattering of the incoming trapping beam on the dipole leads to a momentum transfer which pushes the particle along the propagation direction of the beam. This scattering force can be shown to equal

$$\boldsymbol{F_{scat}}(\boldsymbol{r}) = \frac{n_2}{c} \frac{8}{3} \pi \left(ka \right)^4 a^2 \left(\frac{m^2 - 1}{m^2 + 2} \right)^2 |\boldsymbol{E}(\boldsymbol{r}, t)|^2 \boldsymbol{e_z} \tag{2.2}$$

where c is the speed of light in vacuum, $k = \frac{2\pi}{\lambda}$ is the wavenumber of the trapping beam and $\boldsymbol{e_z}$ is the unit vector in z direction which coincides with the optical axis of the system. The gradient force, which pushes the dipole towards the focus of the beam, follows immediately from the fact that an electric dipole in an inhomogeneous electric field feels an average force given by [23, 51]

$$\begin{aligned} \boldsymbol{F_{grad}}(\boldsymbol{r}) = \langle \boldsymbol{F_{grad}}(\boldsymbol{r}, t) \rangle_T &= \langle [\boldsymbol{p}(\boldsymbol{r}, t) \cdot \nabla] \boldsymbol{E}(\boldsymbol{r}, t) \rangle_T & (2.3) \\ &= \pi n_2^2 \epsilon_0 a^3 \left(\frac{m^2 - 1}{m^2 + 2} \right) \nabla |\boldsymbol{E}(\boldsymbol{r})|^2 & (2.4) \\ &= \frac{2\pi n_2 a^3}{c} \left(\frac{m^2 - 1}{m^2 + 2} \right) \nabla I(\boldsymbol{r}) & (2.5) \end{aligned}$$

where it was used that the intensity I is related to the electric field E by [23]

$$I(\boldsymbol{r}) = \frac{1}{2} n c \epsilon_0 |\boldsymbol{E}(\boldsymbol{r})|^2 \tag{2.6}$$

Finally, for the Mie regime ($a \approx \lambda$), calculating the scattering and gradient force is challenging, but can be achieved by use of the Maxwell stress tensor [40, 60, 111, 112, 114].

In general, if the gradient force is smaller than the scattering force, the particle cannot be stably trapped. High numerical aperture (NA) lenses by definition yield many light rays that intersect the focus at steep angles, and contribute a large gradient force but only a small scattering force to the full optical force on the particle. In contrast, low NA lenses intersect the focus at a shallow angle, and contribute large components to the scattering force. Therefore, to create a stable single beam optical trap, a lens with as high a NA as possible must be used.

For the Rayleigh and Mie regime, the scattering as well as the gradient force can only be computed if the intensity distribution at the focus of the beam is known. Richards and Wolf showed in a seminal paper [109] that this distribution equals an Airy pattern for lenses with very small numerical apertures (NA → 0), but deforms drastically if the numerical aperture increases (see figure 2.1). As pointed out above, to minimize the scattering force, a high NA lens is necessary for stable confinement of a particle with optical tweezers. For such a lens the central intensity maximum stretches in direction of polarization of the incoming beam compared to the original Airy pattern.

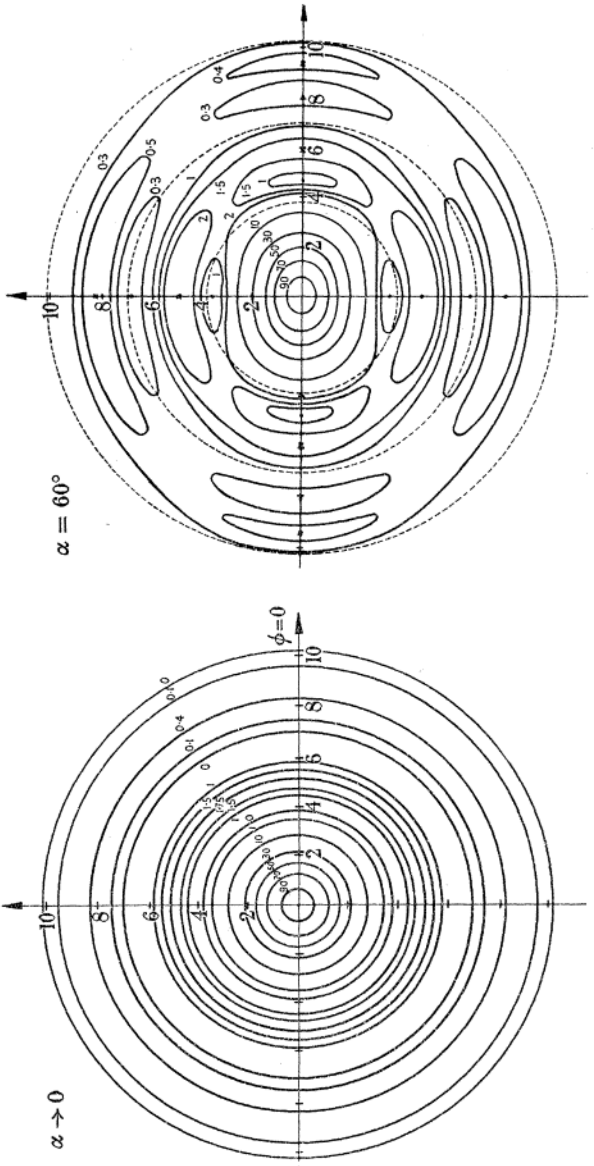

Figure 2.1: Schematic of the intensity distribution perpendicular to the optical axis at the focus of an aplanatic lens, for two different angular semi apertures ($\alpha = 0$ and $\alpha = 60°$), and thus different NAs. The direction of polarization of the incoming beam is along the x-axis ($\phi = 0$). Axes have arbitrary units. Reprinted with permission from [109].

In this study, particles with radius $a \leq \lambda$ were used; these particles fall into the Mie regime. Rohrbach and Stelzer's derivation for the Mie regime [112, 114] shows that the gradient force increases linearly with small displacements of the trapped particle from its equilibrium position, implying a three-dimensional harmonic trapping potential

$$E_{\text{trap}}(\boldsymbol{r}) = \frac{1}{2}(k_x x^2 + k_y y^2 + k_z z^2). \tag{2.7}$$

Of the three spring constants (k_x, k_y, k_z) defining this potential, the spring constant along the optical axis (z-axis) is the weakest. The lateral spring constants are larger, but not, as one might naively assume, equal. The rotational symmetry along the optical axis is broken by the direction of polarization of the incoming laser beam, and the lateral spring constant along this direction is weaker than the one perpendicular to the direction of polarization. We may get some intuition for this effect by inspecting, for simplicity and as a crude approximation, equation 2.5 which was derived for the Rayleigh regime instead of analyzing the much more complicated theory for the Mie regime. Assuming that the central intensity maximum of the focal region of the laser beam can be approximated by a Gaussian distribution with half width σ_α along each of the three axes ($\alpha = x, y, z$) of the system, we have for the components of the gradient force along these axes:

$$\begin{aligned} F_{grad,\alpha} \propto \frac{\partial}{\partial \alpha} \mathrm{e}^{-\alpha^2/2\sigma_\alpha^2} &= -\frac{1}{\sigma_\alpha^2} \alpha \mathrm{e}^{-\alpha^2/2\sigma_\alpha^2} && (2.8) \\ &\approx -\frac{1}{\sigma_\alpha^2} \alpha && (2.9) \end{aligned}$$

where approximation 2.9 is valid for small displacements α from the focus. The spring constant of the confining potential is therefore inversely proportional to σ_α^2:

$$k_\alpha \propto \frac{1}{\sigma_\alpha^2} \tag{2.10}$$

Thus, since for a high NA lens the central intensity maximum is stretched in the polarization direction of the incoming beam, the lateral spring constant along this direction is weaker than the one perpendicular to it.

It is very challenging to compute the precise spring constants for a given photonic force microscope from first principles. However, in practice the spring constants can be extracted from the spatial probability density of the trapped particle (see section 2.2.5), and thus their *ab initio* calculation is unnecessary.

2.2 Confined Brownian Motion

Consider now a particle in an aqueous medium of viscosity η confined in a harmonic potential as given by equation 2.7. This particle collides with on the order of 10^{21} individual fluid molecules per second [18], which results on long time scales in a random walk of the particle *within the optical trap* (confined Brownian Motion). On very short time scales ($\Delta t \ll 10^{-7}$s) each collision with a cluster of fluid molecules gives the particle a "kick", resulting in ballistic motion of the particle, until it collides with other fluid molecules. It is then slowed down again, and its new subsequent direction of motion and velocity are randomized [57]. These "kicks" are what make up the thermal force $\boldsymbol{F_{th}}$ acting on the particle. In this work, particle positions were sampled at 100 kHz ($\Delta t = 10^{-5}$s), more than two orders of magnitude greater than the ballistic regime of motion. Therefore, we need not concern ourselves with this regime here, and may assume that subsequent particle displacements $\Delta \boldsymbol{r} = \boldsymbol{r}(t+\Delta t) - \boldsymbol{r}(t)$ are to a first approximation independent, and that there is no correlation in the magnitude and direction of $\boldsymbol{F_{th}}(t)$ and $\boldsymbol{F_{th}}(t+\Delta t)$. Further, we may assume that $\boldsymbol{F_{th}}(t)$ is a white noise Gaussian process, sufficiently defined by its moments [10, 141, 146]:

$$\begin{aligned} \langle F_{th}(t) \rangle_{F_{th}} &= 0, && (2.11) \\ \langle F_{th}(t_1) F_{th}(t_2) \rangle_{F_{th}} &= g\delta(t_1 - t_2) && (2.12) \end{aligned}$$

where g is a measure for the strength of the fluctuating thermal force. It can be shown that $g = 2\gamma_0 k_B T$ by the fluctuation-dissipation theorem; $\gamma_0 = 6\pi\eta a$ is the viscous drag on the particle, and T is the temperature. The correlation 2.12 is related to the power spectral density of the thermal force [72, 146], which in this case is constant, as expected for white noise:

$$\mathrm{PSD}_{F_{th}}(f) = 2g \tag{2.13}$$

For sufficiently long time scales, we may then write down the equation of motion for a particle confined in a harmonic potential. We will consider the one dimensional case along the x-axis; identical equations exist for the y and z direction:

$$m\ddot{x} = -\gamma_0 \dot{x} - kx + F_{th}(t) \tag{2.14}$$

This equation is called the Langevin equation [107]. m is the mass of the particle, and k is the spring constant of the confining potential. The left hand side of equation 2.14 is the inertial force on the particle; the terms on the right hand side are the frictional force, potential force, and the fluctuating thermal force respectively. For now, as a first approximation, we have ignored the inertia of the surrounding fluid in this equation. The full hydrodynamic theory is discussed in section 2.2.3. Since we are considering time scales at which the inertial energy of the particle has long been dissipated by friction (the system is over-damped), we may approximate the left hand side of equation 2.14 as zero, thus

$$\gamma_0 \dot{x} + kx - F_{th}(t) = 0. \tag{2.15}$$

Obviously, this equation cannot be integrated and solved analytically due to the randomly fluctuating thermal force term. However, as shown below, we can compute several statistical quantities, such as the mean squared displacement of the particle from the center of the trap, the power spectral density of the motion of the confined particle, and the probability distribution of particle positions.

2.2.1 Mean squared displacement

The mean squared displacement (MSD) of a diffusing particle is a useful statistical quantity: It describes how the variance of the particle's displacement evolves with time. Starting with the Langevin equation (equation 2.14) an expression for the MSD of a free particle ($k = 0$) can be derived (see for example [107]). One finds for the one dimensional case

$$\langle x^2 \rangle_{\text{free}}(t) = 2Dt, \tag{2.16}$$

where $D = k_B T/\gamma_0$ is called the diffusion constant. Thus, the MSD of a freely diffusing particle increases linearly with time.

Consider now a trapped particle confined in a harmonic potential. It is intuitively clear, that in this case the MSD cannot grow unbounded for large t. The particle is confined by the trap and displacements far away from its center are statistically negligible. One therefore expects the MSD in this case to plateau above a characteristic time τ.

The MSD for such a confined particle is given by [141] as

$$\langle x^2 \rangle_{\text{confined}}(t) = \frac{k_B T}{k} \left(1 - \mathrm{e}^{-2\frac{k}{\gamma_0}t}\right), \tag{2.17}$$

which for short time scales simplifies to equation 2.16, and has a plateau at $\frac{k_B T}{k}$ for times much larger than

$$\tau = \frac{\gamma_0}{k}. \tag{2.18}$$

τ is called the position autocorrelation time of the trap. Particle position measurements separated by a time $\Delta t > \tau$ are uncorrelated.

2.2.2 Power spectral density of particle motion

Another useful statistical quantity of the random walk of a confined particle is the power spectral density (PSD) of its position time trace. Starting with equation 2.15, an expression for the (one-sided) PSD can be derived [10, 146]:

$$P(f_i) = \frac{D}{\pi^2(f_c^2 + f_i^2)} \tag{2.19}$$

where $f_c = k/(2\pi\gamma_0)$ is the corner frequency, and $f_i = i/T_{msr}$, $(i = 0, 1, 2, ...)$ makes up the frequency space axis, with T_{msr} being the time for which the signal $x(t)$ has been recorded. Note that the corner frequency depends linearly on the spring constant of the confining potential k; the stronger the optical trap, the larger is f_c. The corner frequency is a measure for the time scale at which the motion of the particle is dominated by the trapping potential, rather than the fluctuating thermal force. Thus, in strong traps with large corner frequencies, the particle will feel the influence of the trapping potential on shorter time scales than in weak traps, as is intuitively clear.

2.2.3 Full hydrodynamic theory

There are several effects not taken into account by the Langevin equation (equation 2.15). First, due to the approximation we made, the inertia of the particle has been neglected. Second, we have not taken into account the inertia of the fluid: whenever the particle moves, it will (by its drag) also move the fluid that surrounds it. This means that the friction between the particle and the fluid depends on the particle's *past* motion, since this past motion determines the fluid's present motion. This effect is called the hydrodynamic memory effect. A generalized Langevin equation can be formulated, which takes these two effects into account [10, 19].

From this generalized Langevin equation one can find the hydrodynamically correct form of the power spectral density of the motion of the confined particle [10]:

$$P_{hydro}(f) = \frac{D/\pi^2[1 + (f/f_\nu)^{1/2}]}{(f_c - f^{3/2}/f_\nu^{1/2} - f^2/f_m)^2 + (f + f^{3/2}/f_\nu^{1/2})^2}, \tag{2.20}$$

where $f_m = \gamma_0/(2\pi m^*)$, with $m^* = m + 2\pi\rho a^3/3$. ρ is the mass density of the fluid. $f_\nu = \nu/(\pi a^2)$, with $\nu = \eta/\rho$ being the kinematic friction coefficient of the fluid.

The frequency constants f_m, f_c and f_ν give the time scales on which the inertia of the particle, the confinement of the trap, and the inertia of the surrounding displaced fluid dominate the particle's motion, respectively. For example, for a 500 nm diameter polystyrene particle in water held in an optical trap with stiffness $k = 64\mu$N/m, on very fast time scales, the particle is mostly influenced by inertial effects ($f_m = 2.65$MHz). On slow time scales of $f_c = 1/(2\pi\tau) = 1$kHz, the confinement of the optical trap dominates the particle's motion. In the intermediate regime the particle's motion is dominated by the inertia of the surrounding fluid and the hydrodynamic memory effect ($f_\nu = 680$kHz) [80].

2.2.4 Distribution of particle positions

The probability density of the positions visited by the trapped particle is likely the most important statistical quantity for this dissertation. From equilibrium statistical mechanics it is clear that such a probability density exists for a particle confined in a harmonic potential, and that it must follow Boltzmann statistics [39]:

$$p(\boldsymbol{r}) = \frac{\sqrt{k_x k_y k_z}}{(2\pi k_B T)^{3/2}} \mathrm{e}^{\frac{-E(\boldsymbol{r})}{k_B T}}, \tag{2.21}$$

where the energy landscape is given by the harmonic confinement of the particle, $E(\boldsymbol{r}) = \frac{1}{2}(k_x x^2 + k_y y^2 + k_z z^2)$. Equation 2.21 is a *three-dimensional Gaussian distribution.* The positions of a particle confined by optical tweezers are thus Gaussian distributed.

This probability density is only valid at equilibrium though, and it is not immediately clear for how long one has to observe the particle so that its position probability has reached equilibrium. The temporal evolution of the probability density of a harmonically confined particle is given by the Smoluchowski equation, which is discussed below. We will see that for long enough time scales the probability density indeed approaches the Boltzmann distribution (equation 2.21).

2.2.4.1 The Smoluchowski equation

The time evolution of the spatial probability density of a particle diffusing in a (one-dimensional) harmonic potential is given by the following Smoluchowski equation [121]:

$$\frac{\partial p(x,t|x_0,t_0)}{\partial t} = D\left(\frac{\partial^2}{\partial x^2} + \frac{k}{k_B T}\frac{\partial}{\partial x}x\right) p(x,t|x_0,t_0). \tag{2.22}$$

Assuming that the particle's position was known to be x_0 at $t = t_0$, i.e.

$$p(x,t_0|x_0,t_0) = \delta(x - x_0), \tag{2.23}$$

then equation 2.22 is solved by

$$
\begin{aligned}
p(x,t|x_0,t_0) &= \frac{1}{\sqrt{2\pi k_B T S(t,t_0)/k}} \exp\left[-\frac{\left(x - x_0 \mathrm{e}^{-2(t-t_0)/\tilde{\tau}}\right)^2}{2k_B T S(t,t_0)/k}\right] && (2.24)\\
S(t,t_0) &= 1 - \mathrm{e}^{-4(t-t_0)/\tilde{\tau}} && (2.25)\\
\tilde{\tau} &= 2k_B T/(kD) = 2\tau, && (2.26)
\end{aligned}
$$

where τ is the autocorrelation time of the position fluctuations in the given optical trap, as defined in section 2.2.1.

Figure 2.2 shows the time evolution of the probability density for a 200 nm diameter particle that at $t_0 = 0$ was localized at $x_0 = 100$ nm in a harmonic potential with spring constant $k = 1$ pN/μm. The viscosity was that of water at room temperature, $\eta = 8.9 \cdot 10^{-4}$ Pa s. At fractions of the autocorrelation time (red curve) the particle has not yet felt the effects of the confining potential, and its probability density can be approximated as Gaussian, spreading around the particle's initial position. However, as several autocorrelation times pass, the density approaches Boltzmann statistics (black curve). Observation times in the present work were always many orders of magnitude larger than the autocorrelation time. Therefore, we may use equilibrium statistical mechanics in the following.

2.2.4.2 The voxel occupancy

In this work a PFM is used to track the positions of a nano-particle confined in a harmonic potential. As will be shown, one can generate visual representations of the particle's surrounding by interpreting the measured

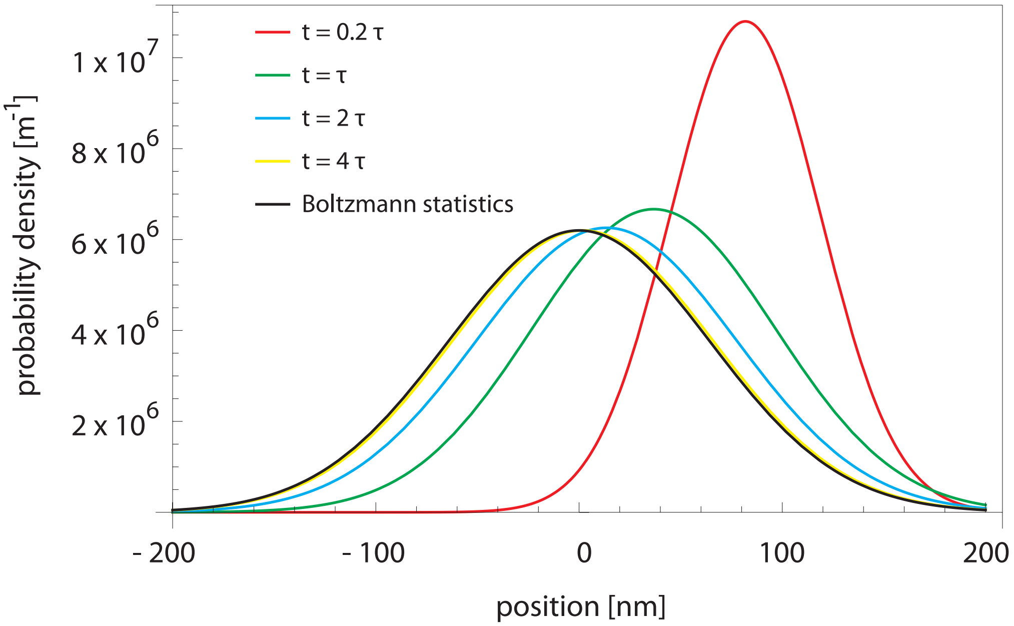

Figure 2.2: Time evolution of the probability density for a 200 nm diameter particle that at $t_0 = 0$ was localized at $x_0 = 100$ nm in a harmonic potential with spring constant $k = 1$ pN/μm. The viscosity was that of water at room temperature, $\eta = 8.9 \cdot 10^{-4}$ Pa s. τ is the autocorrelation time of position fluctuations of the trapped particle.

probability density of particle positions (see section 2.4).

However, due to finite observation times, this probability density can only be measured approximately. This approximation is done by subdividing the volume accessible to the particle ("trapping volume") into voxels, typically of size 10 nm x 10 nm x 10 nm, unless noted otherwise. One then counts how often the particle visited each voxel during the observation time T_{msr}; the resulting three-dimensional matrix of counts is called the voxel occupancy.

The theoretical expectation value for the voxel occupancy follows from the Boltzmann distribution (equation 2.21). The probability to find the particle in the voxel $(x, x+\epsilon), (y, y+\epsilon), (z, z+\epsilon)$, where ϵ is the side length of the voxel, can be approximated by

$$P = p(x, y, z)\epsilon^3. \tag{2.27}$$

The theoretical occupancy of a voxel located at (x, y, z) is then

$$\begin{aligned} n(x, y, z) &= N\epsilon^3 p(x, y, z) && (2.28)\\ &= N\epsilon^3 \frac{\sqrt{k_x k_y k_z}}{(2\pi k_B T)^{3/2}} \exp\left[\frac{-E(x, y, z)}{k_B T}\right], && (2.29)\end{aligned}$$

where $N = T_{msr}/\Delta t$ is the number of acquired points in the time series. Δt is the time between samples.

By rearranging this equation, we see that from the voxel occupancy we can recover the underlying energy landscape:

$$E(x, y, z) = -k_B T \ln\left[n(x, y, z)\right] + C, \tag{2.30}$$

where the additive constant $C = \ln\left[N\epsilon^3 \frac{\sqrt{k_x k_y k_z}}{(2\pi k_B T)^{3/2}}\right]$ is of no further significance (the offset of an energy landscape is arbitrary by the work-energy theorem). We may therefore set $C = 0$, or any other value we find convenient.

Let us restate equation 2.30 for the *measured* energy $E_m(x, y, z)$ and voxel occupancy $n_m(x, y, z)$:

$$E_m(x, y, z) = -k_B T \ln\left[n_m(x, y, z)\right] + C, \tag{2.31}$$

Of course our measured voxel occupancy will only be equal to the theoretical expression 2.29 within some error. This error is given by counting statistics; however the statistics are complicated by correlations between individual counts: Consider a particle diffusing through a voxel with side length ϵ. Then, by equation 2.16 the particle will on average spend a characteristic time $\tau_\epsilon = \epsilon^2/(2D)$ in this voxel. If we sample the particle's position at time intervals Δt, with $\Delta t < \tau_\epsilon$, then $N_{corr} = \tau_\epsilon/\Delta t$ subsequent counts will be highly correlated (we find the particle in the voxel for most of them). To find an expression for the error of such correlated counting statistics an approach by Straatsma *et al.* (see [133]) was adapted:

For each voxel α we have a correlated time series of equally spaced events $X_{\alpha,i}$, which indicate whether at time i the particle visited the voxel ($X_{\alpha,i} = 1$, with probability p) or the particle did not visit the voxel ($X_{\alpha,i} = 0$, with probability q). Consider a time series of length N. The measured voxel occupancy is

$$n_{m,\alpha} = \sum_{i=0}^{N} X_{\alpha,i}. \tag{2.32}$$

By [133] the variance of the measured voxel occupancy is then given by

$$\begin{aligned}
\mathrm{var}(n_{m,\alpha}) &= N\,\mathrm{var}(X_{\alpha,i})(1 + 2N_{corr}) && (2.33)\\
&= Npq(1 + 2N_{corr}) && (2.34)\\
&\approx Np(1 + 2N_{corr}) && (2.35)\\
&= n_\alpha(1 + 2N_{corr}). && (2.36)
\end{aligned}$$

where it was used that $\mathrm{var}(X_{\alpha,i}) = pq$ for a Bernoulli-like event, and $n_\alpha = Np$ is the theoretical voxel occupancy of voxel α. The approximation leading to equation 2.35 is valid since $p \ll q$ and $q \approx 1$, which is the definition of a Poisson process. Equation 2.36 is the desired expression for the variance of the occupancy of one voxel, taking correlated counting statistics into account. Note that the expression simplifies to Poisson statistics for the case of zero correlation, since for $N_{corr} = 0$ it follows that $\mathrm{var}(n_{m,\alpha}) = n_\alpha$, as it should.

In practice, we will want to find the underlying energy landscape by equation 2.31 from the measured voxel occupancy. Thus, the theoretical voxel occupancy $n(x, y, z)$ is not known. Therefore it is necessary to approximate $n(x, y, z)$ in equation 2.36 by the measured voxel occupancy $n_m(x, y, z)$, leading to

$$\mathrm{var}(n_{m,\alpha}) = n_{m,\alpha}(1 + 2N_{corr}). \tag{2.37}$$

2.2.5 Determination of the stiffness of the trapping potential

As pointed out in section 2.1, it is almost impossible to accurately compute the spring constants for a given PFM from first principles. However, this is not necessary, as the spring constants can easily be extracted by a simple measurement [39].

Consider a particle trapped in the harmonic trapping potential given by equation 2.7, interacting only with the surrounding fluid. The spring constants can then be extracted by equation 2.29 from the measured voxel occupancy of the particle. The problem may be treated separately for each spatial dimension, since there is no coupling between the Langevin equations for x, y, and

z direction (see equation 2.14). For the x direction it follows then that

$$n_{m,x}(x) = \tilde{C} \exp\left[-\frac{k_x x^2}{2k_B T}\right], \tag{2.38}$$

which is a Gaussian distribution with variance $\sigma_x^2 = k_B T/k_x$. $\tilde{C}$ is a constant which has no further significance. The spring constant in x direction may therefore be computed from the variance of the measured one-dimensional voxel occupancy:

$$k_x = k_B T/\sigma_x^2. \tag{2.39}$$

Alternatively, we may use equation 2.18 to extract the spring constant from the autocorrelation time of the motion in $i = x, y, z$ direction of the trapped particle, τ_i,

$$k_i = \frac{\gamma_0}{\tau_i}. \tag{2.40}$$

Experimentally, the autocorrelation time for motion along x can be found from the time trace by computing (see [100])

$$\langle x(t)x(t+T)\rangle = \langle x^2\rangle \exp\left[-\frac{T}{\tau_x}\right] \tag{2.41}$$

which yields τ_x from a mono-exponential fit.

2.3 Three-dimensional position detection

2.3.1 Position detector

We will now turn our attention to detecting the position of the confined nano-particle within the optical trap. Independent of what approach we take to detecting the particle's position, the spatial resolution of the position detector is always intimately linked to its temporal resolution: For example, by equation 2.16 a 200 nm diameter particle diffuses on average 70 nm within 1 ms. Thus, a 1 kHz detector has an inherent minimum position uncertainty of 70 nm for such a particle. Therefore, in order to achieve a high spatial resolution, a high temporal resolution is necessary. A position detector with a bandwidth of 40 kHz has a minimum position uncertainty of 11 nm, while a 1 MHz detector achieves an uncertainty of $\sim$2 nm. While a high detection bandwidth could in principle be achieved by traditional means like video microcopy using extremely short integration time cameras, it would be impossible to read out the acquired frames at a high rate due to data bandwidth limitations. Even if such a readout could somehow be achieved, the frames would still need to be processed in order to find the particle's position, making realtime tracking of the particle by video microscopy impossible.

To circumvent this difficulty, a novel, high speed detection scheme based on interferometry was first proposed by Allersma *et al.* in 1998 [2], but was initially limited to the two-dimensional motion lateral to the optical axis. One year later, Pralle *et al.* [102] realized that this detector could be extended to three dimensions, thus making a photonic force microscope possible.

Figure 2.3 shows a schematic of this trapping and detection scheme. The expanded beam of a near-infrared laser is focused through an objective lens and forms an optical trap in the focal plane (red wavefronts in figure 2.3). A single particle is held in the trap and forward scatters a part of the trapping beam (orange wavefronts). Transmitted light of the trapping

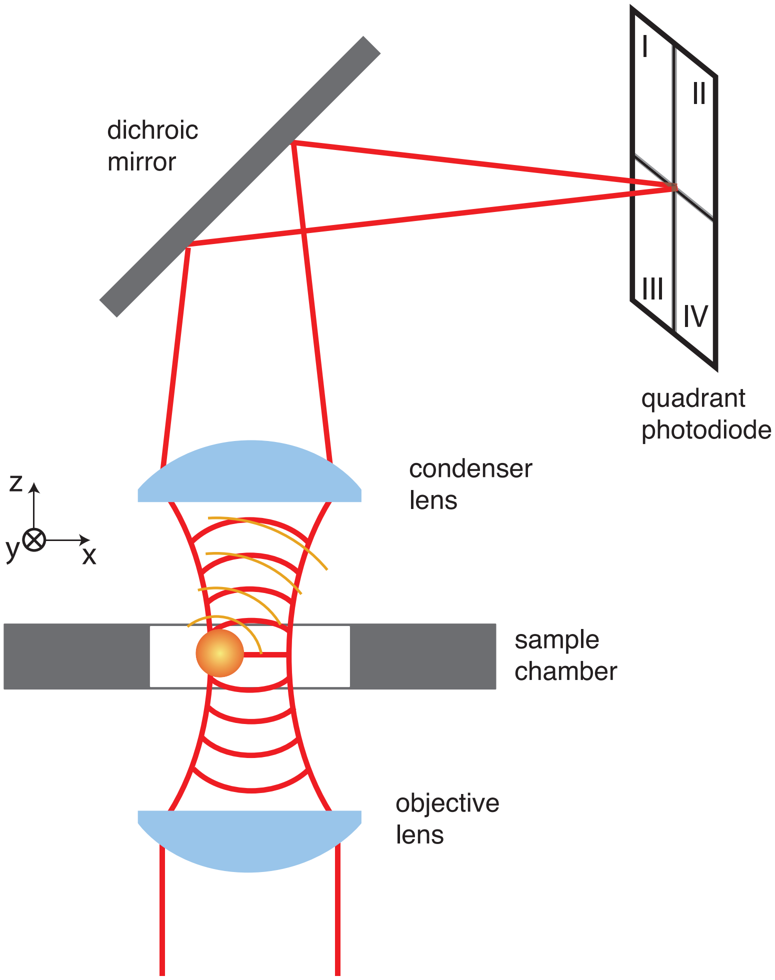

Figure 2.3: Trapping and detection scheme of a photonic force microscope. A near-infrared laser (1064 nm) is focused through an objective lens and forms a single-beam optical trap in the focal plane of the lens. A single colloidal nano-particle is trapped in the beam. The light from the laser beam (red), as well as forward-scattered light from the trapped particle (orange), are collected by a condenser lens and projected onto a quadrant photodiode (QPD). The electrical signals of the QPD are used for 3D position tracking of the particle in the optical trap. Movement of the stage allows for displacement of the optical trap relative to the sample chamber with nanometer precision.

beam along with forward scattered light is collected by a condenser lens and focused on a quadrant photodiode (QPD), where the two waves interfere and produce the particle position signal. The quantitatively accurate treatment of this signal is involved [102, 112, 113], but it can be motivated qualitatively: When the particle moves along the x-axis, the interference pattern on the QPD will move laterally as well. If the particle moves in y direction, the interference pattern will move up- and downwards on the QPD. Thus, for a *small* displacement of the particle from the center of the trap in x direction (Δx)

$$\Delta x \propto [(S_I + S_{III}) - (S_{II} + S_{IV})] = S_x, \tag{2.42}$$

where S_i, $i = I, II, III, IV$ are the output voltages of the four quadrants. Analogously, we have for a displacement in y direction

$$\Delta y \propto [(S_I + S_{II}) - (S_{III} + S_{IV})] = S_y. \tag{2.43}$$

The displacement along the optical axis is proportional to the full intensity on the QPD:

$$\Delta z \propto [(S_I + S_{II} + S_{III} + S_{IV})] = S_z. \tag{2.44}$$

This proportionality to the full intensity is a result of Gouy phase shift (for an elegant Fourier space treatment, see [113]). A focused laser beam undergoes a gradual phase shift of $\Delta\phi = \pi$ while passing through the focus. Light scattered by the trapped particle will have a phase corresponding to its displacement from the focus. Therefore scattered and unscattered light have a phase difference depending on the particle's displacement from the focus, reflected in the intensity of the interference of the two beams.

The signals S_x, S_y and S_z (also referred to as the "detector response") can be directly measured by moving a particle attached to a glass coverslip through the stationary focus along the x, y and z direction respectively, and recording the output of the quadrant photodiode. Figure 2.4 shows the result of such a measurement for one of the PFMs used in this work for a 500 nm diameter polystyrene particle. Shown in red is the linear range of the detector, in which the electronic signal can be approximated as being linearly dependent on the displacement of the particle from the center of the trap. This linear range was defined as the part of the curve having a slope within 15% of the maximum slope. The full width of the linear ranges for a typical 500 nm diameter polystyrene particle are $\Delta x = 200$ nm, $\Delta y = 180$ nm and $\Delta z = 450$ nm. Equations 2.42, 2.43 and 2.44 are only valid in this range. The slope of the linear range is called the detector sensitivity β. It describes by how much the detector responds for a given displacement of the particle.

For large displacements from the focus, the relationship between particle motion and detector response becomes increasingly nonlinear, and the sensitivity is no longer sufficient to calculate the correct particle position from the detector response: additional non-linear terms must be taken into account. This concern is addressed below.

2.3.2 Detector calibration and nonlinearity correction

As explained above, using interferometry to track the position of a trapped particle yields electronic signals S_x, S_y and S_z that are proportional

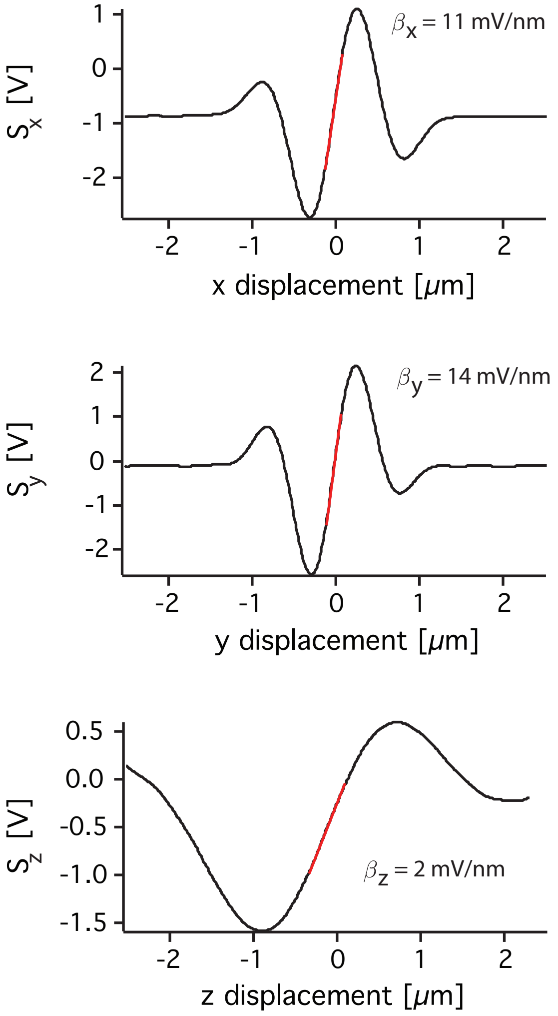

Figure 2.4: Typical response of the position detector of a photonic force microscope. A 500 nm diameter polystyrene particle was attached to a glass coverslip and scanned through the focus along the x-, y- and z-axis of the system. From the output voltages of the QPD, the detector responses S_x, S_y and S_z were computed. Red indicates the linear range of the detector for the given axis. The slope of the linear range is the detector sensitivity β. The full width of the linear ranges for the given particle were $\Delta x = 200$ nm, $\Delta y = 180$ nm and $\Delta z = 450$ nm. The focus is located at $x, y, z = 0$.

to the particle's motion only for small displacements from the focus. Larger extensions lead to a non-linear relationship between particle displacement and detector response. It is therefore necessary to find a non-linear transformation relating the response to the particle position. In other words, it is necessary to linearize the detector. One possibility is to record the detector response ahead of any experiments by scanning an immobilized bead through the focus (see figure 2.4). However, there are several severe pitfalls with this approach: Firstly, the particle has to be adhered to a substrate in order to be immobilized. The contact between substrate and particle changes the scattered wave from the particle, and thus the detector response, compared to a particle diffusing in solution. Secondly, the local environment within the sample can scatter light as well, thus influencing the signal on the detector; the response curves therefore change locally for different positions in the sample. This makes a detector calibration *in situ* desirable.

Here, we follow a method based on the analysis of the MSD (see section 2.2.1) of the trapped particle, which allows the detector to be calibrated *in situ*, at a location in the sample close to the one at which the experiment is performed [138].

Consider the trapped particle diffusing through position x_0, y_0, z_0 in the trapping volume. The detector then shows a response $S_x(x_0) = SX_0$, $S_y(y_0) = SY_0$ and $S_z(z_0) = SZ_0$. Further x_0, y_0, z_0 may be far enough from the focus so that the sensitivity can no longer be used to accurately describe the relation between a small change in particle position δx and corresponding change in detector response δS_x. We may assume though that the local slope of the response $\partial S_x/\partial x$ does not change much over the change in particle position δx. The local slope of the x response can then be approximated for the voxel centered around x_0, y_0, z_0 as

$$\left.\frac{\partial S_x}{\partial x}\right|_{SX_0} = \sqrt{\frac{MSD_L^*\left(SX_0, t\right)}{2Dt}}, \tag{2.45}$$

where MSD_L^* is the local MSD of the *detector response* of the particle's motion in units of V^2, computed from all parts of the response time trace which start in the voxel centered around SX_0. It is divided by the theoretically expected MSD in units of m^2 given by $2Dt$. t is a time lag that must be short enough so that the particle does not diffuse too far away from the voxel under consideration. Methods to determine a suitable length of t are discussed in [138].

This procedure is done for all voxels in the trapping volume. One can then integrate to find $x(S_x)$ which is the desired relation between measured detector response and particle position which both linearizes and calibrates the detector:

$$x(S_x) = \int \frac{1}{\partial_x S_x|_{SX'}} \mathrm{d}SX' \tag{2.46}$$

The linearization and calibration for the y and z direction are obtained in a completely analogous manner.

2.4 Thermal noise imaging

The high resolution and high bandwidth trapping and tracking of a small nano-particle discussed in the previous sections can be used for three-dimensional super resolution imaging of soft matter. This imaging technique is discussed in this section.

Thermal noise imaging (TNI) is a scanning probe technique that can be implemented using a PFM. TNI utilizes the confined thermal motion of the optically trapped particle as a three-dimensional, noninvasive scanner for soft, biological material. Consider as an analogy a tennis ball (the tracer particle) randomly moving (thermal motion) through a room (the optical trap). Let's assume the room is empty but for some object, e.g. a table (the biological material). If the ball's motion is now tracked for an extended time with high spatial precision and high bandwidth (to avoid motion blur), then a three-dimensional histogram of ball positions (voxel occupancy, see section 2.2.4.2) will feature an excluded volume of all voxels that were occupied by the table, since they were inaccessible to the ball. Thus, a three-dimensional (inverse) image of the table can be generated. This image is called a "thermal noise image". Confining the motion of the particle is essential: If there is no confinement to the volume of interest, the particle will just diffuse away and one cannot collect enough statistically independent data points to construct an image. Particle positions must be measured with extraordinary bandwidth ($\sim$1Mhz) in order to avoid motion blur which would lead to an increase in position measurement uncertainty (see section 2.3.1). These requirements make a PFM an ideal choice to perform TNI experiments.

Consider now as an example a 200 nm diameter tracer particle confined in a weak optical trap. It's position can be tracked with nanometer precision (see section 2.5.6) and megahertz bandwidth (figure 2.5A). After observing the particle's position traces for several seconds the voxel occupancy of the trapping volume (see section 2.2.4.2) can be computed (figure 2.5B). The time over which the particle's motion is tracked is the *integration time* of the thermal noise image. Plotting an iso-occupancy surface yields the representation shown in figure 2.5C. This representation is called the thermal noise image of the trapping volume. If a biological fiber intersects the trapping volume, a cylindrical volume becomes inaccessible to the diffusion of the particle (figure 2.5D). This excluded volume has a radius R_E equal to the sum of the fiber's radius R_F and the particle's radius R_P (see dashed circle in figure 2.5D),

$$R_E = R_F + R_p. \tag{2.47}$$

The iso-occupancy surface for this case clearly shows the excluded volume (see figure 2.5E) and is called the thermal noise image of the fiber. The surface roughness of the image is dominated by the standard deviation of the measured voxel occupancy due to correlated counting statistics (see equation 2.37). Errors in the position measurement of the particle (1 nm laterally and 7 nm axially) do not significantly impact the measured voxel occupancy since the particle's positions are binned into comparably large voxels (10 nm x 10 nm x 10 nm).

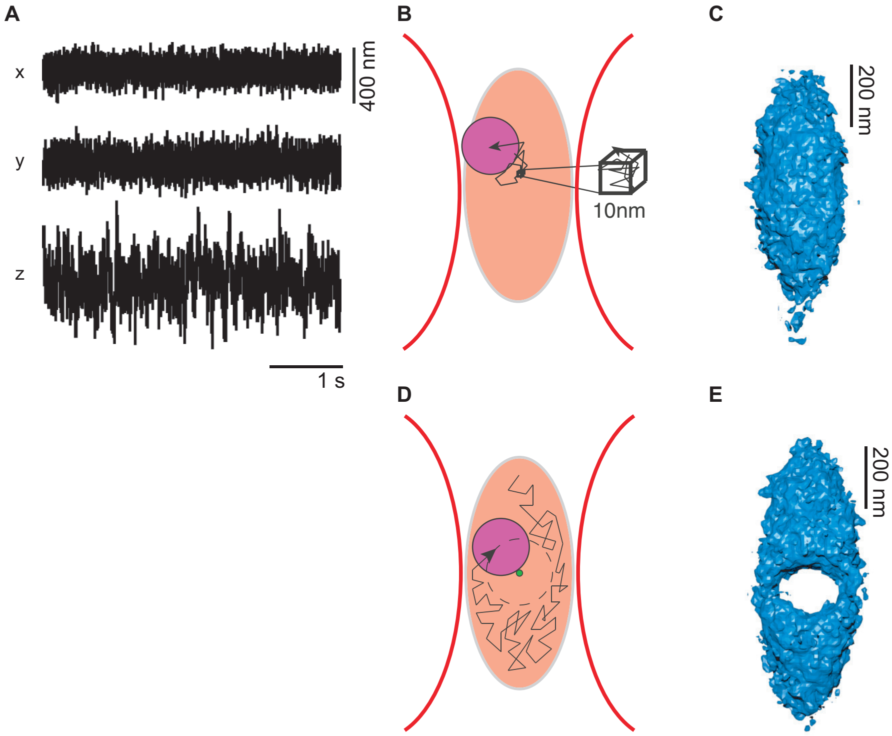

Figure 2.5: Principle of thermal noise imaging. **A** - Typical time traces of a 200 nm diameter particle diffusing in a weak optical trap. **B** - The trapping volume is subdivided into voxels, here with a side length of 10 nm each, and the voxel occupancy (see section 2.2.4.2) is calculated. **C** - Isosurface of equal voxel occupancy. This representation is called the “thermal noise image” of the trapping volume. **D** - If a biofilament (green circle) is introduced into the optical trap, parts of the trap become inaccessible to the particle’s diffusion (dashed circle). The excluded volume thus depends on the filament’s and on the particle’s radius. **E** - Isosurface of equal voxel occupancy for an optical trap intersected by a biofilament. The excluded volume is clearly visible. This image is termed the thermal noise image of the filament. Particle positions were sampled at 100 kHz at a 1 MHz electronics bandwidth. The biofilament was a single microtubule (see chapter 5). The isosurfaces are drawn for an occupancy value of 3 counts.

The resolution of a thermal noise image is given by two factors, the surface roughness of the image as discussed above, and the size of the probe particle. As an example for the impact of the probe's size consider two biopolymer fibers that are in close proximity but do not touch each other. In order to fully scan around each of the filaments, the probe's diameter must be smaller than the distance between them. If the probe is too large, it will not be able to access the space between the fibers. Consequently, this space will be visualized as an excluded volume in the resulting thermal noise image, even though there was no structure present in it. Thus, the two fibers cannot be fully resolved individually; rather they appear as one large excluded volume.

In the following section we will see that Boltzmann statistics links thermal noise images intimately to the energy landscape in which the tracer particle moves.

2.4.1 The Logarithmic Relative Occupancy (LRO)

As we have seen in section 2.2.4, the energy landscape through which the particle moves can be recovered from the voxel occupancy using Boltzmann statistics by equation 2.31. In the most general case, this energy landscape E is made up of the confining optical trapping potential E_{trap} (see equation 2.7) and the interaction energy between the particle and the structure (e.g. the filament) in the trapping volume E_{str}. There may be external contributions to the total energy landscape: For example a tracer particle with a magnetic moment would feel a magnetostatic contribution when exposed to an external magnetic field. However, such external contributions were not used in this work, and we will ignore them in the following. Thus, by equation 2.31 it follows for the energy landscape E that

$$\begin{aligned} E(x,y,z) &= E_{\text{trap}}(x,y,z) + E_{\text{str}}(x,y,z) && (2.48) \\ &\approx E_m(x,y,z) && (2.49) \\ &= -k_B T \ln\left[n_m(x,y,z)\right] + C, && (2.50) \end{aligned}$$

where E_m is the measured energy landscape, which is only equal to E within error. n_m is the measured voxel occupancy.

E_{trap} is analytically known once the optical trap's spring constants along each axis have been found (see equation 2.7 and section 2.2.5). It is related to the theoretical voxel occupancy for an empty[1] trapping volume n_{trap} by equation 2.29. We therefore have

$$E_{\text{trap}}(x,y,z) = -k_B T \ln\left[n_{\text{trap}}(x,y,z)\right] + C'. \qquad (2.51)$$

where C' is an additive constant of no further significance.

Rewriting equation 2.48 then yields the interaction energy between tracer particle and the scanned structure:

$$\begin{aligned} E_{\text{str}}(x,y,z) &= E(x,y,z) - E_{\text{trap}}(x,y,z) && (2.52) \\ \approx E_{m,\text{str}}(x,y,z) &= E_m(x,y,z) - E_{\text{trap}}(x,y,z) && (2.53) \\ &= -k_B T \ln\left[\frac{n_m(x,y,z)}{n_{\text{trap}}(x,y,z)}\right] + \tilde{C}, && (2.54) \end{aligned}$$

---

[1] "empty" here means that there is only the trapped tracer particle and no biological material in the trapping volume.

where again we have to approximate E by E_m, and consequently can only extract the *measured* interaction energy between particle and structure, $E_{m,\text{str}}$. The constant $\tilde{C}$ may be set to zero by the work-energy theorem. The negative natural logarithm of the ratio of measured voxel occupancy to theoretically expected voxel occupancy for an empty trapping volume is called the *Logarithmic Relative Occupancy (LRO)*:

$$\text{LRO}(x, y, z) = -\ln\left[\frac{n_m(x, y, z)}{n_{\text{trap}}(x, y, z)}\right] \tag{2.55}$$

The LRO is equal to the measured interaction energy between the tracer particle and the scanned structure, in units of $k_B T$. If the LRO is calculated for an empty trapping volume, n_m is equal to n_{trap} within error, and the LRO is approximately zero, as one would expect.

The uncertainty of the LRO's measurement can be found by propagating the standard deviation of the voxel occupancy:

$$\sigma_{\text{LRO}}(x, y, z) = \frac{\sqrt{\text{var}\left(n_m(x, y, z)\right)}}{n_m(x, y, z)}, \tag{2.56}$$

where $\text{var}\left(n_m(x, y, z)\right)$ is the variance in voxel occupancy calculated by correlated counting statistics (see equation 2.37).

It is important to remember that we have made no assumption as to what exact form the interaction energy between particle and structure takes. If the scanned structure is static, the energy is given by the electrostatic and steric interaction between the particle and the structure. However, if the scanned structure fluctuates, for example by thermal motion, the meaning of the interaction energy is not so clear. For this important case, which is discussed in detail in chapter 5, the interaction energy is an "effective" energy landscape dominated by the motion of the scanned structure.

2.4.2 The Standardized Occupancy (SO)

Voxels far away from the center of the trapping volume are visited by the particle very rarely, and their measured voxel occupancies and LROs have large errors. It is therefore useful to introduce a quantity which describes the statistical significance of a given voxel occupancy measurement, i.e. how likely it is that the difference between n_m and n_{trap} is caused due to a change in the underlying energy landscape, and thus due to the presence of a scanned structure, rather than due to insufficient counting statistics. The *Standardized Occupancy (SO)* quantifies by how many standard deviations the measured occupancy of a voxel differs from its theoretical occupancy:

$$\mathrm{SO}(x,y,z) = \frac{n_m(x,y,z) - n_{\text{trap}}(x,y,z)}{\sqrt{\operatorname{var}\big(n_m(x,y,z)\big)}} \tag{2.57}$$

where $\operatorname{var}\big(n_m(x,y,z)\big)$ is the variance in voxel occupancy calculated by correlated counting statistics (see equation 2.37). For the case of an empty trap, in which n_m approximates n_{trap}, this definition of the SO is analogous to the definition of a standardized random variable with zero mean and standard deviation of unity. Therefore, the larger the magnitude of the SO, the more statistically significant the measured LRO is.

2.5 Implementation

In the course of this research, two custom built photonic force microscopes in almost identical configurations were used. The first ("Single Molecule PFM") was based on a design by Rongxin Huang [56], but was strongly improved, and its precision enhanced, especially for detection along the optical axis. Since the axial position signal corresponds to the full intensity on the QPD (see section 2.3.1), the power noise of the trapping beam dominates the error with which the axial position of the trapped particle can be measured. The initially used laser's power noise was too large to track the axial motion of small particles (~200 nm diameter). Thus, a novel method to analyze the power stability of lasers was developed by the author [72], and a large number of commercially available DPSS lasers were compared. As a result, the initially used Crystalaser (Crystalaser, 1W, 1064 nm, SLM, ultra-stable option, Crystalaser, NV, USA) was replaced with the several orders of magnitude more stable Mephisto (Mephisto 500 mW, 1064 nm, Noise Eater Option, Innolight, Germany).

The second PFM ("Thermal Noise Imaging PFM") was co-developed from scratch with Dr. Martin Kochanczyk, and is described in detail in his dissertation [71]. It features a much lighter condenser assembly, which greatly reduces low frequency noise in the position detection of small (~200 nm diameter) particles. The stability of both PFMs is discussed in section 2.5.6.

The author developed an extensive library of Labview Realtime software for instrument control, calibration, data acquisition, data evaluation and realtime feedback from the ground up for both microscopes.

Figure 2.6 shows the design of both PFMs, as well as the beam paths of the trapping and tracking beam, and of the fluorescence excitation and emission. Below, the essential components of both PFMs are briefly described. Differences between the two different microscopes are pointed out where they exist.

2.5.1 Optical tweezers and 3D position detector

The beam (red dashed line in figure 2.6) of a continuous wave, near-infrared DPSS laser operating in a TEM_{00} mode (Crystalaser, 1W, 1064 nm, SLM, ultra-stable option, Crystalaser, NV, USA; and later Mephisto 500 mW, 1064 nm, Noise Eater Option, Innolight, Germany) was passed through a Faraday isolator (2I1055-WP2, EOT Inc., MI, USA) to optically decouple the laser from the microscope, and then expanded and collimated by a 10x beam expander (Sill Optics, Germany) to overfill the back aperture of the objective lens. It is convenient to use 1064 nm as the wavelength of the trapping laser, as firstly, this wavelength is readily available, and secondly, the photodamage this wavelength causes to biological material is small in comparison to other common wavelengths [91]. Neutral density (ND) filters (Thorlabs, NJ, USA) were used to attenuate the laser power to the desired level. A shutter was placed in the beam path to allow a fast deactivation of the optical trap by blocking the path of the trapping beam. A dichroic mirror reflected $> 99\%$ of the expanded trapping beam into a high NA objective lens (UPlanSApo,

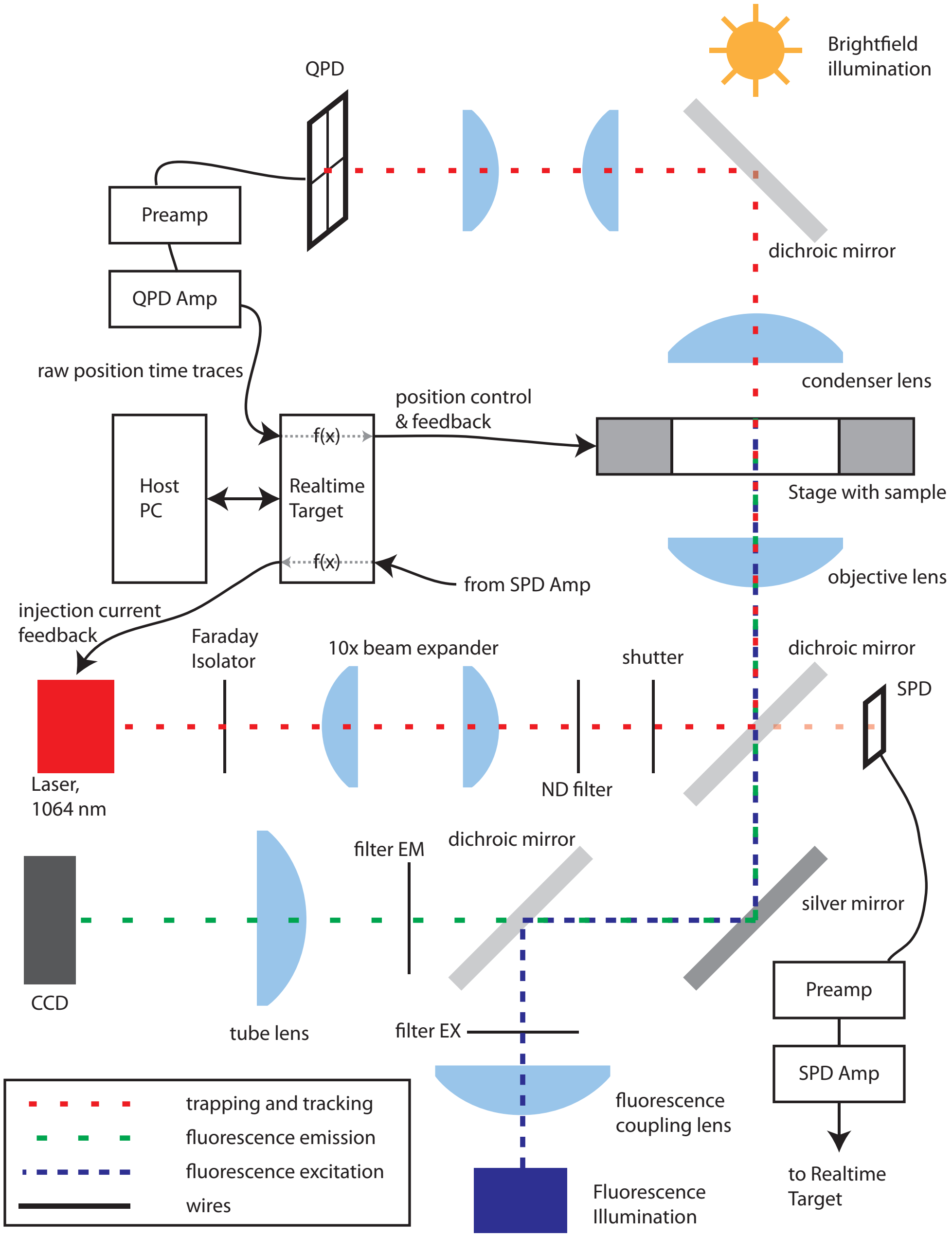

Figure 2.6: Schematic of the components and beam paths of a PFM. See section 2.5 for a detailed discussion.

60x, water immersion, Olympus, Tokyo, Japan), thereby overfilling the back aperture of the lens with an approximately homogeneous intensity distribution. This beam then forms the optical trap discussed in section 2.1 in the focal spot of the objective lens. The intensity of the transmitted fraction of the trapping beam was measured by a single photodiode; its purpose is discussed later (see section 2.5.3).

Behind the focus of the objective lens, the trapping beam (and any forward scattered light from a trapped particle) was collected by a condenser lens (445245-9902, Zeiss, Germany) and then projected onto an InGaAs quadrant photodiode (QPD, G6849, Hamamatsu Photonics, Hamamatsu, Japan), where scattered and unscattered light interfered and formed the trapped particle's position signal. The QPD's output voltage was amplified twice, first by a pre-amplifier and then by a differential main amplifier (both custom built by Wolfgang Oeffner, Oeffner MSR Technik, Germany); the pre-amplifier also computed the detector responses S_i, $i = x, y, z$ (see equations 2.42, 2.43, and 2.44) from the output of the QPD's four quadrants. The bandwidth of pre-amplifier and differential amplifier was $\sim$1 MHz.

The amplified detector response was then sampled at 100 kHz (unless noted otherwise) by the Realtime Target using a high speed and high precision DAQ board (Single Molecule PFM: NI PCI 6120, 16 bit, National Instruments, TX, USA; and later NI PXI 5922, up to 24 bit, National Instruments, TX, USA. Thermal Noise Imaging PFM: NI PCI 6120, 16 bit, National Instruments, TX, USA). The NI PCI 6120 has an integration time of $\sim$9 ns per datapoint (private communications with National Instruments), and thus passes the entire 1 MHz bandwidth available from the amplifiers. The NI PXI 5922 employs a hardware anti-aliasing filter which cannot be deactivated, and has a frequency cutoff at 0.4 times the sampling frequency. Care must therefore be taken when utilizing the NI PXI 5922 so as to not increase the position measurement's uncertainty too much due to the reduced temporal bandwidth (see section 2.3.1).

The software running on the Realtime Target then calibrated (see section 2.3.2) and analyzed the recorded time traces in realtime, and, depending on the experiment, sent a feedback signal to the nano-positioning stage which repositioned the sample accordingly.

2.5.2 Sample positioning

Both PFMs were employed with x, y, z - nano-positioning stages in order to position the sample relative to the stationary optical trap. The stage used on the Single Molecule PFM (P-561, Physik Instrumente, Germany) had an unfortunate resonance frequency of ∼180 Hz which was easily excited by ambient noise, causing a lateral vibration of the stage with a standard deviation of ∼1 nm (see section 2.5.6.1), even under optimized conditions. Therefore, the precision of a position measurement on this microscope could not exceed 1 nm. The stage attached to the Thermal Noise Imaging PFM (PDQ375, Mad City Labs, WI, USA) had a resonance in the kilohertz range, which is not as easily excited by ambient noise as the 180 Hz resonance.

Positioning commands could be sent from the Realtime Target to both stages at a rate of ~1 kHz, sufficient for the position feedback required in this work.

2.5.3 Laser stabilization

Changes in the signal of the single photodiode (SPD) reflect power fluctuations in the trapping and tracking laser. This signal was monitored by the Realtime Target. By use of a PID loop implemented in Labview Realtime a feedback was calculated, which then acted on the injection current of the laser, thereby eliminating small drifts in the laser power.

2.5.4 Fluorescence microscopy

The beam of a fluorescence excitation source (X-Cite 120Q, LDGI, ON, Canada) was focused by a fluorescence coupling lens into the back focal plane of the objective lens, thus achieving a homogeneous illumination of the sample in the focal plane of the lens (blue dashed line in figure 2.6). Coupling of the beam into the beam path was achieved by a filter set consisting of an excitation filter (filter EX), an emission filter (filter EM) and a dichroic mirror (Chroma, VT, USA). Fluorescence emitted from fluorophores in the focal plane (green dashed line in figure 2.6) was then collected by the objective lens, separated from stray light by the emission filter and focused by the tube lens onto a CCD camera (Single Molecule PFM: iXon EMCCD, Andor, UK; Thermal Noise Imaging PFM: SensiCam QE, PCO, Germany), where it formed an image of the fluorescing material. Fluorescence microscopy was used to image fluorescent particles and fluorescently labeled biofilaments.

2.5.5 Brightfield microscopy

Both PFMs were equipped with a bright field illumination source (Collimated LED Light Source, red, Thorlabs, NJ, USA) which served to through-illuminate the sample through the condenser lens. A bright field image of the focal plane of the objective lens was then recorded by the CCD camera. Brightfield microscopy was employed to image large ($>$ 500 nm diameter) particles, as well as support structures employed in the single biofilament assay (see section 5.2.3).

2.5.6 Stability and position detection resolution

In this work, it was desirable to achieve nanometer resolution in the tracking of the trapped (tracer) particle. Instabilities which lead to a decrease in the precision of the position measurement include fluctuations in the laser power, fluctuations in the laser pointing, fluctuations in the laser phase, as well as vibrating mechanical components (such as lenses, mirrors, the nano-positioning stage, etc.) that are susceptible to excitations and drift [72]. The laser and all mechanical components were carefully chosen or designed to minimize such instabilities. The resulting stability of both PFMs was measured and is discussed below. For both PFMs particles of various diameters were immobilized by adhesion to a glass substrate, and moved into the center of the trapping volume. Tracking of these immobilized particles then reveals the uncertainty in the position detection of the PFMs.

2.5.6.1 Single Molecule PFM

Crystalaser During the experiments described in chapter 3 the Single Molecule PFM was equipped with a Crystalaser (see section 2.5.1). The standard deviation in a typical position measurement of one immobilized 1 μm bead over a time of 5 s was 1.5 nm in the lateral directions, and 1 nm along the optical axis at a sampling rate of 100 kHz, which is at the positioning noise of the x, y, z - nano-positioning stage. This error is thus not a limitation of the position detector; the limiting factor is the nano-positioning stage. This outstanding stability of the PFM is demonstrated in figure 2.7. A 1 μm diameter bead was immobilized on a glass cover slide, and scanned on a 10 nm diameter circle laterally close to the focus (figure 2.7A). The measured particle positions are shown in figure 2.7B. Each datapoint was integrated for 100 ms. Clearly, the scanned circle can be recovered, with little distortion. It is difficult to stabilize the sample over time scales of several minutes. The coverslip was attached to a support using vacuum grease, and showed under optimized conditions a drift of $\sim$10 nm/minute for each axis. This long term stability was sufficient for the experiments presented in this dissertation.

Small beads ($\sim$200 nm in diameter) which scatter much less light[2] could

---

[2] The scattering cross-section of a small dielectric sphere with diameter a is $\propto a^6$ [60]; therefore a 200 nm diameter particle scatters $\sim$15000 times less light than a 1 μm particle.

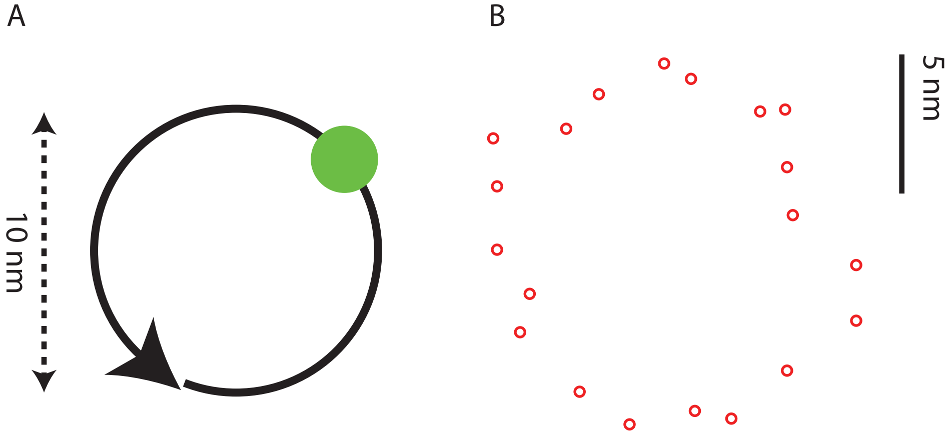

Figure 2.7: Stability and resolution of the Single Molecule PFM. **A** - An immobilized 1 μm diameter bead was scanned laterally, close to the focus of the objective lens on a 10 nm circle. **B** - Measured positions of the circle scan. Positions were sampled at 100 kHz, and every plotted datapoint is the integral of 100 ms of position data.

not be tracked along the optical axis due to the Crystalaser's comparably high intensity noise. The Crystalaser was therefore replaced, and an Innolight Mephisto used for all other experiments.

Innolight Mephisto Experiments on lipid droplets (see chapter 4) were done using the Single Molecule PFM equipped with an Innolight Mephisto laser. Axial tracking of 200 nm diameter particles could easily be accomplished using this laser. Axial position measurements over 5 s (sampling frequency 100 kHz) had a standard deviation of ∼8 nm, less than the typical voxel size (10 nm) used during some of the data analysis for binning. The lateral position error was ∼2 nm, dominated by a slow (1.5 Hz) resonance which corresponds to the eigenfrequency of the optical table floating on nitrogen-pressurized isolators. It is likely that the condenser assembly shifted slightly with the motion of the table, causing the laser beam to move on the detector. This issue was avoided on the Thermal Noise Imaging PFM by use of a redesigned, much lighter condenser assembly [71].

2.5.6.2 Thermal Noise Imaging PFM

The Thermal Noise Imaging PFM (equipped with an Innolight Mephisto laser) was used for thermal noise imaging experiments on single microtubules and collagen networks (chapters 5 and 6), using exclusively 200 nm diameter particles. For such a particle, this PFM performs slightly better than the Single Molecule PFM, due to the elimination of the 1.5 Hz resonance described above. The standard deviation in a typical position measurement of one immobilized 200 nm diameter bead over a time of 5 s was 1 nm laterally and 7 nm along the optical axis, at a bandwidth of 1 MHz and sampling rate of 100 kHz. This PFM uses the same sample chambers as the Single Molecule PFM and consequently has the same long term stability of $\sim$10 nm/minute for each axis, given by the drift of the sample chamber's coverslips.

Chapter 3

Detection of Sequential Bond Formation

The ability to track the position of a tracer particle with nanometer precision is very important for the research described in this dissertation. To demonstrate the outstanding precision in position detection that can be achieved by use of a photonic force microscope (PFM, see chapter 2) the sequential formation of individual molecular bonds between a trapped particle and a surface was resolved and is described in this chapter. As shown below, the discussed method has direct impact on the study of the mechanical properties of small biomolecules. This work was published in [7].

3.1 Introduction

Mechanical single molecule studies provide new mechanistic insight into working and design principles of biomolecules not accessible by bulk methods. For certain classes of biomolecules, such as molecular motors, mechanical properties are of direct importance to their function. For motor molecules, mechanical measurements provide direct insight into the conversion of chemical energy into mechanical work. For a more general class of biomolecules, mechanical measurements reflect the conformational state of the probed molecule as well as changes of that state, since the mechanical properties can be seen as a result of an elastic network of bonds formed within the biomolecule. The stability of such a bond network is probed, for example, in single molecule unfolding experiments [26, 33, 34]. These experiments provide new insight into the factors determining bond stability and in turn elucidate the design principle for the particular molecule or even its entire molecular class. Unfortunately, unfolding experiments apply large forces to the molecule and are destructive while conformational changes in most biomolecules are close to the thermal energy regime. Non-destructive experiments have been performed successfully but so far were limited to large molecules tens of nanometers in size and larger [28, 64, 127, 128, 159]. Getting experimental access to smaller molecules in the range of a few nanometers would be extremely beneficial. Molecules of this size make up the majority of biomolecules and therefore access to this size range will enable the study of a much wider range of phenomena on the single molecule level than previously possible. Their small size will also make it easier to compare in vitro and in silico single-molecule experiments [130], thus improving our mechanistic insight into various phenomena such as ligand-receptor interaction. Mechanical experiments on small molecules are challenging. The molecule of interest needs to be spanned between two surfaces which may start to interact strongly at small separation distances via a complex interplay of various types of attractive and repulsive intermolecular interactions. In addition, the local geometry of the interacting surfaces may influence the measurement. Therefore, it becomes important to establish criteria for single molecule conditions and the presence of specific or nonspecific interactions.

The work described in this chapter demonstrates that the residual thermal motion of a tracer particle linked to the surface either by specific bonds or nonspecific interactions contains a wealth of information about the local binding conditions, even for nanometer size linker molecules. For the case of the ligand-receptor pair biotin-avidin with a total length of approximately 5 nm (estimated from the crystal structure published in ref. [103]) the formation of multiple specific bonds between the tracer particle and the surface could be followed one after the other. Criteria were found to distinguish between specific and nonspecific bond formation from the three-dimensional distribution of the position fluctuations of the tracer particle. To achieve this, the high spatial resolution and high bandwidth position detector of the Single Molecule PFM described in chapter 2 was used, which allowed following the particle's thermal fluctuations in three-dimensions. As shown below, all three components - precision, bandwidth and three-dimensional detection - are important to get reliable, quantitative data.

When a colloidal particle binds to a surface it is not completely immobilized. Thermal forces (see section 2.2) act on the particle and cause displacements about the point (or area) of contact, regardless of whether the contact is formed by specific or nonspecific interactions. Typically, binding takes place on fast time scales so that the immobilization leads to a strong and sudden reduction in thermal position fluctuations. In the most drastic case, the particle diffuses freely in solution while after binding it is confined to displacements of just a few nanometers. In the case where the particle is confined in an optical trap, the particle is initially constrained by the trapping potential and, upon binding, it is additionally confined by the bond to the surface. When the particle binds to the surface via a short linker, the extent of the position fluctuations is dominated by the confinement through the linker. Any change in linkage between the particle and the surface leads to a change in the three-dimensional probability distribution of the particle's thermal position fluctuations. Such changes can either be caused by a change in the linker length, a change in mechanical properties of the linker, or by a change in the number of links formed. Most molecular events lead to an abrupt change in position fluctuations allowing to temporally resolve molecular events if the particle's position is recorded with sufficient bandwidth. If we assume that the linker properties do not change before and after such molecular events, we can convert the three-dimensional probability distribution into a three-dimensional energy landscape using Boltzmann statistics (see section 2.2.4) [39, 64]. In this way, we can extract quantitative information about the contact's properties as long as the probability distribution was measured correctly, i.e. it was measured with sufficient spatial resolution and bandwidth.

The following sections will first focus on nonspecific interactions and discuss the strong adhesion of a tracer particle to glass, as well as its weak adhesion to a protein layer. Subsequently, single specific bonds and then multiple specific bonds are characterized. As we will see below, these interactions can be clearly distinguished from each other.

3.2 Materials and Methods

3.2.1 High bandwidth and high precision optical trapping

The Single Molecule PFM described in section 2.5 was used for the experiments described in this chapter. This PFM has a position detection precision of 1.5 nm laterally and 1 nm along the optical axis at a bandwidth of 1 MHz for tracer particles with 1 μm diameter. Before each data acquisition the PFM was calibrated *in situ* as discussed in section 2.3.2.

3.2.2 Surface preparation

15 mm diameter glass coverslips were immersed in Hellmanex II solution (2% in deionized water, Hellma GmbH & Co. KG, Germany) and sonicated for 15 minutes. Subsequently, they were washed with and immersed in deionized water and sonicated for another 15 minutes. This cleaning procedure was repeated 3 times.

After drying with nitrogen gas, the coverslips were functionalized with BSA (Rockland, PA, USA) and biotinylated BSA (B-BSA, Thermo Fisher Scientific, IL, USA) via physisorption. Stock solutions of B-BSA (2 mg/ml) in phosphate buffered saline (PBS) and BSA (2 mg/ml) in PBS were prepared and mixed in a ratio of 1 to 100. The top surface of each coverslip was homogeneously covered with 100 μl droplets of the BSA solution for the non-biotinylated coverslips and BSA/B-BSA solution for the biotin functionalized coverslips. The prepared coverslips were incubated for 20 min at room temperature and afterwards rinsed with PBS.

3.2.3 Particles

For single molecule experiments, 1 μm diameter polystyrene nano-spheres covered with NeutrAvidin were acquired from Molecular Probes (Invitrogen, CA, USA).

The experiments on nonspecific binding to glass substrates were conducted using carboxylated polystyrene nano-spheres of 1 μm diameter (Invitrogen, CA, USA). Note that the glass coverslip was not coated with BSA for these experiments. The biotinylated tracer particles were prepared by silanizing 970 nm diameter silica beads (Bangs Laboratories, IN, USA) using an APTES (2%) in acetone solution. Subsequently, NHS-Biotin (Thermo Fisher Scientific, IL, USA) was used to covalently attach biotin to the glass beads.

3.3 Results and Discussion

3.3.1 Adhesion to glass

In this section, the nonspecific adhesion of a polystyrene tracer particle to a clean glass surface is explored as an example of a strong, nonspecific interaction. A carboxylated polystyrene particle with diameter of 1 μm is suspended in solution and manipulated towards the clean glass surface using optical tweezers (figure 3.1). Initially, the bead diffuses within the trap, but binds strongly to the glass coverslip after coming into contact with the surface. This event is referred to as "nonspecific" since it does not rely on the specific interaction between two biomolecules. Upon the binding event, the particle's mean position is fixed at the location at which it adsorbed to the glass substrate. Its movement is reduced to thermal fluctuations around its contact area, which depend on the strength of adhesion between particle and substrate, and the position noise resulting from the mechanical stability of the experimental setup. Note that the axial as well as lateral fluctuations are reduced to the same order of magnitude. The residual fluctuations with standard deviations of 1.5 nm along the lateral and 1 nm along the axial direction are at the resolution limit (see section 2.5.6.1). The difference between the magnitude of thermal fluctuations when the trapping potential is the only constraint on the particle's motion, and the residual fluctuations of the immobilized particle, defines the dynamic range of our method. Binding events can be characterized by the additional confinement they put on the thermal position fluctuations of the particle. Binding events are easily identified by the abrupt change in the magnitude of the thermal fluctuations along at least one dimension. These abrupt changes occur because of the separation of timescales between fast molecular scale events that cause the binding and the relatively slow thermal motion of the tracer particle. The discrete changes in fluctuation amplitudes make it possible to count the number of events that occur during binding of the particle to the surface.

3.3.2 Adhesion to a protein layer

For the present method to be applicable to the study of specific interactions, nonspecific binding as described above has to be prevented. In optical trapping experiments, this is typically achieved by coating the surfaces

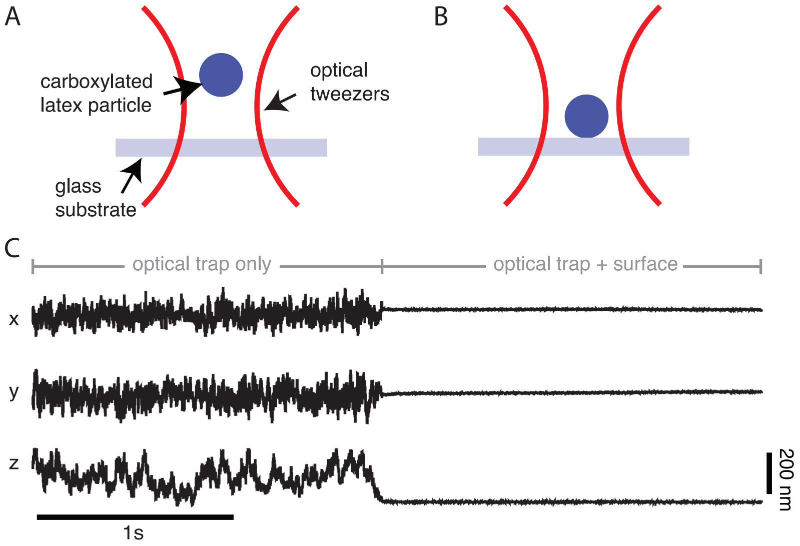

Figure 3.1: Reduction of thermal position fluctuations by nonspecific surface immobilization. **A** - A carboxylate modified latex particle of 1 μm diameter was trapped with weak optical tweezers and its position in x, y and z direction tracked within the trapping volume. The time traces in **C** show its thermal motion in all three dimensions. **B** - After several seconds, the trap was manipulated towards the substrate and the particle bound irreversibly to it. This nonspecific binding event can be seen as a strong reduction in the thermal fluctuations of the position data along all directions.

with blocking reagents such as bovine serum albumin (BSA), casein [64, 134] or polyethylenglycol (PEG) [116, 144]. To demonstrate the efficiency of such blocking, a 1 μm diameter NeutrAvidin coated polystyrene particle and, subsequently, a 970 nm diameter biotinylated silica particle was trapped in solution and manipulated toward a glass coverslip coated with BSA. Figure 3.2 and

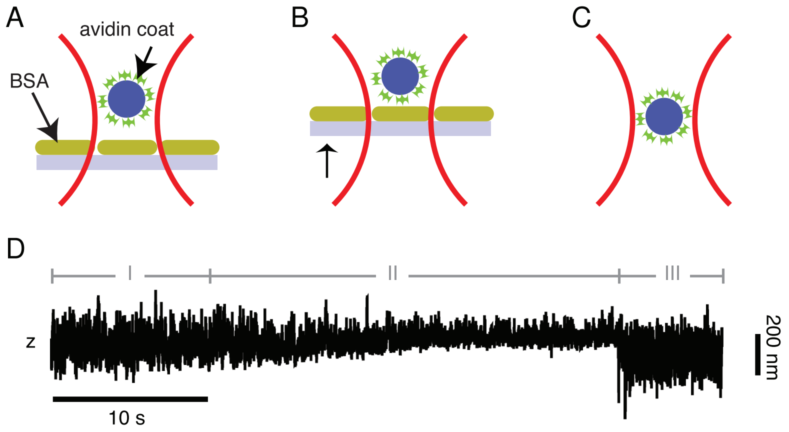

Figure 3.2: Shielding nonspecific interactions with a monolayer of BSA. An avidin coated latex particle of 1 μm diameter was trapped (**A**) and pressed onto a substrate which had been functionalized with a monolayer of BSA (**B**). The accessible trapping volume is reduced as the substrate is moved closer towards the center of the trap as indicated by the reduced fluctuations along the z-axis (**D**). However, other than the reduced explorable space, no interaction between particle and substrate is detected. The particle can still move to the top of the trapping volume, and the lateral fluctuations (not shown) do not change in form. **C** - After more than 20 s, the trap was rapidly manipulated away from the substrate. Immediately, the entire trapping volume becomes available for diffusion, as the particle is no longer restricted by the substrate.

figure 3.3 show time series of position fluctuations for each of the trapped particles. Initially, the diffusion of both particles was only confined by the spatial extent of the trapping volume (figure 3.2A and 3.3A). Slowly each trapped particle was then pressed onto the substrate (figure 3.2B and 3.3B). The further the substrate moved into the trapping volume, the less volume was available for Brownian motion of the particles (reduced axial fluctuation amplitude), and the more often the particles collided with the substrate, thus increasing the probability for a binding event to occur. For the NeutrAvidin coated polystyrene particle, even after pressing it onto the substrate for more than 20 s, no binding event occurred. This is evident from the fact that the maximum value of the axial fluctuations remained unchanged (figure 3.2D, end of phase II). After manipulating the trap away from the surface, the particle's position fluctuations returned to their original levels thus indicating that no binding event occurred (figure 3.2D, phase III). NeutrAvidin functionalized particles could be pressed onto BSA coated substrates for several minutes without showing any indication of a binding event in the position traces. However, in the case of the biotinylated silica particle, a binding event occurred within seconds while the trap was moved closer to the substrate. The binding event is clearly indicated by the strong reduction of the axial thermal fluctuations of the tracer particle (figure 3.3D). In contrast to nonspecific binding to a bare glass surface, the residual fluctuations are in general much larger and parallel to the surface. The 2D histogram of the tracer particle's lateral position fluctuations reveals an asymmetric distribution (figure 3.3E). This asymmetry is to be expected, as the nonspecific bonds originating from the interaction of BSA residues with biotin or from direct contact of the silica tracer particle to BSA form under random orientation, each leading to a distinct, three-dimensional probability

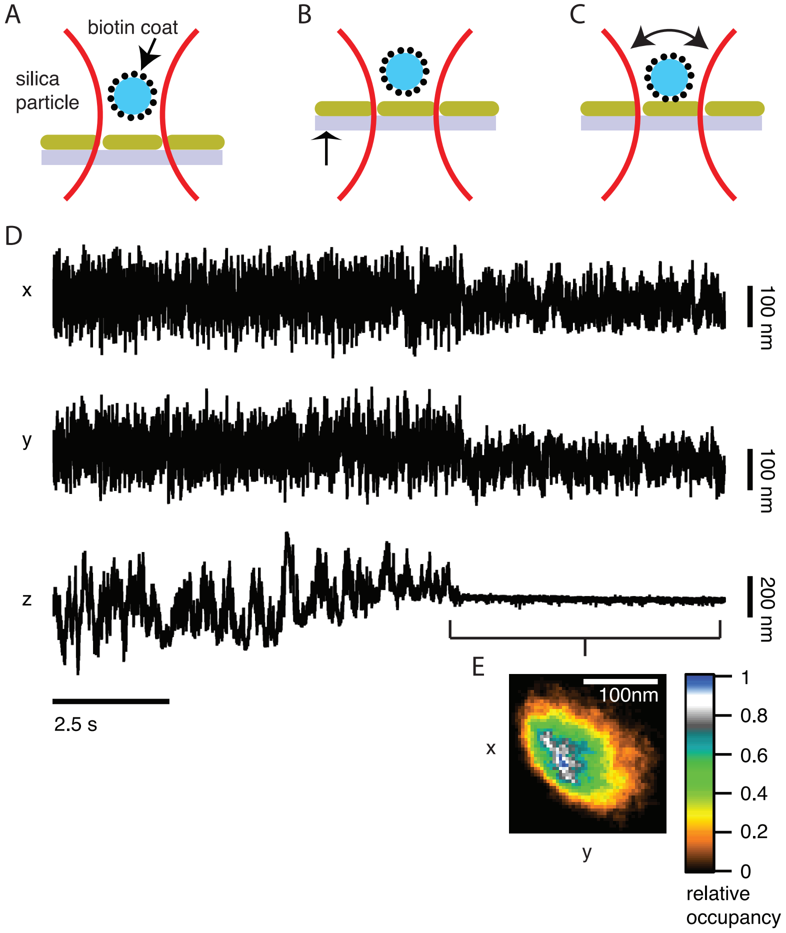

Figure 3.3: Nonspecific interactions with a BSA functionalized surface. A biotin coated silica particle of 970 nm diameter was trapped (**A**) and pressed onto a substrate which had been functionalized with a monolayer of BSA (**B**). The accessible trapping volume is reduced as the substrate is moved closer towards the center of the trap as indicated by the reduction in fluctuations along the z-axis (**D**). After many collisions with the substrate, a nonspecific bond forms between the biotin molecules on the tracer particle and the BSA layer on the substrate (**C**). This binding event can clearly be deduced from the sharp reduction of the axial fluctuations. The reduction in the lateral position fluctuations is noticeable but small, in contrast to the situation in figure 3.1. **E** - The position histogram of the lateral movement of the particle after the binding event shows an asymmetric geometric form.

distribution of the tracer particle position. This attribute suggests that the shape and lateral extent of the distributions could serve as practical indicators to distinguish between specific and nonspecific binding events.

3.3.3 Identification of single molecule bonds

To characterize the probability distributions that result from specific bonds, the well-characterized ligand-receptor complex biotin-avidin [38, 45, 48, 59, 74, 83, 87] was studied. The receptor molecule, NeutrAvidin, was covalently bound to a 1 μm polystyrene particle and its ligand, biotin, was covalently coupled to the protein BSA (figure 3.4A). Since BSA is known to bind strongly to glass surfaces [14], it can be used to provide a ligand-functionalized glass surface. As shown above, BSA also fulfils an additional function of blocking nonspecific interactions between the glass surface and the NeutrAvidin coated particle. In order to achieve single-molecule conditions, the number of specific biotin binding sites was reduced by co-adsorption of plain BSA so that 1 in 100 BSA molecules was functionalized with biotin. Figure 3.4C shows the reduction of axial position fluctuations upon formation of a single biotin-avidin bond. The maximal lateral peak-to-peak fluctuations are also reduced, but their reduction is much smaller. The lateral fluctuations are at least two orders of magnitude larger than for strong, nonspecific binding events (compare with figure 3.1). Note the radial symmetric shape of the lateral position fluctuations. Radial symmetry is to be expected under the conditions that the single specific bond is formed by a linker that does not have a preferred orientation

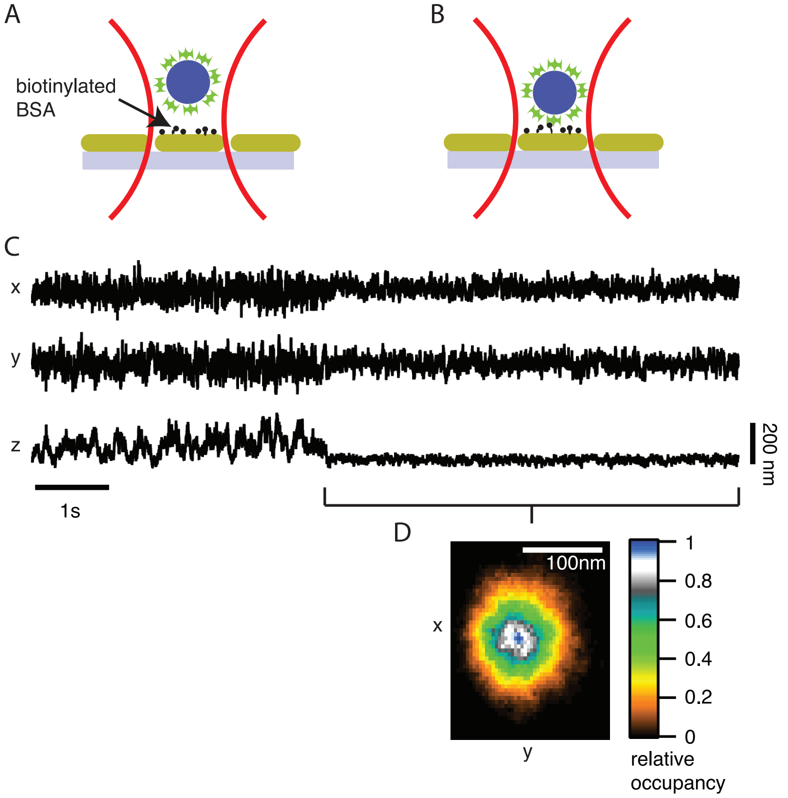

Figure 3.4: Specific interaction between an avidin coated particle and a biotinylated surface. **A** - An avidin coated latex particle of 1 μm diameter was trapped in solution using optical tweezers. The particle explores the trapping volume by diffusion until it is pressed against a substrate sparsely functionalized with biotinylated BSA (one in hundred BSA molecules was functionalized with biotin) (**B**). After several seconds, a reduction of the lateral and axial position fluctuations indicate the formation of one specific biotin-avidin bond (**C**). **D** - A two-dimensional histogram of the particle's lateral movement shows circular symmetry as expected for a single flexible molecular bond.

and the non-specific particle-surface interaction is shielded homogeneously by the blocking reagent. Further evidence for the formation of a single molecular bond can be obtained by considering the length of the molecular tether. The experimental assay can be approximated by a “ball on a string” - model (figure 3.5A). According to the model, the maximal lateral excursion of the tracer particle from the anchor point is given by the radius of the particle and the length of the tether molecule. With a known particle size, an estimate for the tether length can be extracted from the lateral fluctuation data (figure 3.5B). Assuming a bead diameter of 1000 nm, the final amplitude (peak to peak)[1] of the lateral fluctuations of approximately 150 nm corresponds to a linker length of 6 nm. In our assay, the tether consists of biotin residues that are attached to the BSA substrate by linkers with a length of about 2

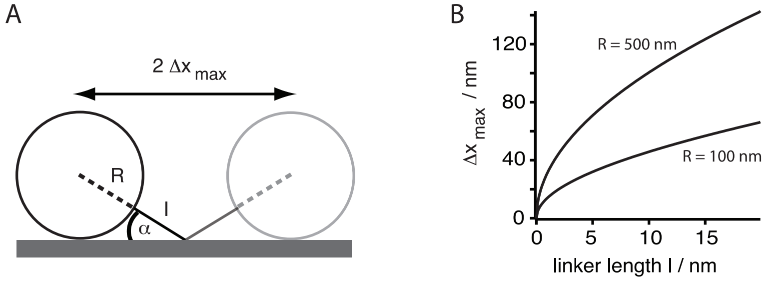

Figure 3.5: Geometrical amplification effect. **A** - A simple geometrical model for a particle with radius R tethered by a single molecule with length l to the substrate. The linker allows the particle to move parallel to the surface with a distance 2 $\Delta x_{\max}$. **B** - The maximal lateral displacement of the particle as a function of linker length for particles of 500 nm and 100 nm in radius. Please note the increased sensitivity for very short linker lengths.

---

[1] The peak-to-peak amplitude was estimated as 6σ, where σ is the mean of the standard deviations of the thermal motion in x and y direction.

nm, and from a single avidin tetramer (approximately 5 nm, estimated from the crystal structure published in ref. [103]). Under the assumption that the linker is free to pivot around its point of attachment to the BSA substrate, these considerations yield a total theoretical tether length of 7 nm, which is in excellent agreement with the measured linker length. The experimentally determined linker length is a lower bound for the true length because of the additional restriction of lateral fluctuations by the optical trap. In summary, the agreement between theoretical and measured linker length, together with the radial symmetric shape of the distribution of the position fluctuations, provide strong evidence for the formation of a single specific biotin-avidin bond between the tracer particle and the substrate.

3.3.4 Formation of multiple molecular bonds

In the following it is shown how the formation of two or more specific bonds can be distinguished from the formation of an individual bond. Figure 6 shows an extended time series of the x, y and z position fluctuations of a trapped tracer particle recorded under the same experimental conditions as described in the previous section. Several seconds after the first binding event occurred, the magnitude of the axial and lateral fluctuations were abruptly reduced and the tracer particle was pulled closer to the substrate. In addition, the average x and y position changed slightly (figure 3.6, second bond). This event is interpreted as the formation of a second specific molecular bond between the substrate and the tracer particle. If a second bond forms between

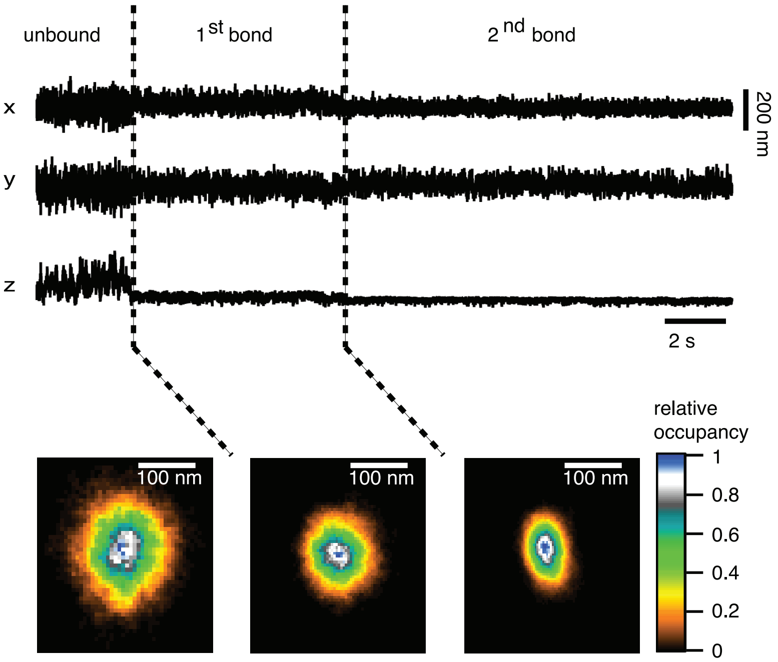

Figure 3.6: Formation of multiple specific bonds. An avidin coated latex particle of 1 μm diameter was weakly trapped in solution and then brought into contact with a substrate coated with biotinylated BSA / BSA in ratio 1:100. Note that this is the same particle and same dataset as shown in figure 3.4. The position fluctuations show two distinct events of reduction in the fluctuation amplitude indicating the formation of two specific bonds (top). (bottom) The two-dimensional lateral histograms for the unbound particle and the particle tethered by a single bond feature circular symmetry, while the lateral position histogram for the doubly tethered bead shows a strong ellipticity.

the particle and the substrate, the magnitude of the position fluctuations is expected to decrease because of the stronger confinement of the particle. The strength of the additional confinement depends on parameters such as the distance between the two anchor points on the surface and the magnitude of the residual non-specific particle-surface interaction. The formation of the second bond also shifts the center of the fluctuations to a position half way between the two bonds if both linkers have the same length, as is the case in our assay. This change in average position can be used to triangulate the location of the bonds on the surface. Finally, and most importantly, the lateral fluctuations along the axis connecting the two bonds are smaller than the fluctuations perpendicular to this axis, leading to an elliptically shaped probability distribution which clearly indicates the formation of a second bond and can be used again to triangulate the position of bonds on the surface. The formation of additional specific bonds follows essentially the same pattern. They lead to additional abrupt changes in the magnitude of fluctuations, a shift in the average position and a change in the shape of the lateral position histogram. However, the magnitude of these changes gets smaller with every bond formed so that the changes eventually become difficult to detect. Up to three binding events could be detected in this way, limited by the number of bonds available under the given experimental conditions and not the by the resolution of the method.

3.3.5 On the correlation of temporal and spatial resolution

The quality of the position histogram, and therefore the quality of the calculated energy landscape, depends on the number of statistically independent points in the histogram. Long observation times and a high sampling rate ensure a precise measurement of the energy landscape. However, oversampling does not improve the quality of the histogram because the particle needs sufficient time to explore the confining energy landscape. The relevant time scale is the position autocorrelation time of the particle, $\tau_k = \gamma_0/k_{\text{eff}}$, determined by the local viscous drag γ_0 on the particle and the effective spring constant k_{eff} of the potential formed by the optical trap and the linkage to the surface which is assumed to be a harmonic potential. For strongly confined particles, τ_k can be as short as microseconds, which underlines the need for fast three-dimensional position detection. In addition, fast position detection, i.e. a short integration time, is also required to measure correct probability distributions and energy landscapes. If slow position detectors ($\sim$1 kHz range) are used, they would, for example, allow a free 1 μm particle to diffuse approximately 30 nm within the integration time of 1 ms or 100 nm within 10 ms (see also section 2.3.1). Such long integration times eventually allow the tracer particle to sample the confining potential several times during the acquisition of one position data point, resulting in averaging of the particle's position with a bias towards the energetically favorable positions. Thus, the position signal no longer represents the particle's true position. Consequently, the probability distributions, as well as the derived energy landscapes, are distorted. In general, low-pass filtering leads to a collapse of the probability distribution making it very difficult to count multiple binding events and to distinguish between specific and nonspecific binding events.

3.4 Conclusions

Observing the reduction of thermal position fluctuations of the tracer particle has been used in the single-molecule field to detect binding events for some time. However, the molecules under investigation were typically long, spanning tens of nanometers to micrometers. The method presented here brings the analysis of the thermal position fluctuations of tethered particles to a completely new level by combining high-spatial-resolution position measurements in three dimensions with high-bandwidth detection. This way, the problems of confirming single molecule conditions and discriminating against nonspecific interactions are solved, which are both key issues for single molecule studies on small molecules and molecular complexes.

In summary, the method shown here brings quantitative mechanical single molecule studies from a small number of specific molecules to the majority of proteins, paving the way for the investigation of a wide range of new phenomena on the single molecule level.

Chapter 4

Lipid droplets as a handle for precise motor transport measurements

The previous chapter shows that specific bonds between small biomolecules can be probed using a PFM. We will now turn our attention to larger, but dynamic molecules, and show that processes far from equilibrium like transport by molecular motors can also be studied with outstanding precision. The work described in this chapter was done in collaboration with Rafael Longoria.[1] Rafael prepared the assay, including purification of lipid droplets, polymerization of microtubules and their immobilization on glass cover slides, and performed the video microscopy experiments. The author performed all experiments involving the PFM, devised and implemented a scheme to determine a droplet's suitability as a tracer particle, and analyzed all photonic force microscopy data sets.

---

[1] Text and figures in this chapter were coauthored with Rafael Longoria and appear as a duplicate in his dissertation by approval of his supervisor.

4.1 Introduction

Molecular motor proteins are responsible for long-range transport of vesicles and organelles in eukaryotic cells. In animal cells, motors of the kinesin family move cargo towards the plus ends of microtubules while cytoplasmic dynein carries the cargos towards the minus ends, typically arranged at the centrosome. Much of our understanding of how molecular motors function has benefited from single molecule measurements *in vitro* where individual motors are attached to microspheres nonspecifically. Yet transport of cargos in living cells is very different: they carry multiple similar and dissimilar motors [75, 125, 129], as well as motor light chains and cofactors [46, 143, 148]. The dynactin complex, a motor cofactor, is of particular interest as it bridges the cargo and the microtubule along which it diffuses without force generation [21]. Dynactin can also interact with both polarity motors [22] and alter their function [70, 76]. Moreover, the organization and stoichiometry of the different proteins on the cargo as well as the way they are attached to it can be important in determining the ensuing dynamics. It is currently not possible to reconstitute such transport complexes on plastic beads. It is, therefore, important to study the native motor complex in order to understand transport beyond the isolated motor function.

Precision measurements on individual endogenous cargos in living cells have recently been demonstrated [52, 125, 126], and used to study the coordination of opposite polarity motors [75] and motor regulation [147]. However, *in vivo* measurements suffer from three shortcomings that reduce the ability to dissect the details of motor dynamics and function with high precision. First, the heterogeneity of the cell can result in local changes in motor dynamics and compromise the high precision detection. Second, the crowded cell and microtubule tracks limit the observation time of individual cargos in isolation as other cargos can bump into them. Third, genetic manipulation can indirectly alter parts of the transport complex not targeted by the mutation making it difficult to dissect function. For instance, it was previously shown that genetic reduction of kinesin results in a concurrent reduction of cargo-bound dynein, even though the overall cellular expression of dynein is not altered [125].

To circumvent these limitations, yet study the native transport complex, the motility of purified cargo was reconstituted “ex vivo”. The term *ex vivo* is used as opposed to *in vitro* to differentiate between the motility of purified organelles as discussed in this work, from other works using isolated motors or motors attached to microspheres. Previous works using purified cargos extracted from different systems have focused on vesicles [53, 90, 99, 110, 129] limiting their use for high precision measurements in an optical trap, as vesicles are floppy and can deform in the trap. A large trap laser power is also necessary to manipulate them due to their small index of refraction. It has been recently demonstrated that sucrose filled vesicles can be easily trapped and do not deform due to osmotic pressure [9]. However, such sucrose filled vesicles do not naturally occur and are thus not useful for studying endogenous transport complexes.

Here, the *ex vivo* transport of lipid droplets purified from *Drosophila* embryos is reconstituted. Unlike vesicles, lipid droplets are refractile spheres of neutral lipids which have been previously used for optical trap measurements *in vivo* [75, 125]. Here, a PFM is used to characterize their suitability for high precision measurements ex-vivo and monitor motor dynamics at an unprecedented bandwidth.

Using the PFM it was possible to follow the dynamics of cargo-microtubule interaction with microsecond temporal resolution. For example, by following the position of a microtubule-bound cargo, it appears that the unbinding of one of the cargo-microtubule tethers can correlate with the onset of transport.

4.2 Materials and Methods

4.2.1 Lipid droplet purification

Wild-type *Drosophila* embryos 0-3 hrs old were collected on yeast-agar plates, washed with ddH2O and dechorionated with 50%/50% v/v bleach/water solution for 2-3 min. Embryos were gently homogenized with a Teflon-pestle in lysis buffer (62.5 mM K_2-PIPES, 1 mM EGTA, 5 mM $MgCl_2$, pH 7.2) supplemented with 1X protease inhibitor cocktail (Roche cOmplete ULTRA mini) and 5 mM DTT. Embryo lysate was centrifuged for 10 min at 10,000 rpm at 4 °C and the top layer of the post-nuclear supernatant (PNS) was collected via a cold glass pipette. This fraction is enriched with lipid droplets. DTT and protease inhibitor supplements were added to the PNS fraction.

4.2.2 Motility assays

Microtubules were grown by suspending 4 μg of unlabeled tubulin and 0.8 μg of rhodamine labeled tubulin (T240 and T590M respectively, Cytoskeleton, CO, USA) in 25 μl BRB80 (80 mM PIPES, 1 mM EGTA, 2 mM $MgCl_2$, pH 6.8) supplemented with 1 mM GTP and incubating at 37°C for 20 min. After polymerization, microtubules were stabilized by resuspension in BRB80 supplemented with 20 μM taxol.

The microtubules were deposited into flow chambers made with 0.02% Poly-L-lysine treated coverslips separated by a spacer. All surfaces were blocked using 5 mg/ml casein in blocking buffer (35 mM PIPES, 5 mM Mg_2SO_4, 1 mM EGTA, 0.5 mM EDTA, pH 7.2) supplemented with 1 mM GTP and 20 μM taxol. Lipid droplet motility was observed in motility buffer (62.5mM K_2-PIPES, 1 mM EGTA, 5 mM $MgCl_2$, pH 7.2) supplemented with 1mM ATP, 5 mM DTT, 20 μM taxol and an oxygen-scavenging system consisting of 50 U/ml glucose oxidase, 500 U/mL catalase and 12.5 mM glucose.

4.2.3 Polystyrene beads

NIST certified polystyrene beads were acquired from BangsLabs (IN, USA), with mean diameter ± standard error of $d = 506 \pm 6$ nm and $d = 990 \pm 30$ nm, henceforth referred to as 500 nm and 1 μm beads, respectively.

4.2.4 High bandwidth and high precision optical trapping

The Single Molecule PFM described in section 2.5 was used for the experiments described in this chapter. This PFM has a position detection precision of 1.5 nm (2 nm) laterally and 1 nm (8 nm) along the optical axis at a bandwidth of 1 MHz for tracer particles with 1 μm (200 nm) diameter.

4.2.5 Linearization of the detector

The relation between QPD response and particle position is approximately linear only close to the center of the trapping volume (see section 2.3). We have seen (section 2.3) that if a 500 nm diameter polystyrene particle is deflected more than $\sim$100 nm laterally from the focus we may no longer treat the detector as linear. It is reasonable to expect (and we will see below) that a lipid droplet of a similar size that actively generates forces against a weak optical trap will be deflected much further than 100 nm from the focus. Therefore, for high precision experiments, the detector's response must be linearized. A method to linearize and simultaneously calibrate the detector is described in section 2.3.2. For calibration, this method relies on knowledge of the trapped particle's radius. However, here we are interested in calibrating the response of a diffusing lipid droplet whose radius is unknown. Thus, we do not know its diffusion constant D which is necessary to calculate the local slope of the detector's response curve using equation 2.45. We may however set the diffusion constant to any arbitrary value, which is equivalent to using arbitrary units for the droplet's diameter. The linearization and calibration procedure described in section 2.3.2 then yields a transformation that linearizes the detector, but transforms the detector's output voltage into arbitrary units of position. In other words while we can linearize the detector, the resulting linearized position signal is still uncalibrated, and we will refer to it as the uncalibrated position signal.

For each trapped particle, a 12 s-long time trace of its position fluctuations was recorded at 100 kHz at the beginning of each experimental run. From this time trace, the transformation to linearize the detector was computed (see section 2.3.2). For all work described in this chapter all recorded detector responses were first linearized into uncalibrated position signals, even if this is not explicitly mentioned hereafter.

4.2.6 Calibration of position signal and determination of particle diameters

The uncalibrated position signal was calibrated as described by Tolic-Nørrelykke *et al.* [139] since their method of calibration does not require any knowledge of the radius of the trapped particle. In brief, four windows of 10 s each of position signal were recorded at a sampling frequency of 100 kHz while applying a sinusoidal lateral motion (amplitude 100 nm, frequency 40 Hz) to the sample chamber. The power spectral density (PSD) of each window was computed, and the four PSDs were averaged. From the power in the peak at the oscillation frequency and the corner frequency of the PSD (see below) the sensitivity of the detector (see section 2.3) was determined.

A fit of the full hydrodynamic theory to the window- and block-averaged PSD [10] yields the corner frequency and the uncalibrated diffusion constant of the trapped particle. The full hydrodynamic theory requires knowledge of the diffusing particle's mass density. The mass density of lipid droplets was assumed to equal 930 kg/m^3.[2] The density enters only as a correction factor in the fit. The particle size computed using the fit is effectively insensitive to the precise value of the density used: the measured size changes only by 0.1% when the density changes by 50%. The goodness of fit is given by the weighted sum of square errors (henceforth called SSE), which is defined as (following [10]):

$$SSE = n_W n_B \sum_{k=1}^{N'} \left(\frac{P_k^{Experiment}}{P_k^{Theory}} - 1 \right)^2 \tag{4.1}$$

where n_W is the number of windows and n_B the number of points per block. The sum runs over all data points in the averaged and blocked PSD, and P_k is the measured or theoretical PSD as indicated by the superscript. The uncalibrated diffusion constant in arbitrary units found by the fit was calibrated using the sensitivity. The particle's diameter d was calculated from the calibrated diffusion constant D by the Stokes-Einstein relation

$$d = \frac{k_B T}{3\pi\eta D}, \tag{4.2}$$

where T is the temperature. The viscosity η of the buffer was assumed to be equal to the viscosity of water at 26 °C.

---

[2] This value was estimated from the mass density of the neutral lipid tricaprin, see [98].

4.2.7 Determination of spring constants

The spring constant of the optical trap can in principle be found from the corner frequency of the PSD (see section 2.2.2) and thus could be extracted from the calibration procedure described above. However, from repeated measurements on the same trapped particle this approach was empirically found to lead to a large scatter in determined spring constants.

It appears that the extraction of the spring constant by Boltzmann statistics from the spatial probability distribution of the trapped particle (see equation 2.39) leads to a more precise measurement. This method was chosen here.

For each measurement, a 12 s long time trace of positions of the trapped particle was recorded at a sampling frequency of 100 kHz, linearized and calibrated. From these data one-dimensional spatial probability distributions were computed and the spring constants extracted.

4.3 Results

4.3.1 Long range motility of lipid droplets *ex vivo*

Lipid droplets in *Drosophila* embryos exhibit bidirectional motion along microtubules. It has previously been shown that the molecular motors kinesin-1 and cytoplasmic dynein, together with a multitude of motor cofactors form the motor complex responsible for this transport of the lipid droplets in the embryos [17, 47, 75, 125, 149]. To reconstitute cargo transport *ex vivo*, lipid droplets from early *Drosophila* embryos were purified (see section 4.2.1). In order to test whether the motor-cargo complexes attached to the purified droplets remain functional, lipid droplets were trapped with optical tweezers, positioned over a taxol stabilized microtubule attached to a glass coverslip, and released from the trap. Lipid droplets attached specifically to microtubules and many moved several micrometers, often after multiple seconds of fluctuating in place (see below). Figure 4.1A shows an example of long-range motility of a lipid droplet measured by video microscopy. Figure 4.1B shows traces of other droplets, moving with velocities of a few hundred nanometers per second, typical of both kinesin- and dynein- transported cargos. These

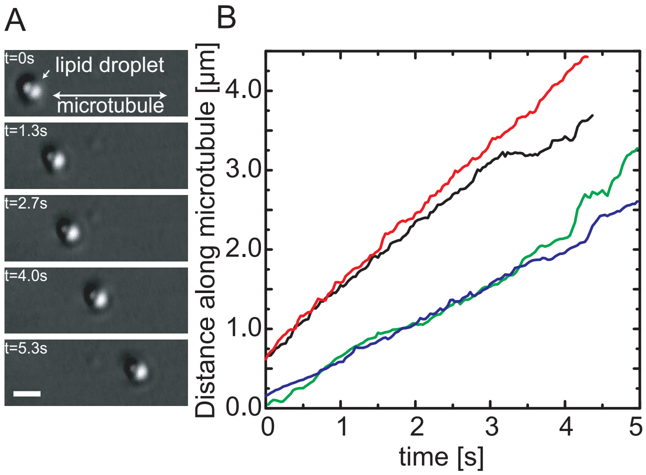

Figure 4.1: Purified lipid droplets can exhibit long-range transport *in vitro*.
A - Video frames showing a lipid droplet being transported along a microtubule attached to the microscope slide and imaged in DIC. Scale bar is 1 μm.
B - Position traces of various droplets show that they are transported at velocities characteristic of molecular motors of around 400-1000 nm/s. Data taken by Rafael Longoria.

experiments demonstrate that motors attached to the droplets survive the purification process and remained functional.

4.3.2 Purified lipid droplets are suitable tracer particles for high-resolution experiments

Tracer particles for high-resolution optical trapping experiments need to be spherical, homogeneous, and stable over time. In addition, their index of refraction should be significantly higher than the surrounding medium. Since the droplets cause a strong contrast in DIC microscopy, the latter requirement is fulfilled. However, the other requirements are more difficult to confirm because the images of the droplets are diffraction limited and look perfectly homogeneous and round most of the time in bright-field and DIC contrast. Another challenge is that their diameter varies and needs to be determined for calibrated force and position measurements.

4.3.2.1 Roundness and homogeneity of the droplets

If a droplet is not spherical, its rotational motion would cause artifacts in the position signal by scattering light into different directions depending on its rotational orientation. Due to the slow timescales of rotational diffusion, the power spectrum of an aspherical particle is expected to be elevated at low frequencies [82, 92]. A similar effect is expected for particles with a heterogeneous index of refraction. Thus, the power spectra of trapped droplets were inspected and compared to the analytical expression for the spectrum of a spherical particle confined by a harmonic potential. To obtain the highest precision, the analytical expression derived from the full hydrodynamic theory [10] was used (see section 2.2.3). To quantify the agreement between the analytical theory and the data, the goodness of the fit was calculated, given by the weighted sum of square errors (SSE, see equation 4.1). For reference, first the PSD of a 1 μm diameter polystyrene bead, as is commonly used as a tracer particle in single molecule experiments (figure 4.2A, circles) was inspected, and compared to the analytical fit. The graph shows that the analytical expression fits the data exceptionally well with a SSE of 0.027, which we will use as a reference for an excellent fit. Figure 4.2A shows the PSDs for two different lipid droplets (circles and stars). By visual inspection of the graphs, it is obvious that the fit to the PSD of the first droplet is much better (SSE = 0.029) than the fit to the PSD of the second droplet (SSE = 0.175). For the latter, the fit fails especially at low frequencies (dashed oval), as expected for a non-spherical and/or non-homogeneous particle. Since it is possible that the roundness and the homogeneity of the lipid droplets depend on their diameter, the SSE of the fit was plotted versus the measured diameter (see section 4.2.6) for each droplet (figure 4.2B). As a reference, the graph also shows SSEs of 500 nm and 1 μm beads (squares and triangles). Evidently, most lipid droplets (circles) have a goodness of fit comparable to that of the reference beads. Larger lipid droplets ($> 1\,\mu$m diameter) tend to show significantly larger SSEs (stars) and therefore are problematic for high resolution experiments. To establish an empirical standard, all lipid droplets with an SSE falling within four standard deviations of that of the standard beads were accepted as suitable for high

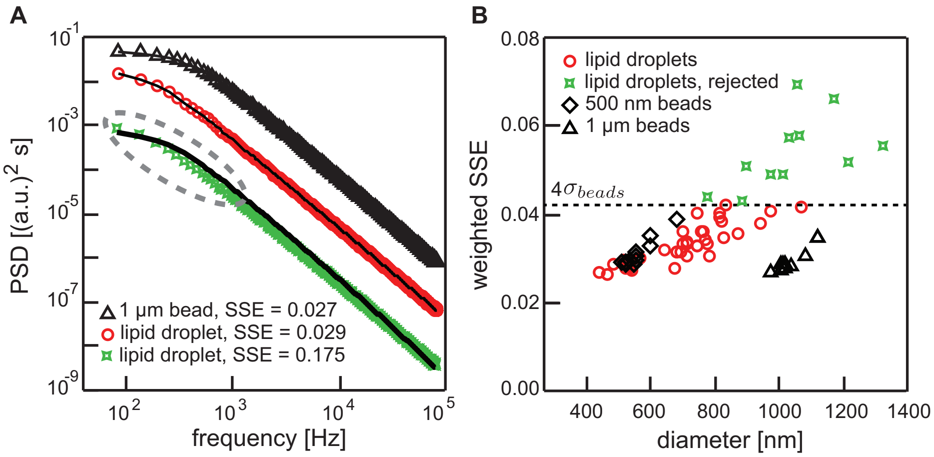

Figure 4.2: The goodness of fit to the droplets' power spectral density (PSD) reveals that most lipid droplets are spherical and homogenous. **A** - Power spectral density plots of the thermal motion of an optically trapped 1 μm diameter polystyrene bead (black triangles) and of the thermal motion of optically trapped lipid droplets (red circles and green stars). Analytical fits of the full hydrodynamic theory for the diffusion of a spherical particle in a harmonic potential are shown as black lines. By visual inspection, it is clear that the theory fits the bead's PSD (black triangles) and the PSD of the first lipid droplet (red circles) very well, but fails to fit the PSD of the second droplet (green stars). The PSD of an aspherical particle is elevated at low frequencies (dashed ellipse), and can no longer be correctly fit by the analytical theory. This indicates that the first droplet was as spherical and homogeneous as the polystyrene bead, while the second droplet was not. **B** - The weighted sum of square errors (SSE) of the fit of the analytical theory to the PSD as shown in **A** is plotted for lipid droplets (red circles and green stars) and reference beads (500nm diameter: black squares, 1 μm diameter, black triangles) versus their diameter which was determined from the fit. Most droplets have SSEs comparable to the SSEs of the reference particles. The larger the droplet, the more likely it is to have a high SSE. We empirically set a cutoff at $\langle \text{SSEbeads} \rangle + 4\sigma_{\text{beads}}$ (dashed line). Droplets with SSEs above this cutoff were discarded and not used in further analysis.

resolution measurements.

4.3.2.2 Droplet size distribution

The diameter of purified lipid droplets varies significantly and therefore needs to be measured with sufficient precision for each droplet in situ. Figure 4.3 shows the diameter distribution of all droplets that were found to be spherical and homogeneous by the criterion set in the previous paragraph. The distribution peaks at a diameter of approximately 660 nm, and the mean diameter of all suitable droplets was 700 nm with a standard deviation of ±150 nm, which agrees reasonably well with previous observations *in vivo* [75]. The distribution appears to be cut off towards small droplet diameters. This is due to smaller droplets being more difficult to visualize in simple bright-field contrast as used in these experiments. Equipping the PFM with dark-field

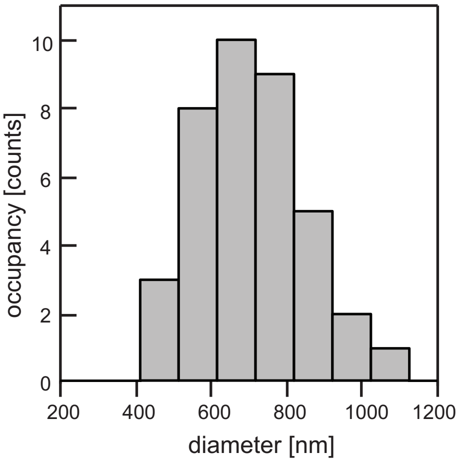

Figure 4.3: Lipid droplet size distribution. The diameter of all droplets was measured using the procedure outlined in section 4.2.6. Only droplets that met the criterion for a spherical and homogeneous particle are presented.

illumination will enable the use of small lipid droplets as tracer particles. Alternatively, DIC microscopy can be used to visualize small droplets, however, the required additional optics can distort the trapping and detection laser beam, compromising the PFM's high spatial tracking precision.

In order to determine the uncertainty in the size distribution, the diameters of two different types of polystyrene beads (500 nm and 1 μm diameter) were measured and compared to the diameters provided by the manufacturer. For the 500 nm beads the manufacturer gave a $d = 506 \pm 6$nm (mean diameter ± standard error), and experimentally the diameter was found to be $d_{\mathrm{exp}} = 558 \pm 14$nm (N = 12 beads). For the 1 μm diameter beads the manufacturer provided a diameter of $d = 990 \pm 30$nm, while experiments yielded $d_{\mathrm{exp}} = 1036 \pm 48$nm (N = 11 beads). This method thus systematically overestimates the particle diameter by about 50 nm in this size range. The origin of the systematic error is currently not known. If higher accuracy is desired in the future, further measurements using reference beads could be made to correct for this small systematic error.

4.3.3 Detector sensitivity and spring constant of the optical trap

Two important parameters for high resolution experiments are the position sensitivity that quantifies the response of the detector signal to a change in position of the tracer particle within the trap, and the stiffness of the trapping potential. High position sensitivity ensures that the signal rises above the laser power noise and the noise of the electronics. For a PFM, the position sensitivity along the optical axis depends critically on the intensity of the forward scattered laser light and with that on the diameter and the ratio of the indices of refraction of the trapped particle and of the medium that surrounds it. Figure 4.4 shows the dependence of lateral position sensitivity on particle

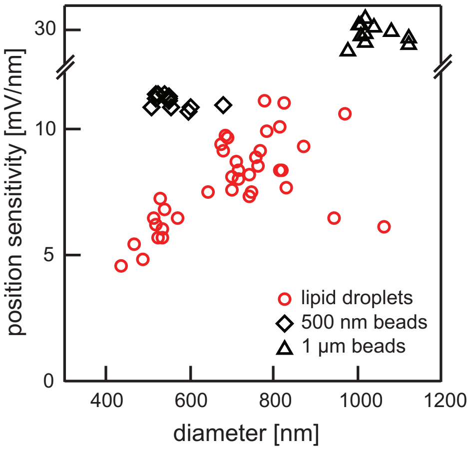

Figure 4.4: Comparison of the position sensitivity of lipid droplets and polystyrene beads. The lateral position sensitivity of lipid droplets (red circles) increases with their diameter. It is comparable to, albeit smaller than, the position sensitivity of 500 nm diameter polystyrene beads (black squares) and 1 μm diameter polystyrene beads (black triangles).

diameter, both for lipid droplets (circles) as well as for two different sizes of polystyrene beads (500 nm beads: rectangles; 1 μm beads: triangles). The sensitivity increases with increasing droplet and particle diameter. Importantly, the position sensitivity for lipid droplets is only slightly smaller than that of 500 nm polystyrene particles, which qualifies them clearly for high precision tracking experiments.

Like the position sensitivity, the spring constant of the trapping potential that confines the tracer particle depends on the ratio of the indices of refraction of the particle and of the surrounding medium and the diameter of the particle. High trapping efficiency has two advantages: Less laser power is necessary in order to confine a particle with the same stiffness and therefore photodamage to the molecular motors and regulatory factors on the lipid droplets can be minimized. The second advantage is that high trapping stiffness increases the available force range and a wider range of collective force generation by teams of motors can be probed.

Figure 4.5 shows the spring constant for lipid droplets in the diameter range from 400 nm to 1 μm as well as for 500 nm, and 1 μm polystyrene beads. The spring constant of lipid droplets is slightly smaller than that of polystyrene beads of the same diameter. The spring constant for lipid droplets increases approximately linearly over the relevant size range from 400 nm to 800 nm diameter, consistent with earlier observations [75, 111].

A low laser power of ~13 mW was used at the sample which is well below the power that was previously employed to trap lipid droplets *in vivo* without observing any photodamage [75, 125]. Nevertheless, a typical droplet of 700 nm diameter experiences a stiffness of 7.5 pN/μm even at this low laser power. The stiffness can easily be increased by increasing the laser power to what was previously used for *in vivo* force measurements and by increasing the numerical aperture of the objective lens.

In summary, lipid droplets are comparable to plastic beads in terms of position sensitivity as well as trap stiffness and therefore are ideal for high

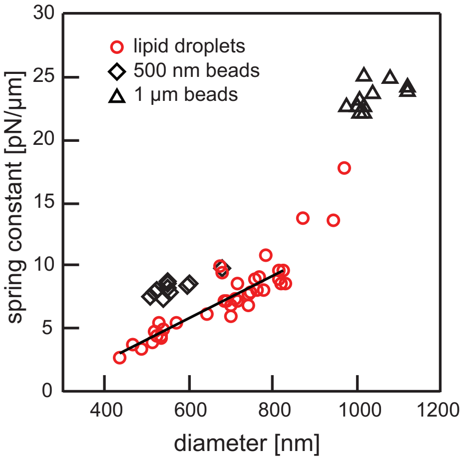

Figure 4.5: Comparison of the spring constant experienced by lipid droplets and polystyrene beads at the same laser power. As expected, trapped lipid droplets feel a stiffer confinement when their diameter increases. Between a diameter of 400 nm and 800 nm this increase is approximately linear at a slope of 17 pN / μm^2 (black line). The confinement of 500 nm diameter (black squares) and 1 μm diameter (black triangles) polystyrene beads is stronger, but of the same order of magnitude.

resolution experiments.

4.3.4 Lipid droplets in high resolution binding and motility assays

In section 4.3.1 it was demonstrated that many purified lipid droplets get transported along microtubules over large distances and therefore carry the endogenous motors and possibly many other factors that regulate transport *in vivo*. High resolution force and tracking experiments could be extremely valuable in characterizing the mechanisms of motor regulation as they allow distinguishing between different states of motors and the sequence of events from initial binding to the onset of force generation and transport. To demonstrate that purified lipid droplets are at least as good as the plastic or silica beads used in traditional motor assays, a series of binding experiments were performed.

Figure 4.6A shows high bandwidth time traces of binding and transport events for a lipid droplet that interacts with a microtubule. The coordinate

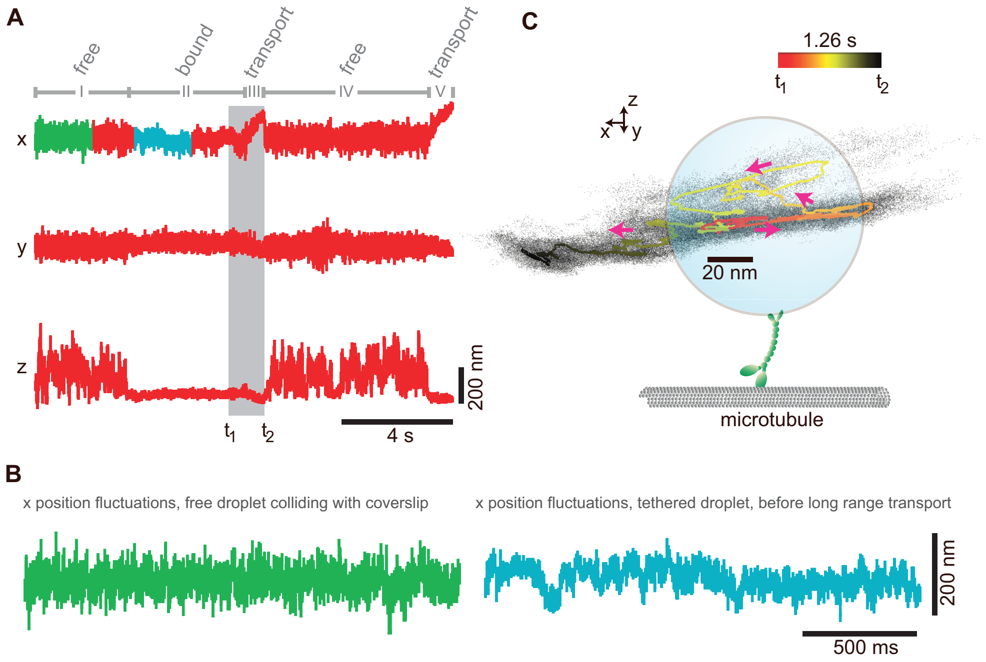

x position fluctuations, free droplet colliding with coverslip

x position fluctuations, tethered droplet, before long range transport

Figure 4.6: Motors and motor cofactors bind the microtubule dynamically. See page 102 for a detailed description.

system is oriented such that the x and y axes are parallel to the coverslip, and the z-axis points into the direction of the optical axis. The microtubule is oriented along the x-axis. Five regimes of behavior, labeled with the Roman numbers I through V, can be observed. In regime I, the droplet was positioned above the microtubule and its diffusion was confined by the optical trap in

x, y and positive z direction. The accessible volume for diffusion towards the microtubule (negative z-axis) is cut off due to collisions with the glass coverslip and the microtubule. The mean z-position of the droplet and the magnitude of its vertical fluctuations abruptly change at the transition from regime I to regime II. This indicates the binding of the droplet to the microtubule via a motor or a motor-cofactor present on the lipid droplet [64]. The possibility of non-specific binding to the surface of each flow cell was excluded by bringing lipid droplets in contact with the glass surface away from any microtubule and monitoring the z trace for any binding event for at least 20 seconds. Lipid droplets consistently did not bind to blocked surfaces; bonds formed only when a droplet was placed directly above a microtubule.

Interestingly, no long-range motor-driven motion in the lateral directions is observed in regime II. This can be inferred from the x and y traces since, on the time scale of seconds, there is no significant change in their mean values after the initial shift induced by the binding event. Thus, the droplet was tethered to the microtubule, but the tether was not generating active forces against the trap, even though the ATP concentration in solution was saturating. However, the PFM makes it possible to resolve the fast time scale dynamics in regime II: Figure 4.6B shows an expanded view of 2 seconds of position data along the microtubule before the droplet was tethered to the microtubule (green trace) compared to 2 seconds of data after the droplet had tethered (teal trace). On fast time scales transient shifts in the mean are visible for the tethered droplet, which are inconsistent with a single passive tether which would lead to uniform position fluctuations over such a time interval [7, 64]. Rather, the data suggest that multiple tethers bridge the droplet to the microtubule and that their combined effect is the inhibition of long-range transport. Such antagonist tethers could be unregulated opposite polarity motors or a motor and dynactin, for example. Methods that allow distinguishing between these two scenarios are presented in section 4.4. Several seconds after the initial binding event, the mean of the x trace rapidly increases, while the means of the y and z trace change only slightly (regime III). This is the signature of active transport of the droplet directed along the x-axis, which is consistent with the orientation of the microtubule. A closer inspection of the transition from regime II to regime III supports the interpretation of regime II as resulting from more than one tether (figure 4.6C): Immediately before active transport begins, the droplet is partially released from the microtubule implying the release of a bond as indicated by the average position trace (orange to yellow). The drastic change in the tethering is more clearly seen in the three-dimensional scatter plot of the position data (black dots). The volume accessible to the bead increases significantly just before the motor pulls the droplet along the positive x-axis and directional transport begins, which is followed by a stronger restriction of its motion also along the z-axis (yellow to black). Thus the detailed analysis of the transition is consistent with the idea that the initial binding event was caused by more than one molecule and that directed transport was only initiated after one of them unbound from the microtubule.

The run of about 200 nm with approximately constant velocity ends with the complete unbinding of the droplet from the microtubule which can be seen from the large increase in axial fluctuations (region IV), and is indicative of transport driven by only a single motor. Rebinding of the droplet to the microtubule in region V leads to immediate transport of the droplet along the positive x-axis. The motor in this case pulls the droplet out of the detection region of the trap.

4.4 Discussion

In this work it was demonstrated that lipid droplets purified from *Drosophila* embryos are close to as good as plastic beads for high resolution experiments with the strong advantage that at least part of the endogenous transport machinery is preserved on the cargo. No further preparation is required. However, this advantage comes with a new challenge. Different types of motor proteins and cofactors participate in binding and transport and, in addition, they may change their conformation and may be in different chemical states. To dissect the entire process from cargo binding to regulation of transport, it is important that different binding states can be distinguished and ordered in time. The number of states that can be distinguished depends on the number of parameters that can be extracted from position time traces and the precision with which each parameter can be measured. For instance, by measuring the stall force of lipid droplets inside *Drosophila* embryos, the number of engaged motors was determined from the number of peaks in the force histograms. The number of states that can be distinguished this way depends on the force range and was limited in previous measurements to about seven (three for plus-end motors, three for minus-end motors, and one for the unbound state) [125]. To distinguish these states, it was necessary to accumulate hundreds of force measurements, averaging over many different motor configurations. From these stall force measurements one can infer mechanisms of motor regulation as was previously demonstrated [75, 125, 147]. However, transport is a dynamic process and the cargo has multiple motors and cofactors that can interact with the microtubule at various time scales and in different ordering, often not leading to active transport. In this situation, high temporal and spatial resolution experiments in three dimensions, as described in this work, are critical. The measurements in figure 4.6A demonstrate the potential of these experiments in determining the different states of the transport complex dynamically.

As shown in chapter 3 and in ref. [64], passive binding events can be analyzed in detail and parameters can be extracted that characterize each state. Here, such parameters include the stiffness of the tether along three axes, the tether length, and its resting position in three dimensions relative to the anchor point on the microtubule. The precision with which the parameters can be measured depends on the time spent in a particular state; long-lived states can be characterized with high precision. Being able to distinguish between states is a necessary condition for a systematic analysis of motor regulation. However, before the mechanistic details of motor regulation can be understood, it is important to identify all molecules (and their state) that determine the properties of a tether. This can be achieved using an interplay between three different approaches: measurements on purified motors and cofactors attached individually to microspheres, measurements on lipid droplets where specific factors have been inhibited, and measurements on droplets purified from different *Drosophila* mutants. Further, there are several ways to improve the assay, such as polarity labeling of the microtubules.

In addition to showing that various states of cargo-microtubule interaction can be identified, the work described here also demonstrated that transition between states can be characterized using the three-dimensional motion of the droplet (figure 4.6C). The high precision and high bandwidth measurements provided unprecedented detail that made it possible to correlate the unbinding of a tether with the onset of transport. However, the identity of the molecules that form the tether is not known. Cataloging the mechanical properties of the various motors and cofactors present on the droplets as described above can solve this problem. Furthermore, novel methods for extracting tether (motors and cofactors) properties during transport will make it possible to correlate the tether state with the velocity of the droplet and the force produced.

Finally, the genetics of the fly is tractable and many well-characterized mutants are available. Mutants that lack factors important for motor-driven transport, and the lipid droplets purified from them, can be systematically studied. The correlation of the loss of these factors with changes in the states observed in *ex vivo* experiments will then provide insight into the function of each factor being investigated. This versatility is a strong advantage in comparison with other *in vitro* assays with purified cargos [13, 52, 53, 90].

4.5 Conclusions

A new *ex vivo* assay was introduced that enables the study of molecular motor cooperativity and regulation of same- and opposite-polarity motors with a higher level of complexity than that obtained via traditional *in vitro* studies. The pesented approach uses purified endogenous lipid droplets from *Drosophila* embryos as high precision tracer particles for use in photonic force microscopy experiments. The purified droplets were shown to be comparable to the plastic or silica beads typically used in *in vitro* studies, when carefully selected based on the goodness of the fit to their power spectrum at low frequency. Furthermore, high resolution position traces of droplets binding to and getting transported along microtubules *in vitro* were presented. A wealth of information can be extracted from these traces such as properties of the tether and the averaged path of the droplet which allows studying the transitions that lead to the motile state. Finally, the high resolution tracking data can be used to investigate motor cooperativity and regulation. Genetic manipulation of *Drosophila* embryos may be used to decipher the role of each factor in this complex process of motor driven transport regulation.

Chapter 5

Thermal noise imaging of microtubules

It is the goal of the presented research to acquire three-dimensional thermal noise images (see section 2.4) of the networks of biofilaments. The stability, resolution and position detection bandwidth of a photonic force microscope as discussed in the previous chapters is indispensable for this imaging technique. To demonstrate the power of thermal noise imaging, images of individual microtubules (not cross-linked to a network) are presented and quantitatively analyzed in this chapter. The author performed all research described in this chapter in collaboration with Martin Kochanczyk. Both researchers shared the workload of each described experiment, of the development of the analytical theory, and of all analyses evenly, unless noted otherwise.

5.1 Introduction

Microtubules are a major component of the cytoskeleton of eukaryotic cells and perform a diverse set of biological functions (see section 1.1.1). They provide the mechanical strength to resist cellular deformations [1, 79], maintain cell polarization during directional cell migration [153], generate forces to move chromosomes during mitosis [1, 37, 124], act as tracks for molecular motor-based intracellular transport [117], and facilitate the exchange of mechanical signals with the cell's extracellular environment [61]. A large set of proteins binds to microtubules, leading, depending on the protein, to microtubule stabilization, destabilization, bundling and cross-linking [30, 81]. Structures formed from microtubules can also specifically bind to other modules within the cell. For example, the protein WHAMM[1] binds to microtubules, actin filaments and membranes, and can cross-link these structures [15, 37].

The mechanical properties of the formed structures depend on the properties of the individual filaments, and on their degree and fashion of connectedness. The biological functions of individual microtubules outlined above appear to require them to be mechanically stiff: for example, to provide mechanical strength they must withstand buckling and stretching, and in order to provide stable tracks for molecular motors they have to remain stationary under an applied load. However, during their polymerization they must avoid obstacles in the cytoplasm and find their binding partners, presumably by thermal motion, in order to form structures, requiring them to be mechanically flexible.

This apparent contradiction, and the desire to understand the properties of higher level structures made from individual filaments, has led to increased recent interest in the mechanical properties of individual microtubules. The focus has been to extract a single parameter quantifying their stiffness,

---

[1] WASP homolog-associated protein with actin, membranes and microtubules

the persistence length l_p (see section 1.3.2). Early studies found a seemingly random spread of one order of magnitude in l_p for individual *in vitro* polymerized and taxol stabilized (see section 1.1.1) microtubules [36, 44]. It was later realized that the anisotropic structure of microtubules gives rise to a contour length l_c dependent persistence length [95, 96, 135] (see figure 5.1), unifying the previous measurements.

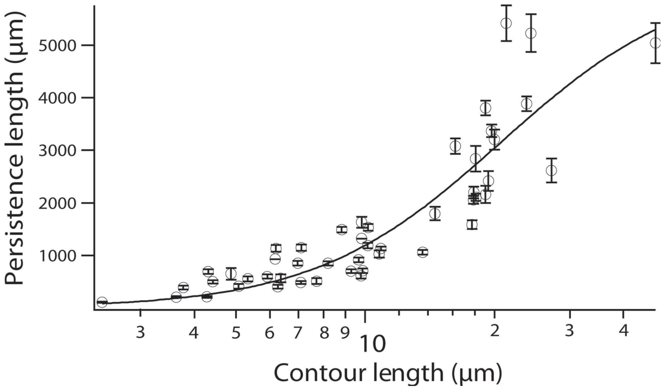

Figure 5.1: The persistence length of individual microtubules increases as a function of contour length. Solid line: Analytical fit which takes the anisotropy of the microtubular architecture into account. Reprinted from [96].

Short microtubules are flexible, presumably allowing them to efficiently explore the volume in their vicinity by large transversal thermal fluctuations. Thus, during its polymerization, a short microtubule can circumvent obstacles in its path, and efficiently find binding partners in its surroundings. Microtubules that have a contour length comparable to the diameter of eukaryotic cells ($\sim$12 μm) are fairly stiff materials, with a persistence length of several millimeters, facilitating the biological functions outlined above [96].

The transversal thermal fluctuations of biofilaments are important for several reasons: First, they are of biological relevance, as explained above. Second, if a filament is confined on both ends, its transversal fluctuations report on its tension: The larger the tension, the smaller one expects its transversal fluctuations to be. This feature is of special importance when considering networks of filaments as discussed in section 1.3.4. Lastly, they can be used to measure a filament's persistence length. Measurements of transversal fluctuations serving this purpose have so far relied on video microscopy [44, 63, 96, 135], making it difficult to characterize short microtubules ($l_c < 4$ μm), due to the small amplitude of their shape fluctuations. Additionally, video microscopy cannot resolve transversal fluctuations of filaments cross-linked to three-dimensional networks, which is currently a matter of great interest (see section 1.3.4).

In the following, thermal noise imaging is introduced as a novel quantitative method to both image individual short microtubules, and extract their transversal fluctuations. An analytical theory is formulated to extract the persistence length from the acquired datasets. This method can be implemented to image networks of filaments, as demonstrated in chapter 6.

5.2 Materials and Methods

5.2.1 Microtubule preparation

Microtubules were grown by suspending $4\,\mu$g of unlabeled tubulin and $0.8\,\mu$g of rhodamine labeled tubulin (T240 and T590M respectively, Cytoskeleton, CO, USA) in $25\,\mu$l BRB80 (80 mM PIPES, 1 mM EGTA, 2 mM $MgCl_2$, pH 6.8) supplemented with 1 mM GTP and incubating at 37°C for 10 min to 30 min, depending on the desired microtubule length.

After polymerization, microtubules were stabilized by resuspension in BRB80 supplemented with 20 μM taxol. Thus, all microtubules in this work were taxol stabilized, even if this is not mentioned hereafter.

5.2.2 High bandwidth and high precision optical trapping

The Thermal Noise Imaging PFM described in section 2.5 was used for the experiments described in this chapter. This PFM has a bandwidth of 1 MHz and position detection precision of 1 nm laterally and 7 nm along the optical axis for tracer particles with 200 nm diameter. Before each data acquisition the PFM was calibrated *in situ* as discussed in section 2.3.2. For some of the shown datasets the PFM's bandwidth was low-pass filtered to 50 kHz. For a 200 nm diameter particle diffusing in water at room temperature, this decrease in bandwidth introduces a ∼10 nm "motion blur" in the detection of the particle's position (see section 2.3.1). This uncertainty is at the bin-width of the voxel occupancy (see section 2.2.4.2 and 2.4) and thus is not expected to significantly decrease the fidelity of the measurement. Typical spring constants of the potential confining the tracer particle were $k_x = 1.5\,\mathrm{pN}/\mu\mathrm{m}$, $k_y = 1.0\,\mathrm{pN}/\mu\mathrm{m}$ and $k_z = 0.15\,\mathrm{pN}/\mu\mathrm{m}$. The corresponding autocorrelation times of the tracer particle's diffusion were $\tau_x = 1.1$ ms, $\tau_y = 1.7$ ms, and $\tau_z = 11$ ms.

5.2.3 Single filament assay

The experimental assay used to study the transversal thermal fluctuation of microtubules by thermal noise imaging has to fulfill three requirements: First, at least one end of each microtubule must to be grafted to a support to keep it from diffusing away. With only one end grafted, the other "free" end is expected to exhibit large transversal thermal fluctuations. If the microtubule is spanned between two supports and both ends are immobilized, it is still expected to transversally fluctuate between the supports, but less than in the case with free end. Second, the introduced supports must have a negligible refraction of the trapping and tracking beam of the PFM (see section 2.3). Third, the supports must lift the microtubules far away from the boundaries of the sample chamber, in order to ensure that neither the thermal motion of the microtubules, nor the thermal motion of the tracer particles couple hydrodynamically to those boundaries. When using the PFM to detect the position of small particles (∼200 nm diameter) close to boundaries between materials with different optical indices, position artifacts on the detector were observed. These artifacts are likely caused by optical surface effects; however their precise origin is not yet understood. Lifting the microtubules away from the boundaries has the additional benefit of avoiding these position detection artifacts.

These requirements were fulfilled in an assay designed by Dr. Martin Kochanczyk: Microtubules were spanned in random directions over a holey carbon film (hole width: $7\,\mu$m, hole periodicity: $9\,\mu$m) on a copper electron

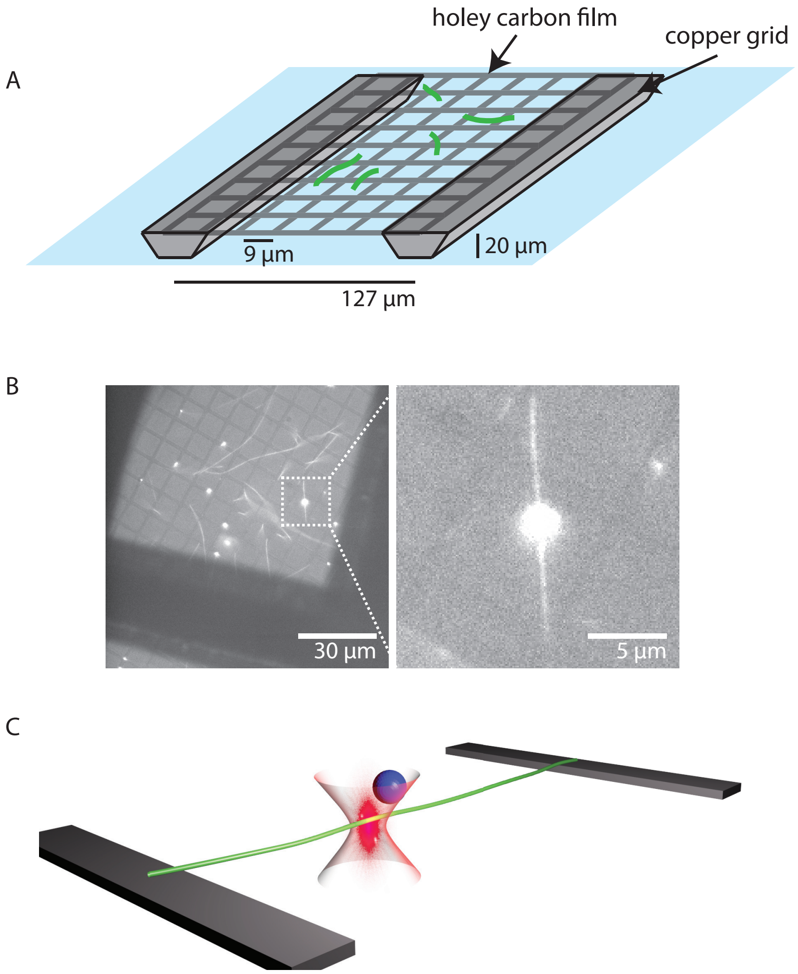

Figure 5.2: Single filament assay. **A** - Schematic of the assay. Microtubules (green) were adhered to a holey carbon film supported by an electron microscopy grid. **B** - Combined bright field and fluorescence image taken with the PFM. A single microtubule spans a hole of the carbon film, and a single tracer particle (bright spot) is held close to the middle of the filament using optical tweezers. **C** - Sketch of the experimental situation in **B**

microscopy grid (spacing of the copper grid: 127 μm; S 7/2, Quantifoil, Electron Microscopy Sciences, PA, USA) (see figure 5.2A). The 20 μm thick copper grid was glued to a glass coverslip using a biochemically inert, solvent-free silicone glue (Elastosil N10, Wacker, Germany). The copper's thickness provides sufficient lift to avoid any hydrodynamic coupling between the glass coverslip and the microtubules or tracer particles [50].

It was empirically determined that the tightly focused trapping beam did not intersect with the copper grid as long as the optical trap was positioned at least $\sim$10 μm from the edge of the copper grids. No datasets were acquired any closer to the copper than this threshold. The holey carbon film on the other hand is only 20 nm thick, and it is possible to position the optical trap in close proximity (down to $\sim$200 nm distance) to it without intersecting the film. When measuring this closely to the film, care must be taken to not intersect it with the trapping beam: The carbon grid absorbs infrared light strongly, resulting in explosive local heating when it intersects the optical trap.

Microtubules must be grafted to the holey carbon film strongly so that at least one end point and the tangent of that end point are fixed. This was achieved by coating the holey carbon film by 50% Poly-L-lysine (PLL) in deionized water. PLL has a strong non-specific interaction with microtubules and is commonly used to immobilize them on surfaces [119]. Initially, the carbon film was found to be too hydrophobic to be coated with the PLL solution. This problem was solved by exposing the entire assembly – coverslip with glued grid – to an oxygen plasma [104] for 2 seconds at $\sim$130 mTorr. The coverslip with the glued, plasma cleaned grid was then quickly assembled to a sample chamber by adding a metal spacer, and after the next steps, a top coverslip.

The carbon film was then immediately coated with 50 μl of PLL solution and incubated for 20 min at room temperature. In typical assays, the PLL solution is allowed to dry on the surface onto which the microtubules are to be adhered. This was not possible here, since the air-liquid interface of the drying PLL solution destroyed the carbon film on the grid by surface tension. Instead, the PLL solution was rinsed off the grid with copious amounts of deionized water.

At this point the top coverslip was added to the sample chamber. Fluid inside the chamber could be exchanged through small channels in the metal spacer: 200 μl of BRB80 buffer to displace the DI water, and subsequently 200 μl of microtubules in BRB80 were flushed into the chamber. The microtubules were allowed to adhere to the PLL coated carbon film for several minutes. Unattached microtubules were then removed from the sample chamber by a flush with 200 μl of a solution containing tracer particles (see section 5.2.4) and an oxygen scavenging system consisting of 50 U/ml glucose oxidase, 500 U/mL catalase and 12.5 mM glucose in BRB80 supplemented with 20 μM taxol.

Microtubules and tracer particles could then be observed in fluorescence microscopy, while the holey carbon film was visible in bright field contrast. Figure 5.2B shows a combined fluorescence and bright field image for a microtubule spanning a 7 μm hole in the carbon film. A tracer particle is held with the optical trap close to the middle of the microtubule (bright spot). A schematic of this is shown in figure 5.2C

5.2.4 Tracer particle preparation

Fluorescent polystyrene beads with a diameter of (190 ± 29) nm (mean ± nominal standard deviation) were acquired from Bangs Labs (sun coast yellow, Bangs Laboratories, IN, USA). Without further preparation these particles nonspecifically attach to microtubules when allowed to repeatedly collide with them. This behavior is incompatible with thermal noise imaging (section 2.4) since the scanning probe must diffuse around the scanned structure and not adhere to it. To prevent this interaction, the particles were coated with bovine serum albumin (BSA) by incubating them them at high concentration (at least) overnight in a solution of 5 mg/ml BSA in phosphate buffered saline (PBS). Beads from this stock solution were then diluted into BRB80 for each experiment. As shown in chapter 3, BSA can be used to shield the nonspecific interaction between a tracer particle and a substrate. Each BSA protein is approximately 1.4 nm x 0.4 nm x 0.4 nm in size [155]. Thus, each particle's diameter is expected to increase by at most $\sim$3 nm due to the coating, assuming that the particles are coated in a monolayer of BSA.

5.3 Results and Discussion

5.3.1 Thermal noise images

Thermal noise imaging is a three-dimensional scanning probe technique that can image nano-structures in three dimensions with super resolution. The optically trapped tracer particle's position is detected using a PFM, by reading out the interference pattern between the unscattered trapping beam and the light forward scattered by the particle. If the imaged structure additionally scatters the beam, detecting the tracer particle's position becomes more difficult (see section 6.3.1.1). It was found that microtubules scatter orders of magnitude less light than the tracer particle though, and can be imaged in a straightforward manner.

If the imaged structures are static during the scan (i.e. there are no thermal fluctuations), the excluded volume in the thermal noise images represents the inverse of the scanned structure (plus the radius of the tracer particle, see section 2.4 for a detailed discussion). Data interpretation is more complicated for fluctuating structures. In the following we will therefore first discuss the imaging of a microtubule confined on both ends, which only has a small (but not negligible, as we will see in section 5.3.2.4) magnitude of transversal fluctuations.

5.3.1.1 Microtubule grafted on both ends

Voxel occupancies (see section 2.2.4.2 and 2.4) were measured along a microtubule whose ends were grafted to the holey carbon film support (figure

5.3A). For all experiments described in this chapter, the power of the trapping beam was adjusted so that the width of the trapping volume explored by the particle was ∼300 nm laterally and ∼900 nm axially, allowing the particle to diffuse completely around a microtubule centered in the middle of the trapping volume.[2] The step size along the microtubule between voxel occupancy measurements was 100 nm, ensuring that subsequently acquired occupancies had a large overlap (figure 5.3B). Twenty-eight individual occupancy measurements were performed, each with an integration time of 4 s and a particle position sampling rate of 100 kHz, resulting in a total scan length of 2.8 μm. The scan was started 4.5 μm from the support; the full length of the microtubule between grafting points was 10.6 μm. The overlapping voxel occupancies were summed up to yield a cumulative voxel occupancy of the entire scan (figure 5.3C). Each iso-occupancy surface of this cumulative occupancy is a thermal noise image of the scan. The image for an isovalue of 5 is shown in figure 5.3D (outside: blue, inside: silver). The front of the three dimensional image was cut away to allow a better view of the “channel” caused by the presence of the scanned microtubule. The “kink” close to the middle of the channel is very likely not a feature of the microtubule itself, but rather an artifact of the measurement caused by a change in the full light intensity on the detector. This change in intensity may have had its origin in a drift in the laser power,

---

[2] “Width” here is defined as $6\sigma_i$, where $\sigma_i = k_BT/k_i$ is the standard deviation of the one-dimensional Gaussian position distribution along axis $i = x, y, z$ (compare equation 2.39). $6\sigma_i$ corresponds to good approximation to the peak to peak position fluctuations along the i-axis.

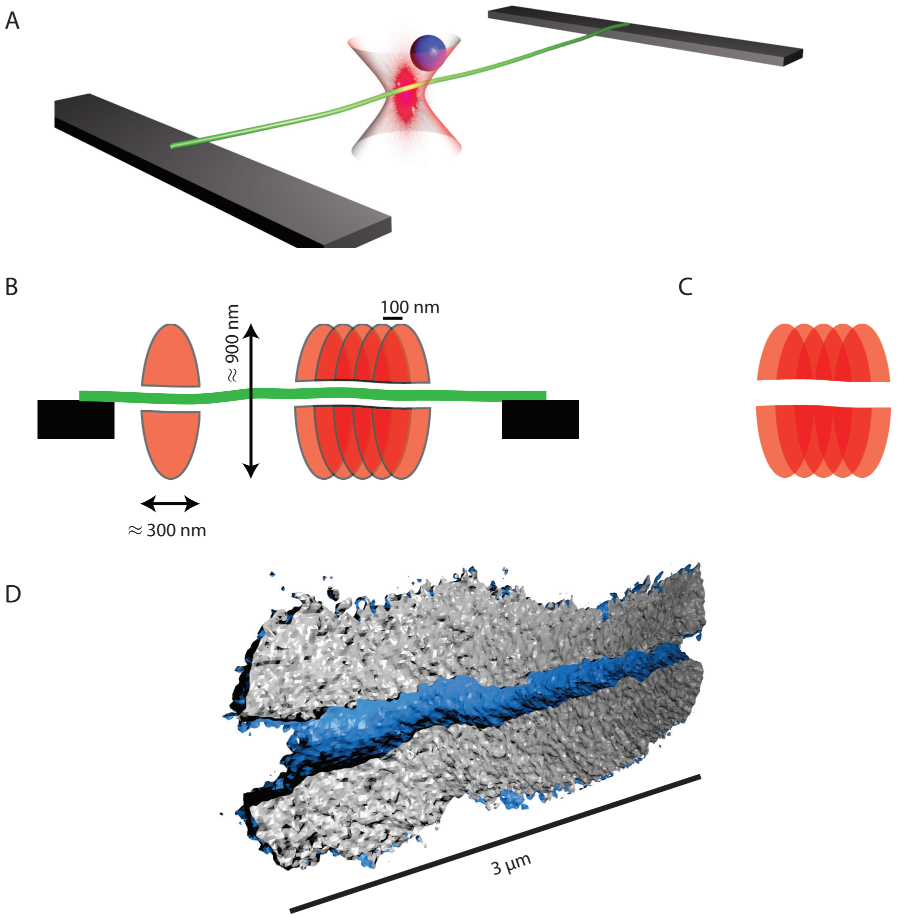

Figure 5.3: Thermal noise image of a microtubule grafted on both ends.
A - Schematic of the single filament assay. The trapped particle was stepped in 100 nm steps along a microtubule which was grafted on both ends to a support (holey carbon film). At 28 positions along the microtubule the tracer particle's voxel occupancy was measured (**B**). **C** - The individual overlapping voxel occupancies were summed up to yield a cumulative voxel occupancy of the entire scan. **D** - Thermal noise image computed from the cumulative voxel occupancy (cumulative voxel occupancy = 5 for this surface). The front half of the image was cut away to reveal the channel caused by the presence of the scanned microtubule. Individual voxel occupancies had an integration time of 4 s and particle positions were sampled at a rate of 100 kHz.

or in additional light being scattered by the copper grid or carbon film.

Coordinate system transformation and position feedback Stepping the trapping volume along the microtubule while keeping the microtubule in the center of the trap is not trivial: First, the microtubule is in general not aligned with one of the major axes of the instrument (i.e. not aligned with the x- or y-axis of the positioning stage). Second, the microtubule will not be perfectly confined to one z-plane. For example, a slight bend in the carbon support of less than 3 degrees causes the mean of the microtubule's contour to rise by 100 nm over a lateral run of 2 μm. Third, the instrument had a slow, but noticeable drift of approximately 10 nm/min, which had to be compensated for during data acquisition.

In order to address the first problem, a fluorescence microscopy image was taken of each microtubule before acquiring thermal noise images. From the fluorescence image, the microtubule's angle with the x-axis of the system was determined. Using this angle, software developed by the author performed a coordinate transformation in realtime, transforming the acquired data and the stage positions to rotate the x-axis of the system in the direction of the microtubule. All experiments were thus performed in the frame of the microtubule, with the microtubule aligned with the x-axis of this frame.

The second and third concerns were simultaneously addressed by a position feedback scheme designed and implemented by the author. After acquisition of each voxel occupancy, the LRO and SO were computed (sections

2.4.1 and 2.4.2) and collapsed into two dimensions along the direction of the microtubule (figures 5.4A and 5.4B). The LRO is the effective interaction

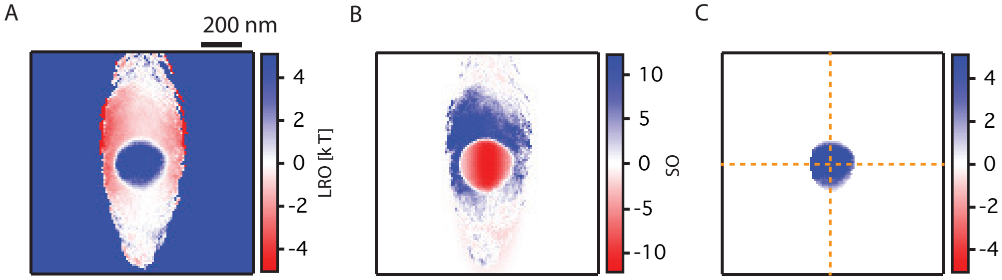

Figure 5.4: Principle of position feedback. Shown are the two-dimensional LRO (**A**) and SO (**B**) computed for each voxel occupancy measurement along the scanned microtubule. The circular excluded volume in the middle of the trapping volume is clearly visible as an extremely high energy barrier in the LRO, and as an underpopulated volume in the SO. **C** - LRO of pixels which have a corresponding SO < -4. The center of mass of this thresholded LRO was computed and indicates the mean position of the microtubule (dashed orange cross).

energy between the particle and the microtubule, in units of k_BT, while the SO gives the statistical significance of the change in voxel occupancy compared to an empty trapping volume. In order to detect the position of the microtubule relative to the optical trap, the center of mass of the two-dimensional LRO was computed for all pixels for which SO < -4 (figure 5.4C). This threshold in the SO prevents voxels at the edge of the trapping volume, which have LROs with large error, from contributing to the center of mass calculation. The center of mass of the LRO equals the average position of the microtubule. If the center of mass was not found to be within ±100 nm of the center of the trapping volume, the sample was automatically repositioned to move the microtubule into the center of the trap, and a new image was acquired. Only upon successful acquisition of an image that had the microtubule centered was the trap stepped to the next position along the microtubule.

5.3.1.2 Microtubule grafted on one end

So far we have considered a double-grafted microtubule which can be considered to be a fairly static structure. Its thermal noise image features an excluded volume which is linked to the inverse image of the filament. We will now discuss a microtubule grafted on only one end, and free on the other end. Such a microtubule is expected to exhibit large transversal fluctuations, especially at points along its contour far from the point of grafting. As we have seen in section 2.4, thermal noise imaging reports on the effective interaction energy between the tracer particle and the scanned structure. If the scanned structure fluctuates, this effective interaction energy changes, resulting in a change in the acquired images. Thus, in contrast to the channel with constant diameter seen in the thermal noise image of the double-grafted microtubule, we expect the thermal noise image of the microtubule with a free end to change when the trapping volume is stepped along the microtubule's contour towards the free end.

Voxel occupancies were acquired along a microtubule with a free end, at a step size of 100 nm between individual measurements (figure 5.5A), at 20 positions, starting at a distance of 1.5 μm from the support (arrows in figure 5.5A). Each occupancy measurement had an integration time of 4 s and a particle position sampling rate of 100 kHz. The full contour length of the scanned microtubule was 7.3 μm. Position feedback during data acquisition was performed as described in section 5.3.1.1. The thermal noise image (isovalue = 5) of the cumulative voxel occupancy of the scan is shown in figure 5.5B (outside: blue, inside: silver). Half of the image is cut away, revealing a channel caused by the scanned microtubule. However, in comparison to the image of the doubly confined microtubule (figure 5.3C), the channel shown here gets smaller the further the scanned position is from the support. Eventually, the channel even vanishes completely. We may understand this behavior by considering the transversal fluctuations of the microtubule. If the microtubule's shape fluctuation is dominated by motion on time scales that are slower than the tracer particle's autocorrelation time, the microtubule will slowly fluctuate out of the way as the particle explores the trapping volume. Thus, with larger fluctuation amplitude of the microtubule, more and more volume becomes accessible to the particle. Eventually, at a sufficient distance from the support, the microtubule's transverse fluctuations are so large that the entire trapping volume becomes accessible to the particle's diffusion. Thus, the further the imaged volume is from the support, the smaller the channel, until it vanishes entirely. As we will see below, the change in the effective interaction energy landscape caused by the presence of the microtubule can still be extracted from the data, even if the excluded volume vanishes.

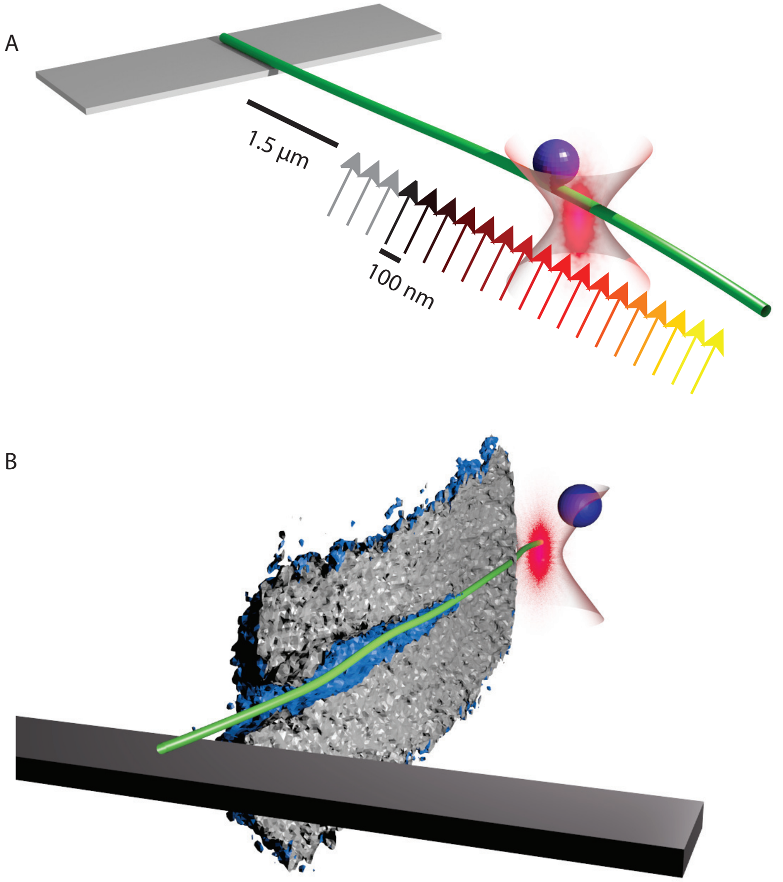

Figure 5.5: Thermal noise image of a microtubule with a free end. **A** - The microtubule was grafted on one end and free to fluctuate on its free end. The scan was started 1.5 μm from the support, and voxel occupancy measurements were performed in 100 nm steps along the microtubule (arrows). **B** - Thermal noise image computed from the cumulative voxel occupancy (isovalue 5). The front half of the image was cut away to reveal the channel caused by the fluctuating microtubule. Occupancy measurements had an integration time of 4 s and particle positions were sampled at a rate of 100 kHz.

5.3.2 Quantitative analysis of thermal noise images

5.3.2.1 Theoretical description of transversal microtubule fluctuations

Before quantitatively analyzing the acquired thermal noise images we will first review some of what is known about the transversal fluctuations of a grafted microtubule with contour length l_c and persistence length l_p. The shape fluctuation z of a microtubule in an aqueous solution as a function of position s along its contour (see figure 5.6) follows the hydrodynamic beam equation [63, 150]

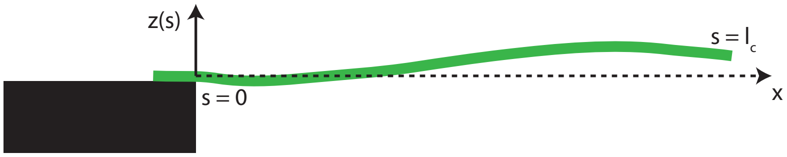

Figure 5.6: Shape fluctuations of a grafted microtubule (green) with a free end. When no forces act on the grafted microtubule its configuration coincides with the x-axis (dashed line). Under the influence of thermal forces, the microtubule's shape fluctuates and is described by the deviation $z(s)$ from the forceless configuration. Note that the deviation z is a function of the position along the microtubule's contour s, and not a function of the position along the x-axis.

$$\kappa \frac{\partial^4 z}{\partial s^4} = -\gamma \frac{\partial z}{\partial t}, \tag{5.1}$$

where $\kappa = k_B T l_p$ is the flexural rigidity of the microtubule, and γ is its perpendicular drag coefficient. γ was approximated by the perpendicular drag on a cylinder [20],

$$\gamma = \frac{4\pi\eta}{\ln\left(l_c/d + 2\ln 2 - 1/2\right)}, \tag{5.2}$$

where η is the viscosity of the surrounding fluid and d is the diameter of the microtubule.

For the boundary conditions of a grafted microtubule with a free end, equation 5.1 is solved by a set of n solutions (see [63])

$$z_n(s,t) = \mathrm{e}^{-t/\tau_n} W_n\left(\frac{s}{l_c}\right). \tag{5.3}$$

The spatial modes W_n (figure 5.7) form a complete orthonormal set on the domain [0,1] and are defined by

$$W_n(\alpha) = \frac{-\cosh q_n - \cos q_n}{\sin q_n + \sinh q_n}\left(\sin q_n\alpha - \sinh q_n\alpha\right) + \cos q_n\alpha - \cosh q_n\alpha, \tag{5.4}$$

where the q_n are the subsequent solutions of $\cos q_n \cosh q_n = -1$. “Complete” here means that the space of shapes of grafted fluctuating microtubules can be constructed by linear combinations of the modes W_n,

$$z(s) = \sum_{n=1}^{\infty} \sqrt{\frac{1}{l_c}} a_n W_n\left(\frac{s}{l_c}\right), \tag{5.5}$$

where the coefficients a_n are called mode amplitudes.

Each mode W_n is randomly thermally excited by the interaction between the microtubule and the solvent, and then decays away (see equation 5.3) with a correlation time τ_n of [63]

$$\tau_n = \frac{\gamma}{\kappa}\left(\frac{l_c}{q_n}\right)^4. \tag{5.6}$$

This continuous excitation and subsequent decay corresponds to random walks of the mode amplitudes a_n in confining potentials with stiffness $k_n = \gamma/\tau_n$ [71].

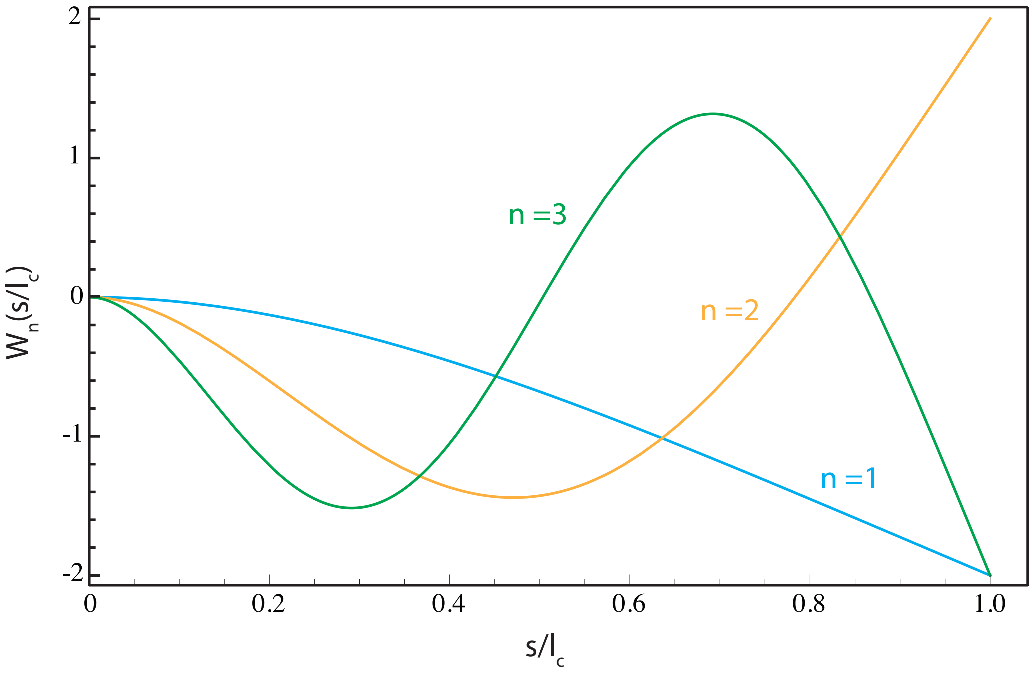

Figure 5.7: First three modes of microtubular shape fluctuations for a microtubule grafted to a support at $s = 0$.

The modes are independent and their amplitudes are uncorrelated random variables with zero mean, thus

$$\langle a_i a_j \rangle = \langle a_i^2 \rangle \delta_{ij}. \tag{5.7}$$

It follows by equipartition that

$$\frac{1}{2}k_n \langle a_n^2 \rangle = \frac{1}{2}k_B T \tag{5.8}$$

$$\langle a_n^2 \rangle = \frac{k_B T}{k_n} \tag{5.9}$$

$$\langle a_n^2 \rangle = \frac{1}{l_p}\left(\frac{l_c}{q_n}\right)^4. \tag{5.10}$$

We may now derive the variance of the fluctuation of every point along the contour of the grafted microtubule. By equations 5.5, 5.7 and 5.10 we have

$$\begin{aligned}
\left\langle z^2(s) \right\rangle &= \left\langle \frac{1}{l_c} \sum_i \sum_j a_i a_j W_i\left(\frac{s}{l_c}\right) W_j\left(\frac{s}{l_c}\right) \right\rangle && (5.11)\\
&= \frac{1}{l_c} \sum_i \sum_j \left\langle a_i a_j \right\rangle W_i\left(\frac{s}{l_c}\right) W_j\left(\frac{s}{l_c}\right) && (5.12)\\
&= \frac{1}{l_c} \sum_n \left\langle a_n^2 \right\rangle W_n^2\left(\frac{s}{l_c}\right) && (5.13)\\
&= \frac{1}{l_c} \sum_n \frac{1}{l_p}\left(\frac{l_c}{q_n}\right)^4 W_n^2\left(\frac{s}{l_c}\right). && (5.14)
\end{aligned}$$

Since microtubules are relatively stiff filaments, the deviations $z(s)$ from the x-axis are small, and we may approximate $s \approx x$. Thus

$$\left\langle z^2(x) \right\rangle = \frac{1}{l_c} \sum_n \frac{1}{l_p}\left(\frac{l_c}{q_n}\right)^4 W_n^2\left(\frac{x}{l_c}\right), \tag{5.15}$$

which is the desired relation between the variance of the transversal fluctuations of a grafted microtubule, and the distance from the support.

The variance of the individual mode amplitudes (equation 5.10) is inversely proportional to the mode number q_n to the fourth power. It is therefore often sufficient to truncate the infinite sum in equation 5.15 after several terms and only study the contributions of the first few modes to the total filament fluctuation variance. This will be referred to as the "truncated" expression for the variance of the microtubule's transversal fluctuations. The question now arises whether there are cases when higher order modes must be considered.

It has been shown that the variance of the transversal fluctuations of an arbitrary point along the contour of a grafted microtubule with a free end can also be written in closed form [43, 96, 135]:

$$\left\langle z^2(x)\right\rangle = \frac{x^3}{3l_p}. \tag{5.16}$$

It is interesting to compare this expression to the truncated result (equation 5.15 truncated to several terms). Figure 5.8 shows that equation 5.16 and equation 5.15 truncated to down to two terms agree over a surprisingly long range of the microtubule. As long as a point along the contour sufficiently far ($> 0.4 l_c$) from the support is chosen, its transversal fluctuations are completely dominated by the first two modes. For positions closer to the support, higher order modes must be taken into account. In the present work, thermal noise images were acquired sufficiently far from the support, and microtubular shape

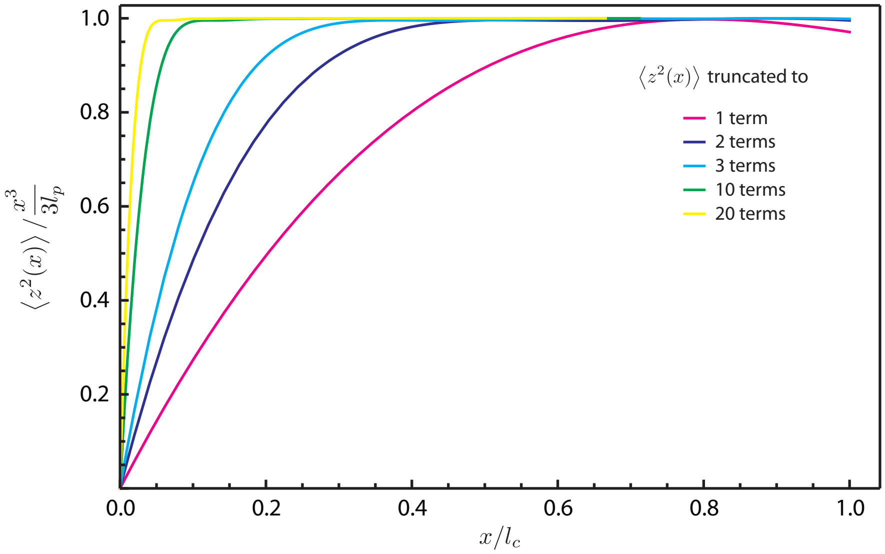

Figure 5.8: Ratio of the truncated expression of $\langle z^2(x)\rangle$ and closed form $\frac{x^3}{3l_p}$ of the variance of the transverse fluctuations along the contour of a grafted microtubule. For positions far from the support, this ratio equals unity, and the two expressions yield equal results.

fluctuations can be considered to be dominated by only the first ∼3 spatial modes to sufficient precision.

5.3.2.2 Interaction between the tracer particle and a fluctuating microtubule: analytical theory

We will now derive an analytical expression for the LRO of an optically trapped particle interacting with a grafted fluctuating microtubule. Since we are using an uncharged and BSA coated tracer particle (section 5.2.4), we shall ignore any electrostatic interaction between the tracer particle and the microtubule and only consider steric interactions, which are complicated by the transversal fluctuations of the filament. The magnitude of the transversal fluctuations changes along the contour of the microtubule (equation 5.16), even over the small extent of a single trapping volume. When measuring the voxel occupancy of one trapping volume, collapsing it along the microtubule into two dimensions and computing its LRO (see figure 5.4) one therefore averages over all magnitudes of transversal fluctuations present along the microtubule in this volume. This effect is small though: For example, consider a microtubule with a persistence length of 2 mm and a trapping volume with depth of 300 nm located on the microtubule 2.2 μm from the support. For this case, the transversal fluctuations change by less than ±5 nm from their mean from the beginning of the volume to its end.

By collapsing the LRO into two dimensions one can therefore reduce the necessary analytical description to a two-dimensional problem perpendicular to the microtubule. The problem can be reduced even further: The transversal fluctuations of the microtubule are radially symmetric. The two dimensional LRO perpendicular to the microtubule is thus expected to have radial symmetry as well. We may therefore reduce the problem to one (radial) dimension (figure 5.9).

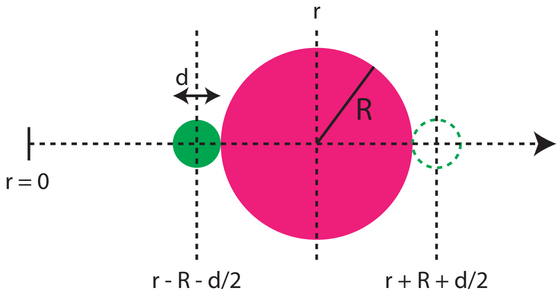

Figure 5.9: Coordinate system for the theoretical treatment of microtubule-tracer particle interaction. The microtubule (green) radially fluctuates away from its equilibrium position at $r = 0$. Due to steric exclusion, it cannot intersect with the tracer particle (pink) located at r. Thus, it cannot enter the region between $r - R - d/2$ and $r + R + d/2$.

We will now begin by deriving the one-dimensional probability density of the trapped particle while it is interacting with the fluctuating microtubule. From this probability density we shall then calculate a one-dimensional expression for the radial LRO.

If no microtubule is present in the trapping volume (i.e. when the trapping volume is empty), the one dimensional probability density of the tracer particle follows from equation 2.21 and is given by

$$p_p(r) = C \exp\left(-\frac{kr^2}{2k_BT}\right) . \tag{5.17}$$

r is the radial displacement of the particle from the focus, k is a radial spring constant describing the trapping potential, and C normalizes the probability density. The optical trapping potential is *not* radially symmetric, and the spring constant k depends on the direction in which the particle is extended from the focus. However, as we will see, this spring constant does not appear in the final form of the derived LRO, and its precise value is therefore of no further consequence.

Every point on the contour of the microtubule performs Gaussian distributed transversal fluctuations with a variance given by equation 5.16,

$$\left\langle z^2(x) \right\rangle = \frac{x^3}{3l_p} = \frac{x^3 k_B T}{3\kappa}. \tag{5.18}$$

This corresponds to the motion of that point in a harmonic potential with an effective spring constant of

$$k_{eff}(x) = \frac{3\kappa}{x^3}. \tag{5.19}$$

The spatial probability density of the point along the microtubule contour is thus

$$p_{MT}(r) = \tilde{C} \exp\left(-\frac{k_{eff} r^2}{2k_B T} \right), \tag{5.20}$$

where $\tilde{C} = \sqrt{\frac{k_{eff}}{2k_B T \pi}}$ normalizes the distribution.

As an approximation we may then express the probability that the microtubule *is* intersecting the particle located at r (figure 5.9) as

$$\int\limits_{r-R-d/2}^{r+R+d/2} p_{MT}(r')\,\mathrm{d}r' = \frac{1}{2}\left[\operatorname{erf}\left(\frac{r+R+d/2}{\sqrt{\frac{2x^3}{3l_p}}}\right) - \operatorname{erf}\left(\frac{r-R-d/2}{\sqrt{\frac{2x^3}{3l_p}}}\right)\right] \quad (5.21)$$

where d is the diameter of the microtubule, R is the radius of the tracer particle, and x is the distance from the support. This approximation ignores all cases in which the microtubule is extended from the focus under a different angle than the particle. In order to include these cases, the probability of intersection between particle and microtubule has to be derived using a two-dimensional approach, which leads to integrals that can not be solved analytically. It was numerically verified that equation 5.21 closely approximates this two-dimensional result. Further, the analytical theory based on the described approximation successfully extracts the microtubule's persistence length from simulated datasets (see below and ref. [71]).

Complementary, the probability that the microtubule *is not* intersecting the particle located at r is

$$1 - \int\limits_{r-R-d/2}^{r+R+d/2} p_{MT}(r')\,\mathrm{d}r' = 1 - \frac{1}{2}\left[\operatorname{erf}\left(\frac{r+R+d/2}{\sqrt{\frac{2x^3}{3l_p}}}\right) - \operatorname{erf}\left(\frac{r-R-d/2}{\sqrt{\frac{2x^3}{3l_p}}}\right)\right]. \quad (5.22)$$

The probability density to find the tracer particle at a certain distance from the center of the trap when scanning around a fluctuating microtubule, $p_{p,MT}$, is equal to the probability density in absence of the filament, p_p, multiplied by the probability that the microtubule *was not* intersecting the particle at that position. Thus

$$p_{p,MT}(r,x) = p_p(r)\left[1-\frac{1}{2}\left[\operatorname{erf}\left(\frac{r+R+d/2}{\sqrt{\frac{2x^3}{3l_p}}}\right)-\operatorname{erf}\left(\frac{r-R-d/2}{\sqrt{\frac{2x^3}{3l_p}}}\right)\right]\right] \tag{5.23}$$

By equation 2.55 the desired expression for the one-dimensional LRO is then

$$\mathrm{LRO}(r) = -\ln\left[1-\frac{1}{2}\left[\operatorname{erf}\left(\frac{r+R+d/2}{\sqrt{\frac{2x^3}{3l_p}}}\right)-\operatorname{erf}\left(\frac{r-R-d/2}{\sqrt{\frac{2x^3}{3l_p}}}\right)\right]\right]+C, \tag{5.24}$$

where C is an arbitrary offset. As we will see in the next section, thermal noise imaging allows us to measure the one-dimensional LRO, which can then be fitted using equation 5.24. The distance from the support x, the particle radius R, and filament diameter d are known, leaving the persistence length l_p and offset C as the only fit parameters. We can therefore extract l_p from the acquired thermal noise images by a fit to the measured LRO. Analyses of simulated datasets verifying the success of this approach can be found in Dr. Martin Kochanczyk's dissertation [71].

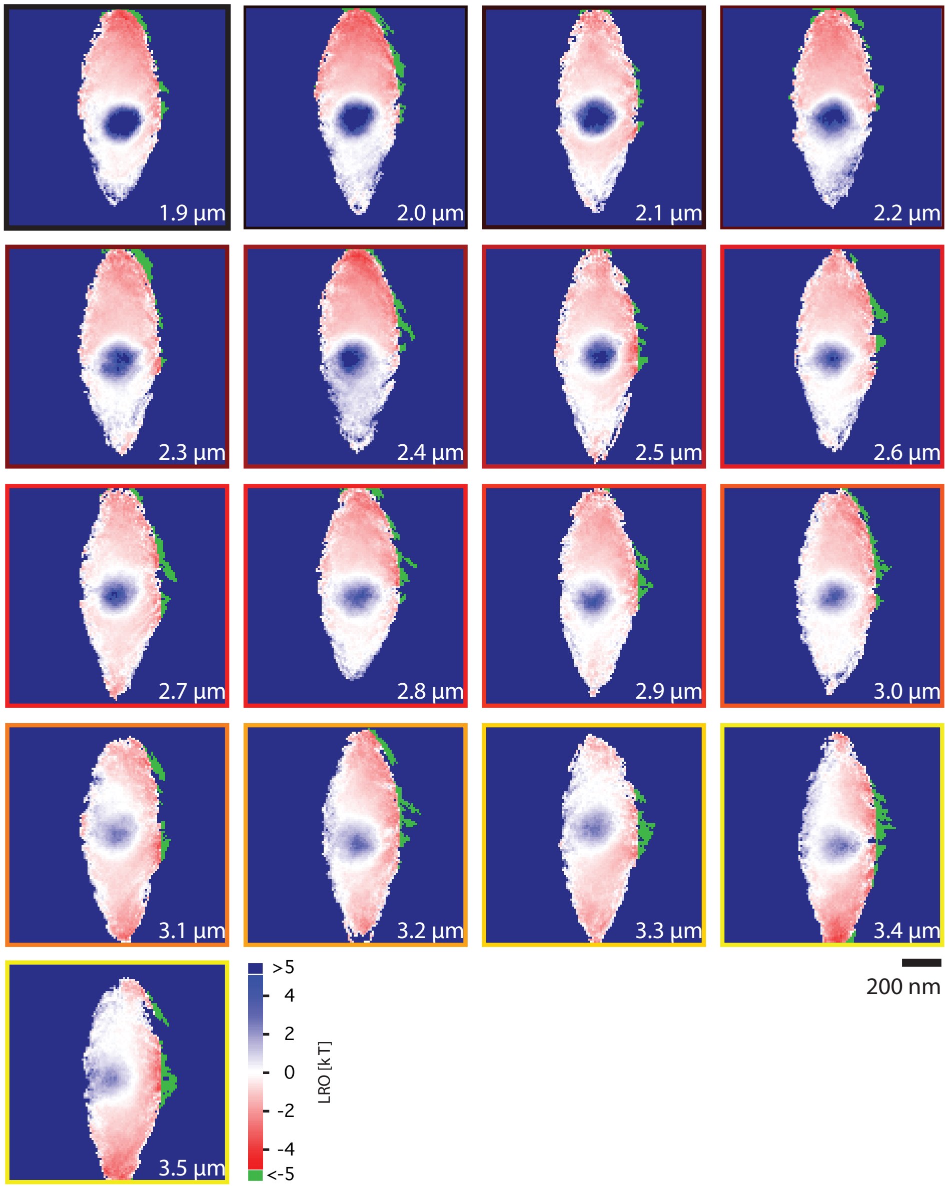

Figure 5.10: Two-dimensional LROs along a grafted microtubule with a free end. The LRO changes with increasing distance from the support (color coded frames of each panel corresponding to arrows in figure 5.5A, and white text in the bottom right of each plot). The further the distance from the support, the shallower the energy barrier experienced by the diffusing particle.

5.3.2.3 Microtubule grafted on one end

As an example consider the same grafted microtubule with a free end of length 7.3 μm which was studied in section 5.3.1.2. We will now analyze it in a more quantitative fashion and extract its persistence length from the acquired data. Figure 5.5A shows the experimental configuration; the arrows indicate the positions along the microtubule at which voxel occupancies were measured. For 17 positions along the contour, separated by 100 nm each, and indicated by colored arrows (black to red to yellow), two-dimensional projections of the LRO were computed and are shown in figure 5.10. Each panel represents a different distance from the support; the frames of the panels are color coded to match the arrows in figure 5.5A. The energy barrier caused by the presence of the microtubule can be seen as a blue disk in each panel. As expected it decreases with increasing distance from the support and thus with increasing transversal fluctuations of the filament.

As discussed in section 5.3.2.2, we'll now make use of the radial symmetry of the LRO and reduce it to one dimension. Starting from the center of the microtubule's energy barrier, the two-dimensional LRO is averaged along concentric circles (figure 5.11A), yielding the one-dimensional LRO which is a function of radial distance from the microtubule's center. These one-dimensional radial LROs are plotted for each distance from the support in figure 5.11B. The color code indicates the distance from the support and again matches the arrows in figure 5.5A. LROs close to the point of grafting (black and brown curves in figure 5.11B) feature a measured infinitely high

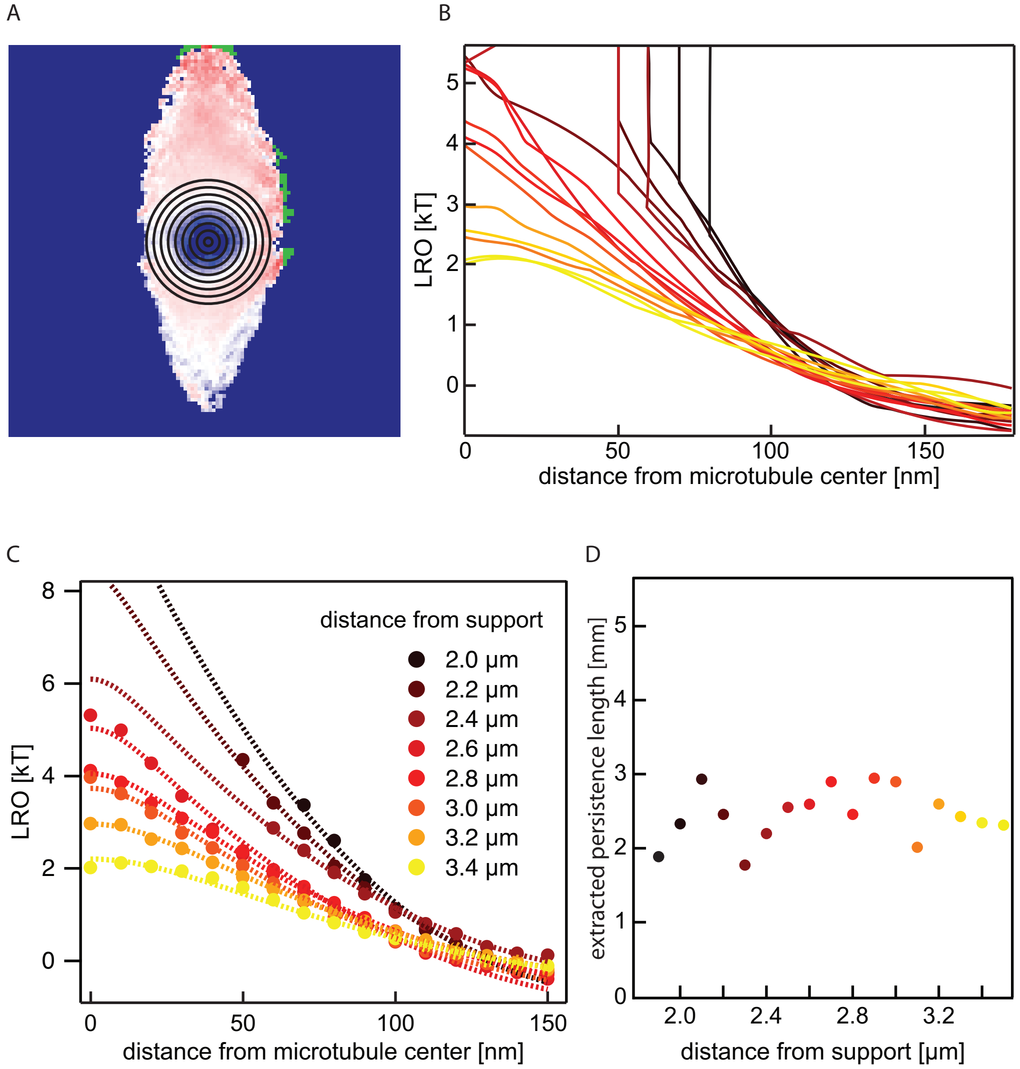

Figure 5.11: Extraction of the persistence length. **A** - Two-dimensional LROs were averaged on concentric circles. The resulting one-dimensional, radial LROs are plotted for all distances from the support (**B**). The color code corresponds to the positions indicated by arrows in figure 5.5A. **C** - Analytical fits (dashed lines) to the one-dimensional LROs (solid markers) yield the persistence length as a fit parameter. Thus, a value for the persistence length can be independently extracted from each two-dimensional LRO along the support (**D**).

energy barrier, stretching from the microtubule's center ($r = 0$) to a distance between $r = 50$ nm and $r = 100$ nm. An infinitely high energy barrier means that voxels within this distance from the center of the microtubule were never visited by the particle during the 4 second long observation time since the microtubule's transversal fluctuations were too small to vacate them. These voxels make up the "excluded" part of the trapping volume.

It is evident that LRO measurements further from the support (red and yellow curves in figure 5.11B) do not feature any excluded volume: There are no voxels with an infinitely high interaction energy barrier, and the particle could access all voxels, implying that they were at times vacated by the microtubule due to its larger transversal fluctuations. However, a high interaction energy of several k_BT is still clearly measurable, which can be used to quantify these transverse fluctuations. The further the measurement is from the support, the larger the transverse fluctuations, and the smaller the effective interaction energy gets, as expected.

In order to extract the microtubule's persistence length from the data, each one-dimensional LRO along the microtubule is fit with the analytical expression given by equation 5.24 (figure 5.11C). Several parameters are held constant during the fit: the particle radius R, and filament diameter $d = 25$ nm are known, and the distance from the support x is measured by analyzing the fluorescence contrast images. This leaves only the persistence length and an additive offset as free parameters for the fit. Extracted persistence lengths for each voxel occupancy (and thus two-dimensional LRO) measurement along the grafted microtubule with contour length 7.3 μm are shown in figure 5.11D. The data are scattered around a persistence length of (2.4$\pm$0.3) mm; the given error is the standard deviation of the scatter around the mean. The precision of the mean is discussed in section 5.3.2.5.

Inserting the extracted persistence length into equation 5.16, we may conclude that the microtubule's transversal fluctuations increased from a standard deviation of 22 nm at the beginning of the scan to 77 nm at the end of the 2 μm long scan.

Persistence length of short microtubules The method outlined above was applied to measure the persistence length of short microtubules ($l_c < 4\,\mu$m), a length regime that has been inaccessible to established techniques. Voxel occupancies were acquired along 15 microtubules, ranging in contour length from 600 nm to 7.7 μm. The persistence length of each microtubule was extracted from the one-dimensional LROs along its contour, as demonstrated above.

The persistence length increases with increasing contour length over several orders of magnitude (figure 5.12), from $l_p = 25\,\mu$m for the shortest measured microtubule, to 2.4 mm for the longest. The data for microtubules with long contour length ($l_c > 4\,\mu$m) is comparable to previous measurements [96, 135], validating the present method. Interestingly, for short microtubules ($l_c < 2\,\mu$m) l_p drops rapidly, indicating novel, previously inaccessible behavior in this length regime. It appears that short microtubule with a contour

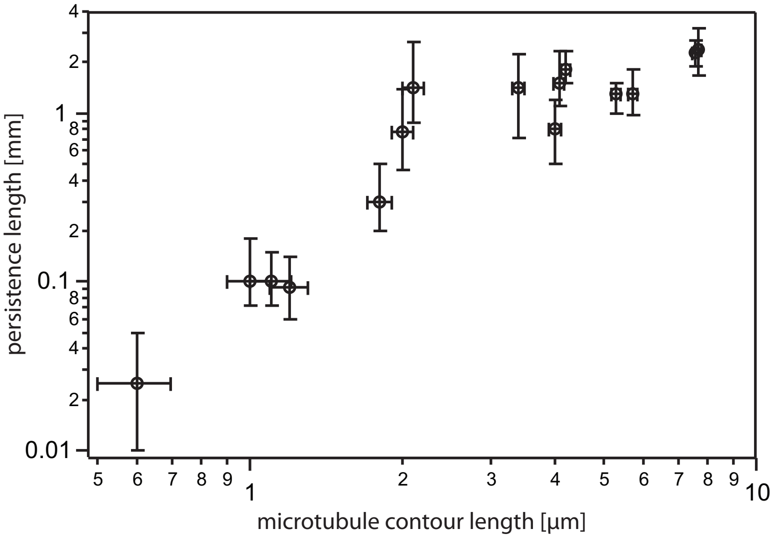

Figure 5.12: Microtubule persistence length as a function of contour length for short microtubules. Thermal noise imaging reveals that the persistence length of a microtubule drops strongly for small ($l_c < 2\,\mu$m) microtubules.

length of approximately $l_c = 1\,\mu$m are very flexible ($l_p \leq 0.1$ mm); however their persistence length seems to increase by an order of magnitude once their contour length doubles to $l_c = 2\,\mu$m. This supports the hypothesis outlined in the introduction: short microtubules might be be flexible in order to avoid obstacles during polymerization, while long microtubules might be stiff in order to fulfill their biological function.

We have so far seen that the rather large transversal fluctuations of a microtubule with a free end can be quantified by thermal noise imaging. The next section demonstrates that small changes in transversal fluctuations can also be easily resolved.

5.3.2.4 Microtubule grafted on both ends

Consider the same microtubule imaged in section 5.3.1.1, which was grafted on both ends to the holey carbon film support. Due to its boundary conditions we expect it to be completely immobilized close to the points of grafting, but able to fluctuate in between. Similar to a biofilament in a network, the magnitude of these transversal fluctuations depends on the tension of the filament, which in the present assay is random, as it depends on the microtubule's random conformation, and thus its random momentary tension, while it was binding to the support. One-dimensional LROs were computed from the voxel occupancies discussed in section 5.3.1.1, for different positions 200 nm apart, starting at a distance of 4.5 μm from the support (arrows in figure 5.13A). The color code of the arrows matches the colors of the LRO curves in figure 5.13B. The tracer particle felt an infinitely high energy barrier at almost all measured distances from the support, in stark contrast to the microtubule with a free end discussed in section 5.3.2.3. The closer the measured position is to the support (black curves), the larger the excluded volume. When stepping further away from the grafting point, the excluded volume gets smaller (red and yellow curves), indicating an increase in the microtubule's transversal fluctuations, as one would expect. Finally, at the second to last measured position, the excluded volume vanishes completely, and the particle could explore the entire trapping volume, albeit with a large energy barrier of approximately $6\,k_BT$ in magnitude. The last measured position along the microtubule again features an infinite energy barrier and thus

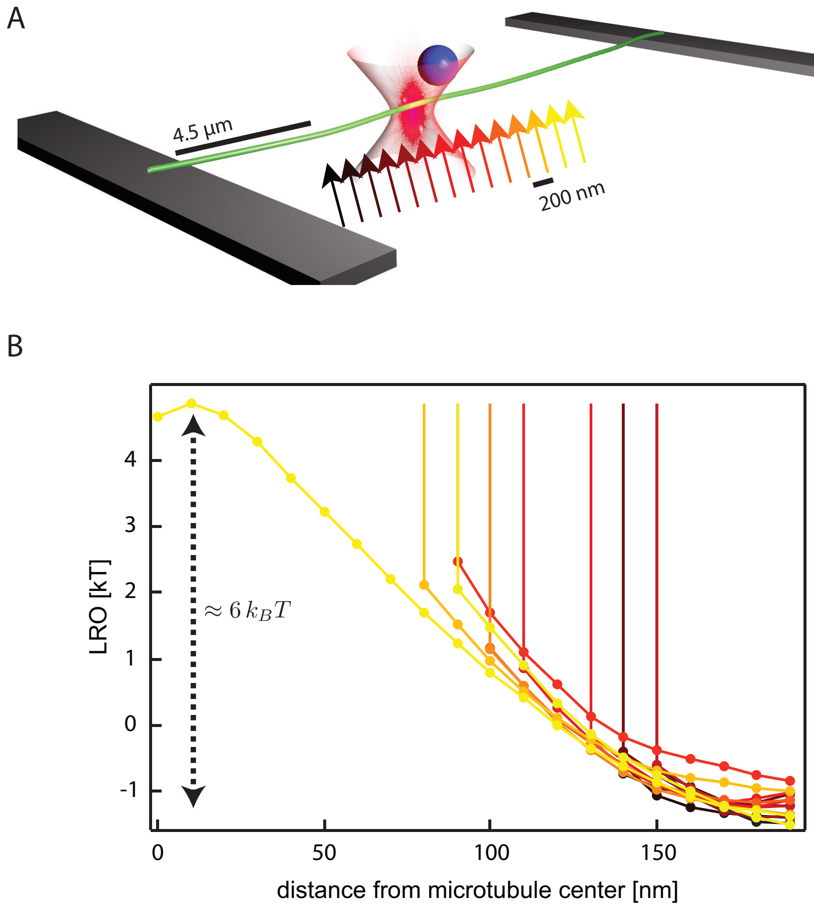

Figure 5.13: LROs along a microtubule grafted on both ends. **A** - The microtubule was grafted on both ends. Voxel occupancies were acquired with a spacing of 200 nm, starting 4.5 μm from the support. **B** - One-dimensional LROs computed for the positions marked in **A**. The excluded volume defined by the position of the infinite energy barrier decreases with increasing distance from the support, indicating an increase in the transversal fluctuations of the microtubule.

an excluded volume, which may indicate that the particle was scanned over the most flexible position along the microtubule, and the transversal fluctuations start to get smaller again towards the end of the scanned range.

It was thus demonstrated that thermal noise imaging can not only quantify the fairly large transversal fluctuations of grafted microtubules with free ends, but also of microtubules confined on both ends, which more closely mimic the behavior in a biopolymer network.

5.3.2.5 Discussion of errors

The precision of the presented measurements is discussed in this section. Both the radius of the tracer particle R, and the distance from the grafting point x must be known precisely in order to extract the persistence length l_p by fitting equation 5.24 to the acquired datasets. The uncertainty in R and x dominate the error in the analytical fit, and thus the error of the measurement of l_p.

Uncertainty in the particle radius R. The manufacturer of the tracer particles specifies a diameter of (190 ± 29) nm (mean ± standard deviation of the ensemble). However, measurement of the hydrodynamic diameter of 20 particles as described in section 4.2.6 yielded 187 ± 10 nm; i.e. the measured spread in diameter was significantly smaller than specified by the manufacturer.

The hydrodynamic radius does not necessarily reflect the effective radius for thermal noise imaging though: The tracer particles are made from polystyrene; i.e. they are polymer “balls” which may have a considerable amount of polystyrene “hairs” sticking out of their surface. This corona of hairs can be as thick as 7 nm [122]. As a result, the precise diameter of a polystyrene particle is an ill defined quantity. Further, for the derivation of the analytical theory of microtubule-probe interaction, we assumed a steric interaction between microtubule and probe. This is, of course, not entirely correct: negatively charged residues on the microtubules (“E-hooks”) extend up to 3.5 nm from the microtubule’s surface [105, 106] and electrostatically interact with charged residues on the BSA layer around each bead.

All these effects were accounted for by setting the radius in equation 5.24 to an effective radius of $R = (125 \pm 15)$ nm. This estimate was verified by analyzing the excluded volumes (i.e. the volumes in which the LRO is infinitely high) in thermal noise images of microtubules grafted on both ends, acquired close to the points of grafting. The transversal fluctuations of the microtubules are expected to be negligible in this case, and the effective particle radius can be extracted from the excluded volume by equation 2.47. All such control experiments yielded particle radii in the estimated range when assuming a radius of $R_F = 12.5$ nm for the microtubule.

Uncertainty in the distance from the support x. The distance x of the trapping volume from the microtubule’s point of grafting was determined by fluorescence microscopy. Due to the diffraction limit, it was estimated that x

could be extracted to a precision of ±100 nm.

Resulting uncertainty of the measured persistence length l_p. In order to determine the error of the extracted persistence length, the one-dimensional LROs were fitted with all permutations of $R \pm 15$ nm and $x \pm 100$ nm, yielding a set of four values for l_p. The largest of these values was used as the persistence length's upper bound, and the smallest as its lowest bound. This in general lead to an asymmetric error around the mean of l_p, as indicated by the error bars in figure 5.12.

5.4 Conclusions

In this chapter, thermal noise imaging was established as a quantitative tool to simultaneously image biofilaments and quantify their transversal fluctuations. The tracer particle's voxel occupancy can be displayed as a thermal noise image, or used to compute the LRO which is equal to the effective interaction energy between the imaged filament and the tracer particle.

Microtubules grafted on one or both ends were chosen as a model system to demonstrate the power of this novel technique. An analytical theory was developed to relate the LRO to the transversal fluctuations of the imaged microtubule, allowing the extraction of the microtubule's persistence length. Using this method, the persistence lengths of very short microtubules were measured, and a surprising new regime of dependence on contour length uncovered: Microtubules below 2 μm in length show a dramatic decrease in persistence length, and thus a dramatic increase in flexibility, supporting the hypothesis that short microtubules during polymerization can avoid obstacles and find binding partners due to their comparably large transversal fluctuations. Finally, it was demonstrated that the transversal fluctuations of a microtubule confined on both ends can be quantified from its thermal noise images, paving the way for the measurement of transversal fluctuations inside a biopolymer network for the first time (chapter 6).

Chapter 6

Thermal noise imaging of collagen networks

Having demonstrated that thermal noise imaging can visualize individual biopolymers (see chapter 5), we will now focus on imaging biopolymer networks. This chapter shows that thermal noise imaging can characterize the local submicroscopic architecture of collagen networks, and can elucidate mechanical properties of individual collagen fibrils *in situ*.

6.1 Introduction

Collagen (see section 1.2) is the most abundant protein in animal tissues [25], where it forms a major component of the extracellular matrix. Its mechanical properties have an impact on many biological processes: The speed at which motile cancer cells invade collagen networks depends on the density of the networks [68]. Cancer cells can locally densify and align the network around them [142], which affects the motion of other cells in their vicinity, possibly enhancing network invasion [145]. Pairs of endothelial cells growing in a collagen network mechanically sense each other and form cell-cell contacts, provided that the network is compliant enough [108]. Further, the stiffness of the matrix influences the fate of cells, for example, depending on its mechanical properties, cell differentiation or apoptosis can be induced [62].

Collagen fibrils have a bending modulus on the order of 0.1 GPa [158], resulting in a persistence length of ∼2 m, which makes them much stiffer than microtubules (see chapter 5). We therefore expect that they can be treated to first approximation as stiff rods. This will be confirmed in this chapter by verifying that, unlike fluctuating microtubules (section 5.3.2), their thermal noise images show no transversal fluctuations.

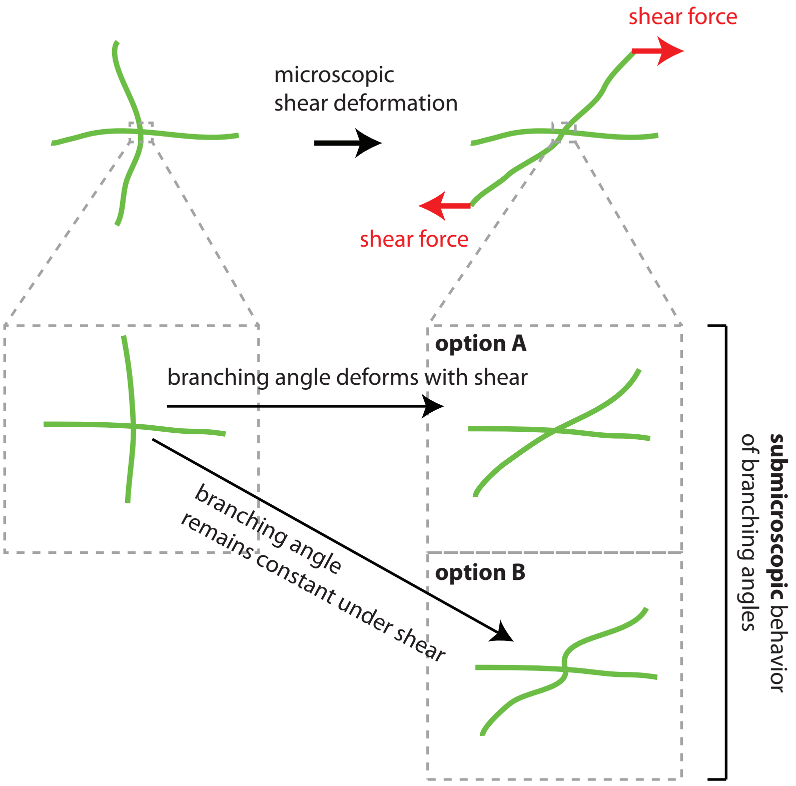

Figure 6.1: Submicroscopic behavior of junctions in collagen networks under shear. Under an applied shear force, two intersecting fibrils may either slide against each other (**A**), or their branching angle may be fixed (**B**).

Locally or globally applied loads thus likely result in deformation and displacement of junctions in addition to bending and stretching of filaments. However, the submicroscopic behavior of the junctions has been inaccessible to established experimental methods (see section 1.3.4)[1], and is not understood [142], despite the fact that it is essential to the understanding of mechanical signal transduction through the network. For example, two collagen fibrils at a junction may either be interacting sterically, and slide against each other under the application of a load, or the angle at which they intersect may be fixed (figure 6.1). The behavior of branching angles under network shear is an important parameter in theoretical models of biopolymer networks. For example, a recent numerical model of collagen networks [78] assumes that the fibrils are coupled in all degrees of freedom at the junctions, i.e. that the branching angles are fixed. This, though, appears unlikely given the observed plasticity of such networks under large strains [142].

In this chapter we will see how thermal noise imaging can be implemented to visualize junctions in collagen networks for the first time under physiological conditions with super resolution, paving the way for the study of their behavior under applied loads. Further, the LROs of the acquired voxel occupancies verify that the observed collagen fibrils did not measurably fluctuate transversally and can indeed be approximated as stiff rods. Additionally,

---

[1] It might be possible to acquire a super resolution image of a collagen network using the concurrently emerging technique of 3D STORM, given that the transversal fluctuations of the individual fibrils are negligible as shown in this work. However, STORM requires the network to be fluorescently labeled, which could change its structure. Currently no 3D STORM data of collagen networks exists.

it will be shown how fibril diameters can be extracted from the acquired data.

6.2 Materials and Methods

6.2.1 Preparation of collagen networks

Collagen gels were polymerized following a procedure established by Professor Dr. Ben Fabry's laboratory at the University of Erlangen-Nuremberg [84]. Acid-soluble rat-tail tendon collagen (type I, Collagen R, 354236, BD Biosciences, NJ, USA) and bovine-dermis collagen (type I, Collagen G, 354231, BD Biosciences, NJ, USA) were mixed at relative concentrations of 1:2. The mixture was then diluted to a total collagen concentration of 2.4 mg/ml by adding equal parts of 10x DMEM (D2429, Sigma Aldrich, MO, USA) and 0.27 M $NaHCO_3$.[2] To induce gel polymerization, the pH of the solution was raised to pH 10 using 1 M NaOH. If desirable, the collagen concentration can then be reduced by adding a diluter solution consisting of one part 10x DMEM, one part 0.27 M $NaHCO_3$ and 8 parts deionized water, adjusted to pH 10 using 1 M NaOH. All components were kept on ice during mixing.[3]

$30\,\mu$l of the mixture were then quickly pipetted into a preassembled sample chamber consisting of a glass coverslip and a metal spacer, and left to polymerize for >45 min at 37 °C in a 5% CO_2 atmosphere. Polymerizing the

---

[2] Fibrils can be polymerized from pure collagen R or collagen G solutions, and DMEM and $NaHCO_3$ are not essential for fibril formation either. However, the described protocol has become a standard in three-dimensional cell culture and was chosen for its biological relevance.

[3] The adjustment of the pH thus occurred in the cold, which is one of two possible polymerization pathways with different intermediate aggregates (see section 1.2).

network inside the sample chamber ensures its attachment to the coverslip, which is a prerequisite for a mechanically stable assay. After polymerization, the gel was gently rinsed with 1 ml of 1x phosphate buffered saline (PBS). Care was taken to never let the gel dry out.

For these polymerization conditions, the formed gel is largely made up of collagen fibrils rather than collagen fibers, i.e. most collagen fibrils in the network do not bundle to fibers.[4]

6.2.2 Tracer particle preparation

The same fluorescent polystyrene beads with a measured diameter of (187 ± 10) nm (mean ± standard deviation see section 5.3.2.5) were used as in section 5.2.4. However, coating the beads with BSA did not prevent their adhesion to collagen fibrils. Instead, the particles were coated with poloxamer 407 (16758, Sigma Aldrich, MO, USA), a block co-polymer consisting of a central hydrophobic block of polypropylene glycol (PPG, 67 repeat units), flanked on each side by a hydrophilic polyethylene glycol block (PEG, 98 repeat units) [86].

Tracer particles were incubated at room temperature at least overnight in a solution of 2 mg/ml poloxamer 407 in PBS. From this stock solution the particles were further diluted into PBS for each experiment.

Poloxamer 407 self assembles as a brush on the surface of the polysty-

---

[4] Personal communication with Janina Lange.

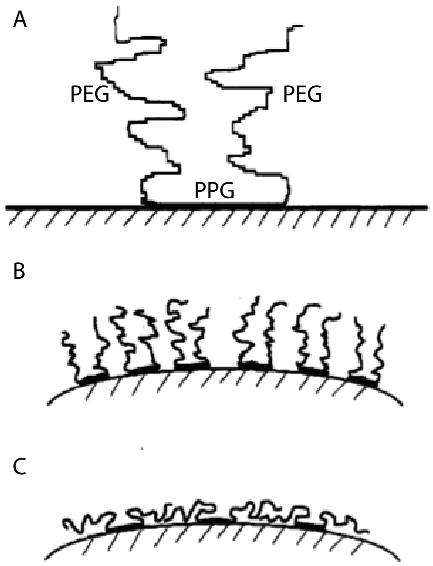

Figure 6.2: Self-assembly of a poloxamer on polystyrene beads. **A** - The hydrophobic PPG block binds to the polystyrene bead, while the hydrophilic PEG blocks form a brush pointing outward. The thickness of the brush formed by the PEG blocks depends on the density of adhesion of the poloxamer to the bead (**B** and **C**). This adhesion density is determined by both the radius of the bead and the length of the PPG block (data not shown). Adapted with permission from [77]. Copyright 1994 American Chemical Society.

rene beads [77, 86], with the hydrophobic PPG block attaching to the particle, while the hydrophilic PEG blocks form coils pointing radially outwards (figure 6.2). The thickness of the brush formed by the PEG blocks depends on the density of adhesion of the poloxamer to the bead (figure 6.2B and C), which is determined by both the radius of the bead and the length of the PPG block [77]. This thickness has been measured for several different poloxamer-bead combinations, but not for poloxamer 407. When assembled onto a 190 nm diameter bead, the thickness of the formed brush can however be extrapolated from the available data to be on the order of 10 nm [77]. Taking into account the particle's size distribution, the uncertainty caused by the poloxamer brush, and allowing for a small corona of polystyrene hairs on each particle's surface (see section 5.3.2.5), we will assume an effective particle radius of (105 ± 15) nm.

6.2.3 High bandwidth and high precision optical trapping

The Thermal Noise Imaging PFM described in section 2.5 was used for the experiments described in this chapter. This PFM has a bandwidth of 1 MHz and position detection precision of 1 nm laterally and 7 nm along the optical axis for tracer particles with 200 nm diameter. Before each data acquisition the PFM was calibrated *in situ* as discussed in section 2.3.2. Typical spring constants of the potential confining the tracer particle were $k_x = 1.5\,\mathrm{pN}/\mu\mathrm{m}$, $k_y = 1.0\,\mathrm{pN}/\mu\mathrm{m}$ and $k_z = 0.15\,\mathrm{pN}/\mu\mathrm{m}$. The corresponding autocorrelation times of the tracer particle's diffusion were $\tau_x = 1.1$ ms, $\tau_y = 1.7$ ms, and

$\tau_z = 11$ ms.

For all experiments described in this chapter, detector signals were sampled at 100 kHz with a full electronics bandwidth of 1 MHz.

6.2.4 Experimental assay

After polymerization (section 6.2.1), the sample chamber was closed by a top coverslip (figure 6.3A). Tracer particles in PBS (section 6.2.2) were flushed into the chamber through channels in the metal spacer. The laminar flow of this flush is located predominantly above the collagen gel, resulting in the tracer particles being deposited above, and not inside the collagen network. The sample was then incubated for >2 hours to allow the tracer particles to diffuse deep into the gel. At this point the sample chamber can be mounted on the PFM. Tracer particles can be viewed using fluorescence microscopy, and the gel produces a small but visible bright field contrast (figure 6.3B). After optically trapping one of the tracer particles thermal noise images (see section 2.4) can be acquired.

The network extends deep into the sample chamber, and it is tempting to try to image far away from the bottom coverslip. It is important to keep in mind that the light distribution close to the focus, and therefore the fidelity of the optical trapping potential and of the position detection decreases with increasing distance from the bottom coverslip due aberrations introduced by transmission through the collagen network. A distance from the bottom coverslip of up to $30\,\mu$m was empirically found to be suitable for thermal noise

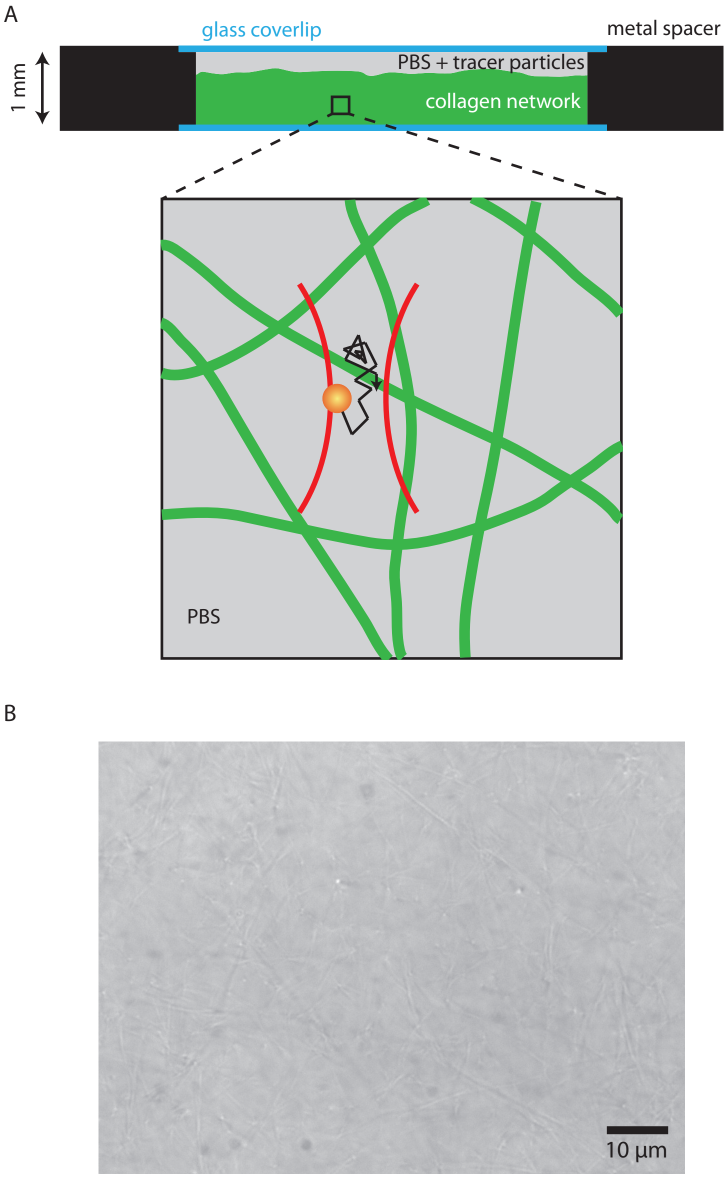

Figure 6.3: Collagen gel assay. **A** - A collagen network is polymerized inside a sample chamber, after which tracer particles in PBS are added. Tracer particles (orange) in the network (green) can be optically trapped (red beam) and thermal noise images can be acquired. **B** - Brightfield image of a collagen network acquired with the PFM.

imaging experiments inside collagen networks.

6.3 Results and Discussion

6.3.1 Thermal noise imaging

In comparison to the single filament assay discussed in chapter 5, thermal noise imaging inside a collagen network poses two additional challenges, and we will discuss here how they can be overcome. Firstly, collagen fibrils are much thicker than microtubules, and forward scatter a significant portion of the trapping and tracking beam onto the detector, leading to artifacts in the position signal. This effect must be corrected for to accurately measure the position of the tracer particle. Secondly, the total acquisition time for large combined thermal noise images must be reduced. In order to acquire meaningful images of local network architecture at the very least the volume around a junction has to be imaged, which is on the order of $1\,\mu\text{m}^3$ as we will see. It was demonstrated in chapter 5 that such large images can be constructed by adding up individual partially overlapping voxel occupancies, which yields the cumulative voxel occupancy of the scan (section 5.3.1.1). The width of individual trapping volumes was ~300 nm laterally and ~900 nm axially, as in chapter 5. To ensure sufficient overlap, individual voxel occupancies were measured at positions spaced 100 nm laterally and 300 nm axially (see figure 6.4A for a two-dimensional sketch). For example, a volume of approximately $1\,\mu$m x 1μm x $1\,\mu$m can be imaged by acquiring an individual voxel occupancy measurement at each grid point on a 10 x 10 x 2 (x x y x z) grid (red dots in

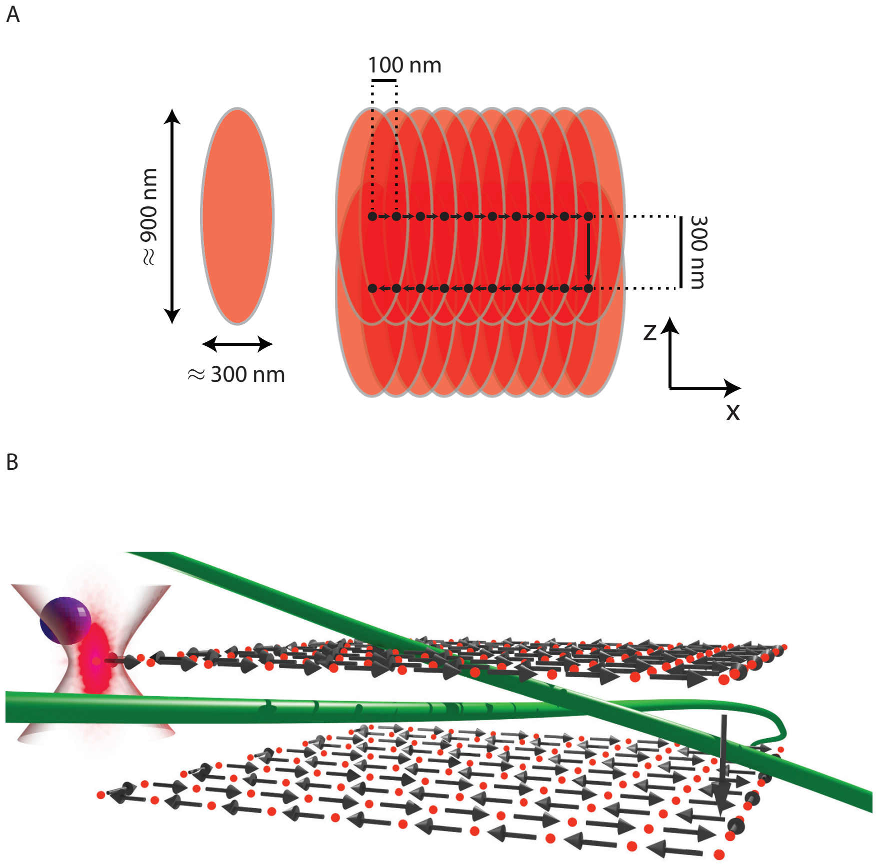

Figure 6.4: Raster scan through a biopolymer network. **A** - Voxel occupancies are acquired centered around positions spaced by 100 nm laterally and 300 nm axially. **B** - 10 x 10 x 2 (x x y x z) grid (red dots) spaced 100 nm laterally and 300 nm axially. The arrows indicate the direction in which the trapping volume is moved between voxel occupancy measurements. Two collagen fibrils (green) are drawn into the figure to indicate that this is, indeed, a scan through a network.

figure 6.4B). With an integration time of 4 s for each individual voxel occupancy, this scan takes 13.3 minutes – a very long time, even considering the instrument's exceptionally small long timescale drift of 10 nm/min. Scanning a 2 μm x 2μm x 2 μm volume (which approximately corresponds to a 20 x 20 x 5 grid) takes over two hours, a time scale over which the instrument cannot be expected to be stable even under the most opportune circumstances. Therefore, a different scanning strategy must be implemented to reduce this total acquisition time.

6.3.1.1 Correction of the position signal for network scattered contributions

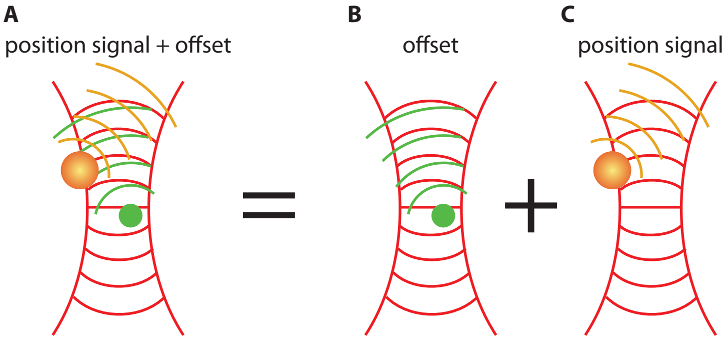

Figure 6.5: Correcting the position signal for network scattered contributions. To first order approximation, the intensity striking the detector (**A**) may be approximated as the sum of the signal caused by the network alone (**B**), plus the position signal of the particle in absence of the network (**C**). **A** is acquired by reading out the detector while the particle is trapped. **B** can be independently measured after releasing the particle from the trap. The actual position signal (**C**) can then be computed.

Recall that in absence of the collagen network the position of the optically trapped tracer particle is determined by reading out the intensity of the interference of the light forward scattered by the particle (orange wavefronts in figure 6.5) with the light of the trapping beam (red wavefronts) on the PFM's quadrant photodiode (QPD, see section 2.3.1). This can be mathematically described as the interference of the scattered electric field $\boldsymbol{E}_p(\boldsymbol{b}_p)$ with the electric field of the incoming beam $\boldsymbol{E}_{in}$ [113]. The scattered electric field depends on the particle's position relative to the focus, $\boldsymbol{b}_p$ (see figure 6.6), while the incident electric field is particle position independent. The intensity striking a certain area element on the QPD is equal[5] to the square of the sum of the electric fields at that location

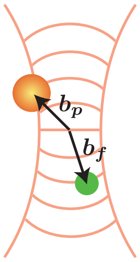

Figure 6.6: Definition of particle and fibril position vectors.

$$
\begin{aligned}
I_{position}(\boldsymbol{b}_p) &= \left|\boldsymbol{E}_p(\boldsymbol{b}_p) + \boldsymbol{E}_{in}\right|^2 && (6.1)\\
&= \left|\boldsymbol{E}_p(\boldsymbol{b}_p)\right|^2 + \left|\boldsymbol{E}_{in}\right|^2 + 2\left\langle \boldsymbol{E}_p(\boldsymbol{b}_p), \boldsymbol{E}_{in}\right\rangle, && (6.2)
\end{aligned}
$$

where the dependence of each term on the location on the QPD is not explicitly shown to improve readability. This intensity distribution is integrated over the area of each of the four quadrants to arrive at the detector responses S_i,

---

[5] up to a multiplicative constant, see equation 2.6. We may neglect this constant here since the scaling between detector response and particle position is determined by the detector calibration *in situ*.

($i = I, II, III, IV$), which are related to the particle's position signal (see section 2.3.1). The intensity of the incoming beam $|\boldsymbol{E}_{in}|^2$ does not depend on the tracer particle's position and contributes a constant offset to the voltage output of all four quadrants, and thus does not contribute to the position signal. It therefore can be set to zero (or any other constant) for the following discussion, and the detector response is thus given by the following intensity distribution on the QPD

$$I_{position}(\boldsymbol{b}_p) = |\boldsymbol{E}_p(\boldsymbol{b}_p)|^2 + 2\,\langle \boldsymbol{E}_p(\boldsymbol{b}_p), \boldsymbol{E}_{in}\rangle\,. \tag{6.3}$$

Consider now a collagen fibril close to the focus of the laser beam. The fibril will forward scatter light of the trapping beam, described by the electric field $\boldsymbol{E}_{fibril}(\boldsymbol{b}_f)$, which depends on the fibril's position relative to the focus, $\boldsymbol{b}_f$ (see figure 6.6). This forward scattered light will be projected onto the QPD. In absence of the tracer particle (figure 6.5B) the intensity distribution on the detector is thus given in complete analogy to the arguments above as

$$I_{fibril}(\boldsymbol{b}_f) = |\boldsymbol{E}_{fibril}(\boldsymbol{b}_f)|^2 + 2\,\langle \boldsymbol{E}_{fibril}(\boldsymbol{b}_f), \boldsymbol{E}_{in}\rangle\,. \tag{6.4}$$

Let's now consider both the particle and the fibril being close to the laser beam's focus, as is the case during thermal noise imaging. The intensity at a given area element of the QPD is now [123]

$$
\begin{aligned}
I_{total}(\boldsymbol{b}_p, \boldsymbol{b}_f) = & \; |\boldsymbol{E}_p(\boldsymbol{b}_p) + \boldsymbol{E}_{in} + \boldsymbol{E}_{fibril}(\boldsymbol{b}_f)|^2 \\
= & \; |\boldsymbol{E}_p(\boldsymbol{b}_p)|^2 + |\boldsymbol{E}_{fibril}(\boldsymbol{b}_f)|^2 \\
& + 2 \langle \boldsymbol{E}_p(\boldsymbol{b}_p), \boldsymbol{E}_{in} \rangle \\
& + 2 \langle \boldsymbol{E}_{in}, \boldsymbol{E}_{fibril}(\boldsymbol{b}_f) \rangle \\
& + 2 \langle \boldsymbol{E}_{fibril}(\boldsymbol{b}_f), \boldsymbol{E}_p(\boldsymbol{b}_p) \rangle \, ,
\end{aligned}
\tag{6.5}
$$

where again $|\boldsymbol{E}_{in}|^2$ has been set to zero. We will assume that the amount of light scattered by the particle and by the fibril is small. Thus, to first order approximation, we may neglect the term $2 \langle \boldsymbol{E}_{fibril}, \boldsymbol{E}_p \rangle$ and write

$$
\begin{aligned}
I_{total}(\boldsymbol{b}_p, \boldsymbol{b}_f) = & \; |\boldsymbol{E}_p(\boldsymbol{b}_p)|^2 + 2 \langle \boldsymbol{E}_p(\boldsymbol{b}_p), \boldsymbol{E}_{in} \rangle \\
& + |\boldsymbol{E}_{fibril}(\boldsymbol{b}_f)|^2 + 2 \langle \boldsymbol{E}_{in}, \boldsymbol{E}_{fibril}(\boldsymbol{b}_f) \rangle \\
= & \; I_{position}(\boldsymbol{b}_p) + I_{fibril}(\boldsymbol{b}_f).
\end{aligned}
\tag{6.6}
$$

This relation is graphically illustrated in figure 6.5.

During each individual voxel occupancy measurement the fibril's position with respect to the focus is assumed to be fixed[6], and the total intensity distribution on the detector is given by the signal caused by the particle's motion, $I_{position}(\boldsymbol{b}_p)$, plus an additional constant offset determined by the position

---

[6] This approximation is valid for collagen networks, since we may assume that the transversal fluctuations of each fibril will be small due to collagen's large persistence length of several meters. More flexible filaments, such as actin, are typically much thinner than collagen fibrils and likely scatter much less light. Thus, when measuring in networks made from flexible filaments the correction outlined in this section is likely not necessary, since the light scattered by the tracer particle is orders of magnitude larger than the light scattered by individual filaments in the network.

of the fibril, $I_{fibril}(\boldsymbol{b}_f)$. Integrating equation 6.6 over the four quadrants of the detector yields for the total signal on the detector (see section 2.3.1 and [123])

$$S_{\alpha,total}(\boldsymbol{b}_p, \boldsymbol{b}_f) = S_{\alpha,position}(\boldsymbol{b}_p) + S_{\alpha,fibril}(\boldsymbol{b}_f), \tag{6.7}$$

and thus, for the detector response that reflects only the motion of the particle,

$$S_{\alpha,position}(\boldsymbol{b}_p) = S_{\alpha,total}(\boldsymbol{b}_p, \boldsymbol{b}_f) - S_{\alpha,fibril}(\boldsymbol{b}_f), \tag{6.8}$$

where $\alpha = x, y, z$. It is this $S_{\alpha,position}(\boldsymbol{b}_p)$ that must be determined to precisely measure the tracer particle's position. Therefore, in order to extract the position time trace of the diffusing particle, two measurements are necessary: For each voxel occupancy measurement at a certain location in the sample, the time traces of the signals $S_{\alpha,total}(\boldsymbol{b}_p, \boldsymbol{b}_f)$ of the particle's motion in the presence of a fibril are recorded. Subsequently, the particle is released from the optical trap, and the constant offsets $S_{\alpha,fibril}(\boldsymbol{b}_f)$ caused by the fibril are measured at the same location in the sample. The detector's response due to the particle's motion, $S_{\alpha,position}(\boldsymbol{b}_p)$, can then be computed by equation 6.8. Calibration of this response (see section 2.3.2) then yields the particle's position time trace.

Having demonstrated how the particle's position time trace can be measured even if additional light is scattered by the network, we will now turn our attention to improving the total acquisition time by implementing a smart scanning strategy.

6.3.1.2 Raster scans with feedback

Consider acquiring voxel occupancy measurements centered around positions on a grid, as shown in figure 6.7A. A two-dimensional grid is drawn for clarity, but the approach outlined in the following applies to three dimensional grids as well. It is evident from the sketch that at most grid positions the trapped tracer particle does not interact with the network while exploring its trapping volume. Acquisition of voxel occupancies at these positions leads to thermal noise images of “empty space” which provide no information about the network. If voxel occupancies are only measured at positions that are close to the network’s filaments (red grid positions in figure 6.7A), the network architecture is fully imaged, but the total acquisition time is dramatically reduced.

Positions close to filaments were found by an initial rapid raster scan of the trapped particle through the grid, during which 100 ms long time traces of $S_{\alpha,total}$, $\alpha = x, y, z$, were acquired at each position. Using the detector’s sensitivity (see section 2.3.2), this signal can be related to the tracer’s position (albeit not corrected for nonlinearities in the detector response), plus an unknown position offset since the detector has not yet been corrected for the signal offsets introduced by the light scattered by the network (see section 6.3.1.1). These 100 ms long time traces are not long enough to compute meaningful voxel occupancies: The autocorrelation time along the optical axis is ∼17 ms, implying that the time traces contain only ∼6 independent position measurements for the particle’s axial motion. However, they are long

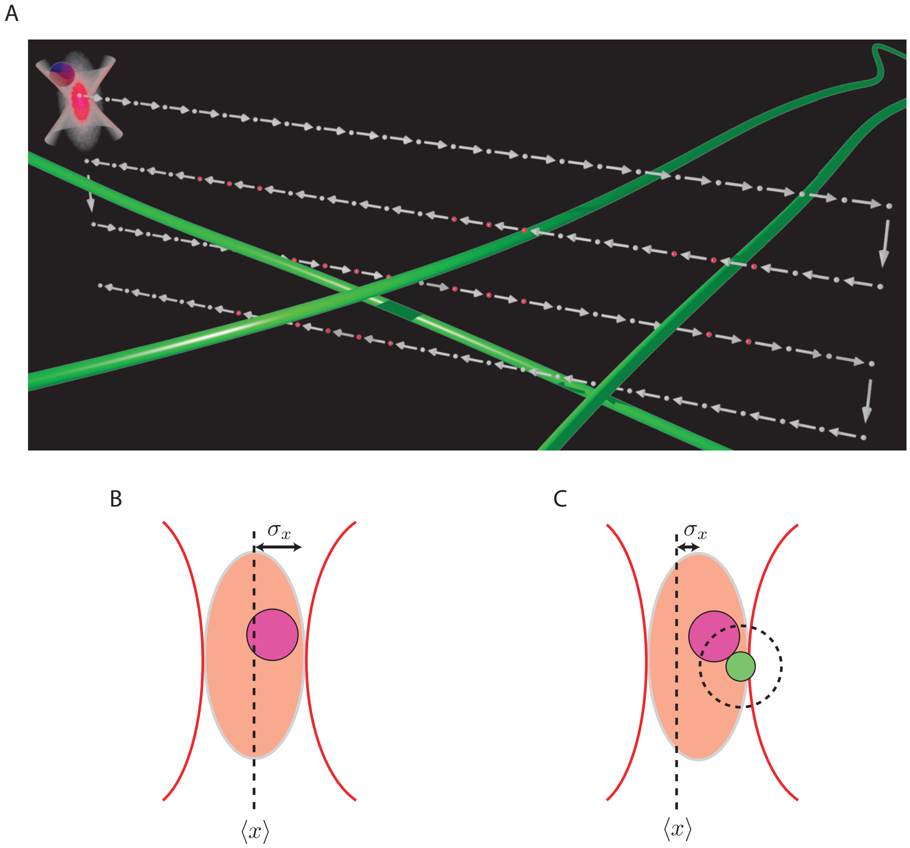

Figure 6.7: Raster scanning strategy with feedback. **A** - Collagen fibrils are detected by a rapid raster scan of the trapped particle through the network. The presence of fibrils was detected by the change of the standard deviation of the tracer particle's thermal motion when a fibril is present (compare **B** and **C**). Voxel occupancies are only acquired at positions close to the filaments (red grid points in **A**), eliminating the imaging of empty space.

enough to estimate the means $\langle \alpha \rangle$ and the standard deviations σ_α (figure 6.7C) of the particle's motion. Since the unknown offsets of the position signal change between grid positions the tracer particle's mean positions are not a useful measure. However, the position standard deviations σ_α are independent from the unknown offsets and can be compared to the reference standard deviations of diffusion in the empty trapping potential (figure 6.7B), given by $\sigma_{\alpha,ref} = \sqrt{k_B T / k_\alpha}$ (compare equation 2.39), where $\alpha = x, y, z$. If a filament is present in the trapping volume, the particle can no longer explore the entire volume, and the standard deviation of the particle's motion along at least one axis is expected to decrease (figure 6.7C).

For experiments described in this chapter, a decrease of at least one of the standard deviations to $\sigma_\alpha < 0.4\, \sigma_{\alpha,ref}$ was empirically found to be a reliable measure to determine whether fibrils were close to a given grid position. Voxel occupancies were acquired at all grid positions that fulfilled this condition, *and at their nearest neighbors.*

The raster scanning strategy described in this section is a feedback mechanism on the dwell time at a certain grid position: If no filament is present, the grid position is not revisited for the acquisition of a voxel occupancy, and the full dwell time spent at it is 100 ms. If the tracer particle interacts with a filament, the voxel occupancy is measured by acquiring a 4 s long time trace of the particle's diffusion, and the total dwell time at the grid position is 4.1 s. This approach can significantly decrease total acquisition times depending on the amount of "empty" space in the imaging volume. An example is discussed in section 6.3.1.4.

6.3.1.3 Acquiring thermal noise images inside a collagen network: essential steps

The following steps are necessary in order to successfully image a large volume inside a collagen network: First, a grid is defined corresponding to the positions at which individual voxel occupancies are to be acquired (figure 6.4). Second, the trapped tracer particle is navigated to an empty space in the network, at which no filaments intersect the trapping volume, and the detector is calibrated (see section 2.3.2). In this work, this calibration position always corresponded to the first grid position, but this is not a requirement. Third, after calibration, the particle is rapidly stepped through the grid (raster scan), with a short detector response acquisition time at each grid position (here: 100 ms), and the positions at which the tracer interacts with the network's filaments are found (see section 6.3.1.2). Fourth, at all positions found this way, time traces of the detector response $S_{\alpha,total}$, long enough to populate three-dimensional position histograms (i.e. voxel occupancies), are recorded (here: time traces were 4 s long). Fifth, the particle is released from the optical trap by closing the shutter in the trapping beam path. As soon as the particle has diffused away, the shutter is re-opened, and the constant offsets $S_{\alpha,fibril}$ are acquired by averaging short (here: 20 ms long) traces of the signal at each of the positions from step four. Finally, the corrected detector responses $S_{\alpha,position}$ can be calculated by equation 6.8. The particle's position time traces at each grid position are subsequently found by calibrating $S_{\alpha,position}$, and the voxel occupancy at each position can be computed. The cumulative voxel occupancy is then calculated as in section 5.3.1.1.

In order for the described approach to succeed, the positions of the fibrils in the sample chamber are not allowed to change significantly between the acquisition of each $S_{\alpha,total}$ and its corresponding offset $S_{\alpha,fibril}$. However, as discussed in section 2.5.6, the instrument had a drift of 10 nm/min under optimal conditions, shifting the sample on the order of one fibril diameter within 15 min.[7] Consequently, all attempts to implement the described "offset correction" failed when a time longer than 15 min passed between the acquisition of $S_{\alpha,total}$ and $S_{\alpha,fibril}$, limiting the total data acquisition time, and thus the total volume that could be explored to approximately 225 individual trapping volumes. A possible method to circumvent this limitation is discussed in chapter 7.

Steps two through five of the discussed method were implemented as a Labview Realtime program, and can be executed with minimal user interaction. Before calibration, the user must manually move the tracer particle to a pore in the network. A pore can be identified by realtime monitoring of the (uncalibrated) two-dimensional xy and yz position histograms of the tracer particle's diffusion, computed from the continuously recorded signals

---

[7] Additionally it can not be excluded that some fibrils move relative to the sample chamber during data acquisition. However, by monitoring the signals $S_{\alpha,fibril}$ for an extended amount of time, it was verified that the total drift of the position of the monitored fibrils was on the order of the known drift of the sample chamber. Any additional motion of the fibrils relative to the sample is therefore likely a small effect.

$S_{\alpha,total}$. Structures in the trapping volume are clearly visible in these histograms, and the volume can be moved around in nanometer-sized increments until an empty space in the network is found. Further, after step four, the user must determine whether the tracer particle has diffused sufficiently far away before re-opening the shutter and continuing to step five.

6.3.1.4 Thermal noise image of a section through a collagen gel

In this section, we will verify that performing a raster scan with feedback (see section 6.3.1.2) can indeed decrease the total acquisition time of thermal noise images in biopolymer networks. For this purpose, a section of a collagen network (concentration 2.4 mg/ml) was imaged. The section was defined by a grid of 1 x 81 x 5 (x x y x z) points, which corresponds to an approximate *depth* x *width* x *height* of the imaged volume of $0.3\,\mu$m x $8\,\mu$m x $2\,\mu$m (figure 6.8). If voxel occupancies with an integration time of 4 seconds were to be acquired at each of the 405 grid positions, the total acquisition time would approximate 27 min. However, the raster scan found only 157 grid positions in proximity to fibrils (some of which were false positives, compare figure 6.8), reducing the total acquisition time to approximately 10 minutes, an increase of over 60% in efficiency. Voxel occupancies were acquired only at these positions and figure 6.8 shows a thermal noise image of the cumulative occupancy (isovalue 10).

It is apparent from the excluded volumes in the image that four fibrils intersected the scanned section, the leftmost at a shallow angle, and the other

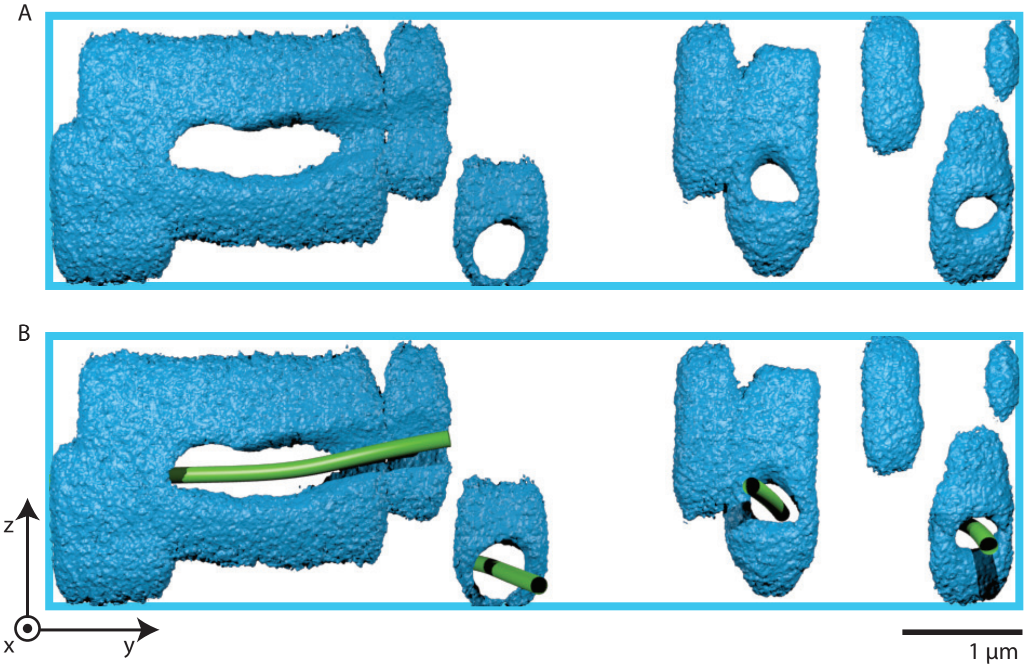

Figure 6.8: Thermal noise image of a section through a collagen gel. Filaments were detected by a raster scan along a two-dimensional grid consisting of 1 x 81 x 5 grid positions (x x y x z). This area is approximately given by the blue frames in **A** and **B**. Voxel occupancies were only acquired at positions at which filaments were detected, and at their nearest neighbors. **A** - Thermal noise image of the cumulative voxel occupancy (isovalue 10). Four fibrils intersected the sectional scan, and are sketched in **B** to guide the eye (green filaments). The thermal noise image of the individual trapping volume displayed in the top right is the position at which the detector was calibrated. Other imaged trapping volumes that are not in proximity to the fibrils were false positives during the raster scan. The collagen concentration of the network was 2.4 mg/ml.

three fibrils at steep angles, as sketched in figure 6.8B to guide the eye. If many such scans are acquired within the same network, the mean distance between fibrils can be determined, which is called the pore size of the network. Fibril diameters can be extracted as well, as we will see in section 6.3.2.

6.3.1.5 Thermal noise imaging of network junctions

We will now turn our attention to imaging local network architecture. The location of a network junction was estimated from bright field microscopy images (figure 6.3B), and a trapped tracer particle was moved into its vicinity. By realtime monitoring of the (uncalibrated) two-dimensional xy and yz position histograms computed from the detector responses $S_{\alpha,total}(\boldsymbol{b}_p, \boldsymbol{b}_f)$ (section 6.3.1.1), it was verified that collagen fibrils were present at the estimated position. The trapping volume was then moved to an adjacent pore in the network (<500 nm from the junction), and the detector was calibrated. The grid size for the raster scan was chosen to extend over the entire junction by a best guess based on the bright field microscopy image. The positions of the filaments were then found by the raster scan, and subsequently voxel occupancies were measured for all trapping volumes in the proximity of fibrils. In the following, we will discuss the resulting thermal noise images of two such acquisitions.

Figure 6.9A shows the thermal noise image (isovalue 10, grid size 7 x 7 x 2) of a junction in a collagen network (concentration 0.6 mg/ml). Several fibrils meet at this junction (sketched in figure 6.9B), and we will focus on

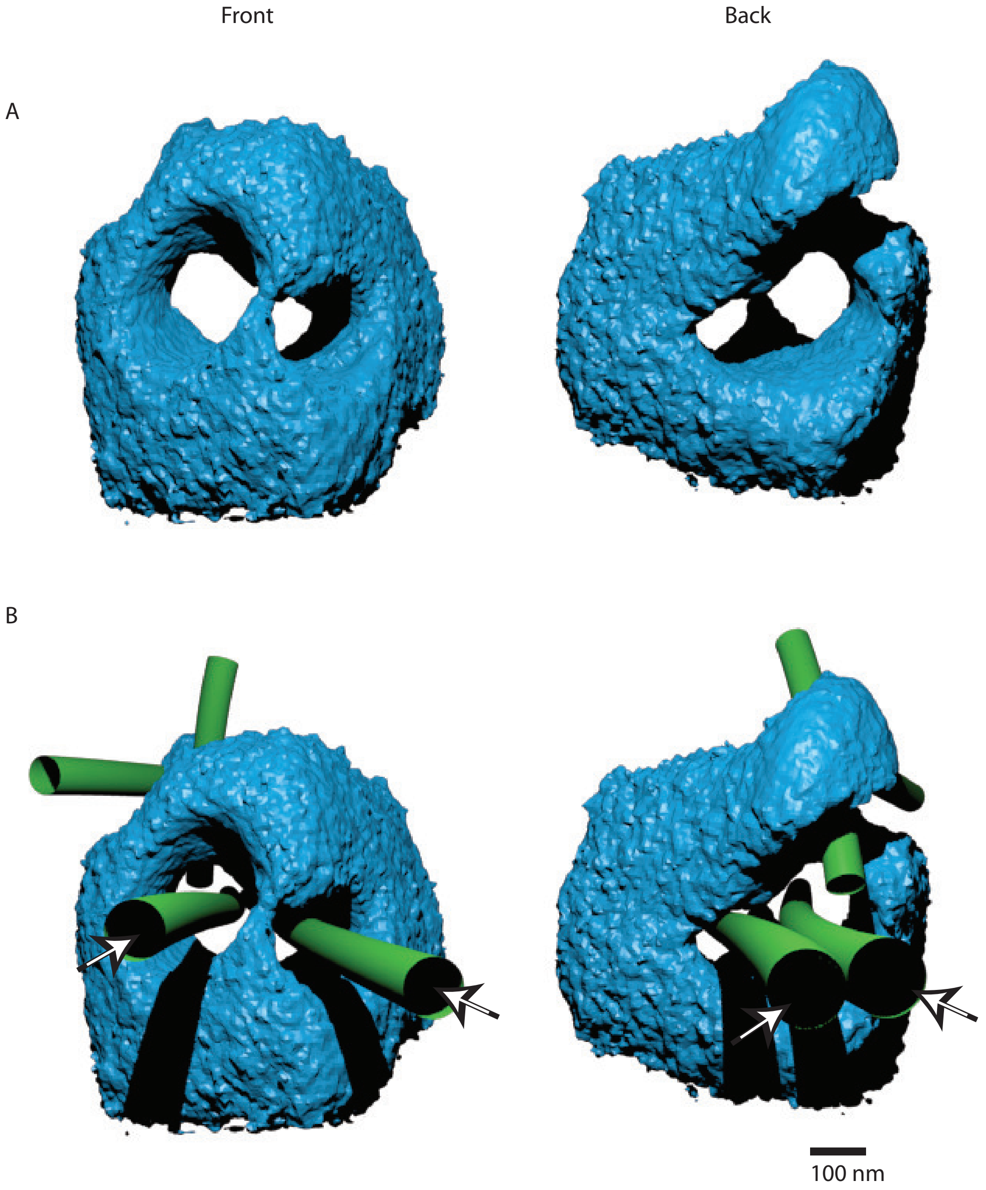

Figure 6.9: Thermal noise image (isovalue 10) of the branching of two collagen fibrils, without (**A**) and with (**B**) sketches of the fibrils (green). Both the front and the back view of the three dimensional image are shown. The fibrils (marked by arrows in **B**) are seen to branch from the back of the image to its front. The collagen concentration of the network was 0.6 mg/ml.

two of them which are marked with arrows. In the front view, there is a thin strand of accessible volume visible between the fibrils, which vanishes quickly when we follow them towards the back of the scanned volume. Thus, the distance between the fibrils decreases from slightly larger than the tracer particle's diameter to smaller than the particle's diameter, and the particle can no longer diffuse in between the fibrils. This could indicate the branching of a bundle of two fibrils.

The thermal noise image of a second junction (isovalue 10, grid size 11 x 11 x 2, collagen concentration 2.4 mg/ml) is shown in figure 6.10. 12 views of the same image are displayed, each rotated by a further 30 degrees around the optical axis. The excluded volume of the image consists of two channels, indicating the presence of two fibrils which intersect each other at an angle close to 90 degrees. A close up view of the junction reveals its submicroscopic structure (figure 6.11): The channel formed by fibril 1 appears to be located above the channel formed by fibril 2. This feature can be quantified by inspecting a slice of the cumulative occupancy perpendicular to the orientation[8] of fibril 2, at the location of fibril 1 (figure 6.11B). Fibril 2's channel is 160 nm below the excluded volume created by fibril 1, indicating that the diameter of fibril 2 was 160 nm, assuming the fibrils were lying on top of each other (figure 6.11C). Fibril 2's diameter was also independently measured using the method described in section 6.3.2.3, with a result of (150 ± 30) nm, strongly supporting the hypothesis that the two fibrils were in contact. Further, this

---

[8] the orientation of fibril 2 was found by the algorithm explained in section 6.3.2.2.

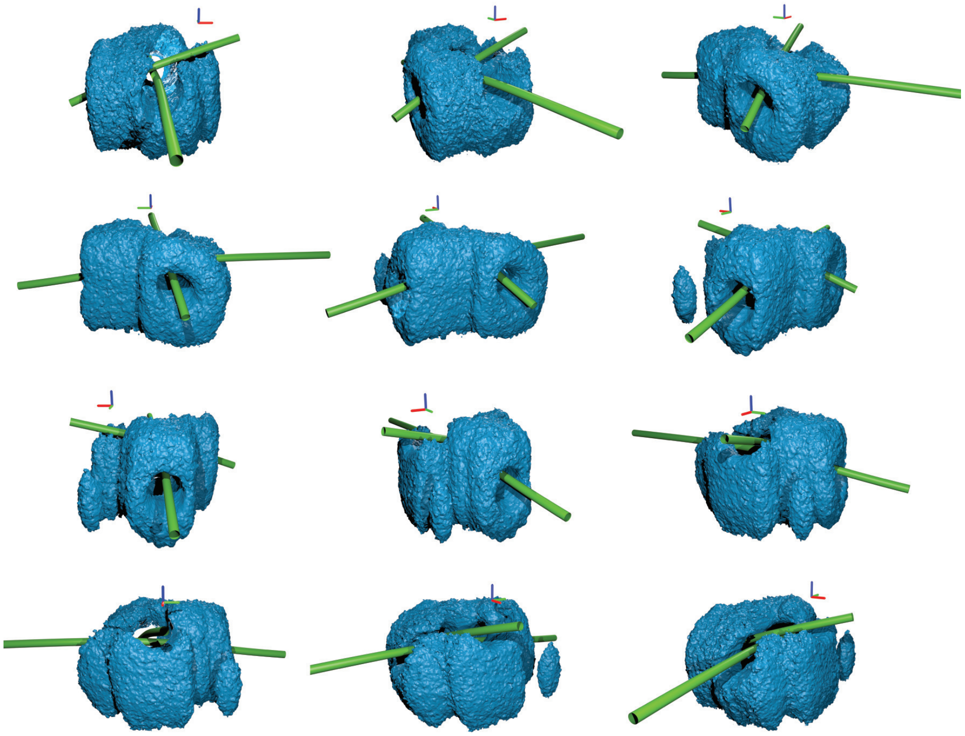

Figure 6.10: Thermal noise image of a junction in a collagen network. Twelve views of the same image are shown, each rotated by a further 30 degrees around the optical axis. The image shows the presence of two fibrils (sketched in green to guide the eye) intersecting each other at an angle of approximately 90 degrees. The axis cue has a length of 200 nm in each direction, and the collagen concentration of the network was 2.4 mg/ml.

diameter agrees well with typical fibril diameters expected for the polymerization conditions used in this work [154].

Thus, thermal noise imaging reveals the submicroscopic local structure of collagen networks, and the experiments shown here pave the way for the study of the behavior of junctions under applied loads. Possible experimental designs to apply such loads compatible with photonic force microscopy are discussed in chapter 7.

6.3.2 Quantitative analysis of thermal noise images in collagen networks

We will now discuss how the effective interaction energy between the tracer particle and the filaments (i.e. the LRO, see section 2.4.1) can be extracted from the acquired data. Recall the calculation of the LRO along microtubules as discussed in section 5.3.2: Due to the radial symmetry of the fluctuations of the filament the dimensionality of the LRO can be reduced from three to one dimension without loss of information. This is possible by calculating the LRO of individual voxel occupancy measurements, collapsing them along the filament axis into two dimensions, and finally averaging on concentric circles centered on the filament to find the radial behavior. Two complications must be overcome to make this approach viable for measurements in collagen networks: First, the diameter of collagen fibrils is too large for them to be imaged using individual voxel occupancy measurements. Only thermal noise images created from cumulative voxel occupancies can image

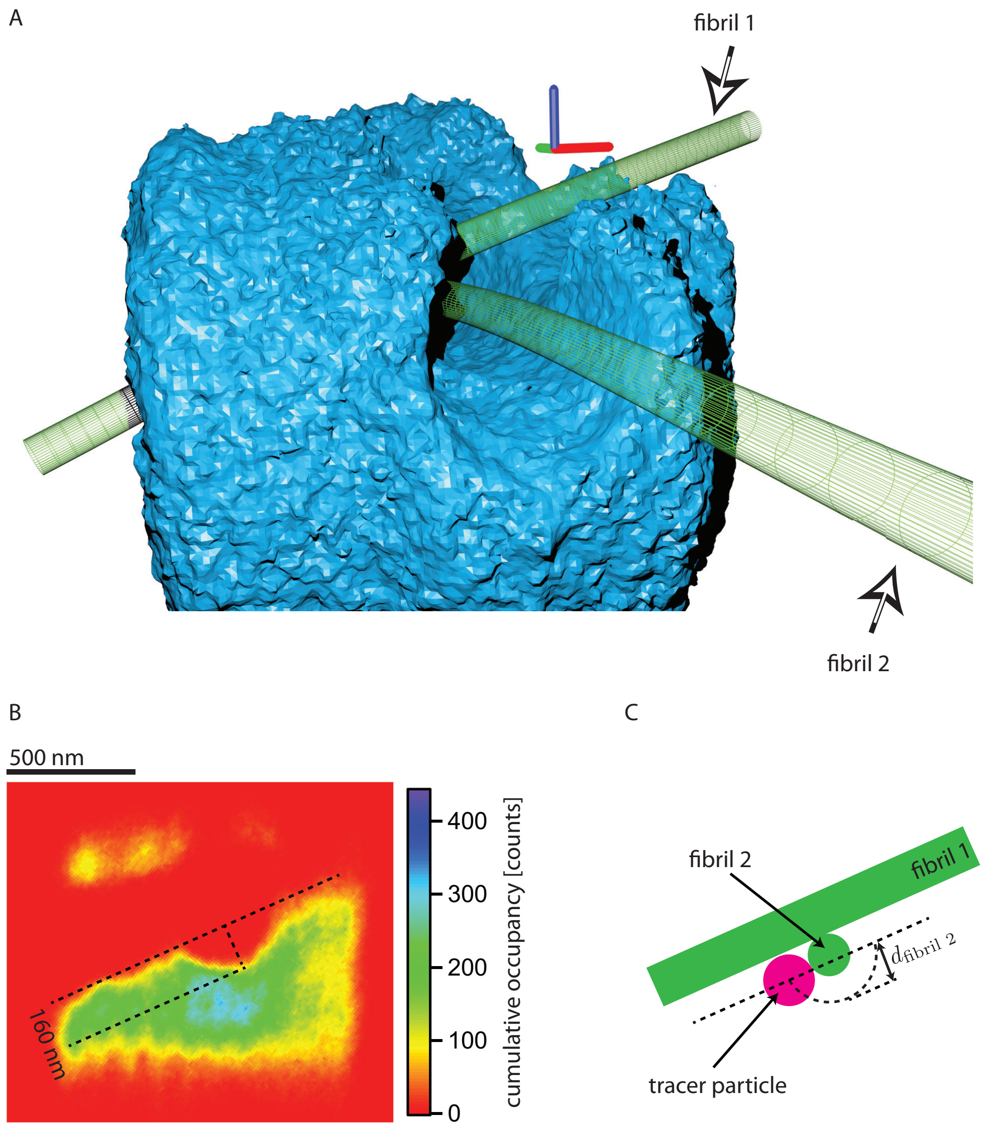

Figure 6.11: Submicroscopic structure of a junction of collagen fibrils.
A - Zoomed view of the thermal noise image shown in figure 6.10. The axis cue has a length of 200 nm in each direction. **B** - Slice of the cumulative occupancy perpendicular to fibril 2 at the position of fibril 1. The channel formed by fibril 1 is approximately 160 nm above the channel formed by fibril 2. This indicates that fibril 2 had a diameter of 160 nm if the two fibrils were lying on top of each other (**C**).

collagen fibrils. A method must therefore be developed to combine the LROs of several individual voxel occupancy measurements into one cumulative LRO. Second, unlike microtubules in the single filament assay described in section 5.2.3, the orientation of collagen fibrils in the gel is not known - in particular, the fibrils are not confined to one xy plane in the sample chamber. Thus, after imaging a filament, its orientation must be algorithmically found before the radial behavior of the LRO can be analyzed.

6.3.2.1 Cumulative LROs

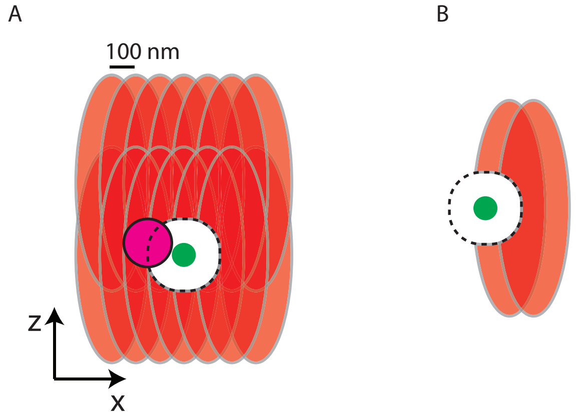

Figure 6.12: Geometry for the computation of cumulative LROs. **A** - Voxel occupancy measurements (red) around a fibril (green). The tracer particle is drawn in pink, and the excluded volume is indicated by a dashed line. **B** - LROs computed from voxel occupancy measurements with different amounts of excluded volume have different energy offsets (see text on page 179).

The LRO describes the effective interaction energy between the tracer particle and the imaged structure up to an additive constant $\tilde{C}$, and can be computed from each individual voxel occupancy measurement by equation

2.54. It was argued that the constant $\tilde{C}$ is of no significance, since the offset of an energy landscape is arbitrary by the work-energy theorem. However, we now want to combine several LROs computed from individual occupancy measurements (figure 6.12A), some of which overlap with the scanned structure. These LROs may have different offsets $\tilde{C}$. Consider two such occupancy measurements, as shown in figure 6.12B. For each one individually, the LRO is equal to the effective energy landscape explored by the particle. However the two energy landscapes have different offsets $\tilde{C}$. During the occupancy measurement on the left a larger part of the trapping volume was inaccessible to the diffusion of the particle than for diffusion in the right trapping volume. Thus, for the left voxel occupancy measurement, particle positions are distributed over a smaller volume, leading to a larger occupancy value for each voxel, which results in a larger constant $\tilde{C}$. In order to combine the two calculated LROs their offset in energy must be adjusted. For this purpose, the average energy difference between each of the overlapping voxels (dark shaded area in figure 6.12B) was calculated, weighted by their error (see equation 2.37). One of the two LRO measurements was then adjusted by addition of this energy difference to equalize the energy offsets of the measurements. In the non-overlapping volumes, the cumulative LRO is then given by the corresponding values of the individual LROs, and within the overlapping volume it is given by their weighted average. The cumulative LRO of more than two voxel occupancy measurements is found by successive addition of individual LROs as outlined above.

6.3.2.2 Determination of the orientation of imaged fibrils

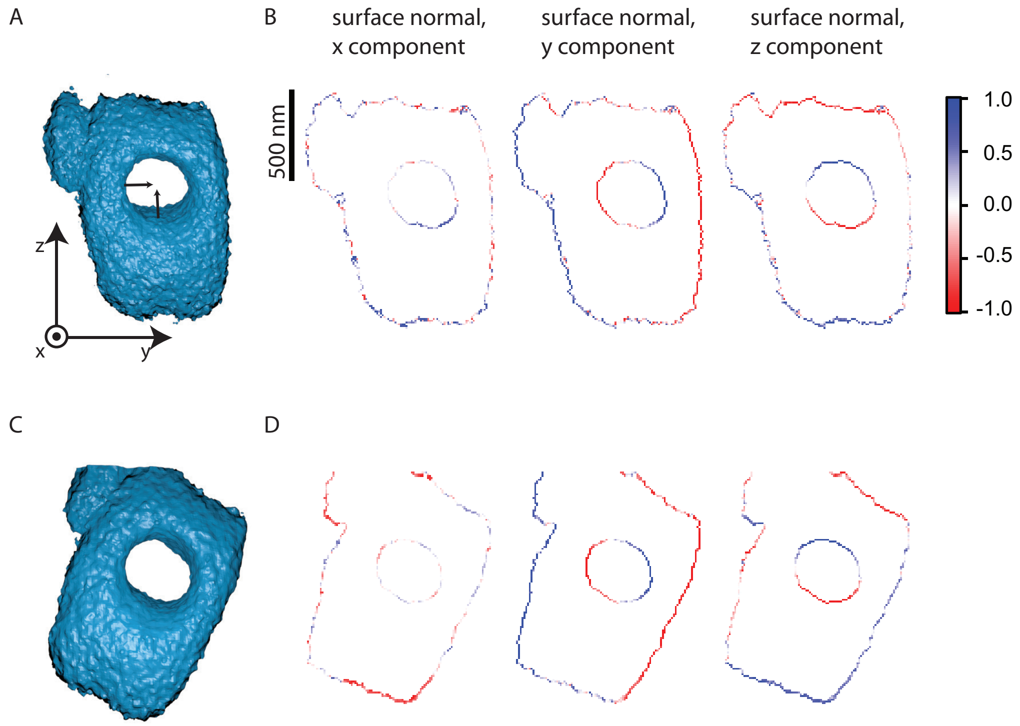

Figure 6.13: Determination of fibril orientation. **A** - Thermal noise image (isovalue 10) of a fibril in a collagen network. It is evident from the shading of the excluded volume that the fibril is not aligned with the x-axis of the coordinate system. From the components of surface normals along the central slice through the thermal noise image (**B**) the fibril's orientation can be computed. The thermal noise image can then be rotated to align the fibril's orientation with the x-axis, and the surface normals along x direction vanish, as expected (**D**).

Fibrils in a collagen gel are oriented in random directions, and can be curved and thus change their direction along their contour. In order to analyze the radial behavior of the cumulative LRO, the local direction of the imaged fibril must be determined from the acquired data. Consider the thermal noise image of an individual fibril shown in figure 6.13A (image acquired on a 3 x 15 x 3 grid, collagen concentration: 2.4 mg/ml). It is clear from the channel's shading that the filament was not oriented along the current x-axis (i.e. it was not perpendicular to the yz-plane). A method is now introduced to compute the unit vector along the fibril's contour. Using this unit vector, the thermal noise image, cumulative occupancy, and cumulative LRO can be rotated so that the fibril is aligned with the x-axis of the coordinate system.

The method requires that the fibril is already roughly aligned with the desired orientation, e.g. by manual rotation of the thermal noise image. Let us examine a slice through the center of such a thermal noise image, as shown in figure 6.13. Since the thermal noise image has already been roughly aligned, the cross-section of the excluded volume appears as a circle or ellipse. The surface normals of voxels along this ellipse point towards the center of the fibril, and their components are plotted in figure 6.13B. Consider now all pairs of surface normals around the excluded channel which are separated by 90 degrees. An example of two such normals are sketched into figure 6.13A. The normalized cross product of each such pair of vectors yields a resulting unit vector into the local direction of the fibril. The unit vectors resulting from all pairs of cross products around the cross-section of the channel are averaged to yield the mean local direction of the fibril. The thermal noise image is then rotated to align this mean unit vector with the x-axis of the coordinate system. For the example shown here, the rotated view is drawn in figure 6.13C. The surface normals of the rotated thermal noise image's channel (figure 6.13D) have vanishing components along the x-axis, as expected for an image of a fibril aligned with this axis, verifying that the method indeed rotates the fibril in the desired direction.

6.3.2.3 LROs and fibril diameters

Consider now the cumulative LRO of the same measurement whose thermal noise image is shown in figure 6.13, computed as described in section 6.3.2.1, and rotated into the direction of the fibril as shown in section 6.3.2.2. A slice perpendicular to the fibril through the center of the three-dimensional LRO is plotted in figure 6.14A. Note that since the LRO was rotated, the optical axis of the microscope no longer lies within the drawing plane. The excluded volume has an elliptical shape, and is not circular as one would expect (see figure 6.14B for a fit). Such elliptical shapes were found for all fibrils analyzed this way (N = 8). All fibrils approximately aligned with an xy-plane of the PFM showed elliptically shaped excluded volumes for which the minor axis of the ellipse was aligned with the optical axis. This could imply that the cross-sectional symmetry of the fibril is broken during polymerization, for example by gravity – an unlikely scenario. More likely, the observed ellipticity is caused by position detection artifacts: Light that travels through the fibril, but is not scattered by it, receives a phase shift, which influences the axial detection of the tracer particle's position (see section 2.3.1).

Due to the elliptical shape of the LRO it is not possible to compute the one-dimensional radial LRO by averaging along concentric circles as was

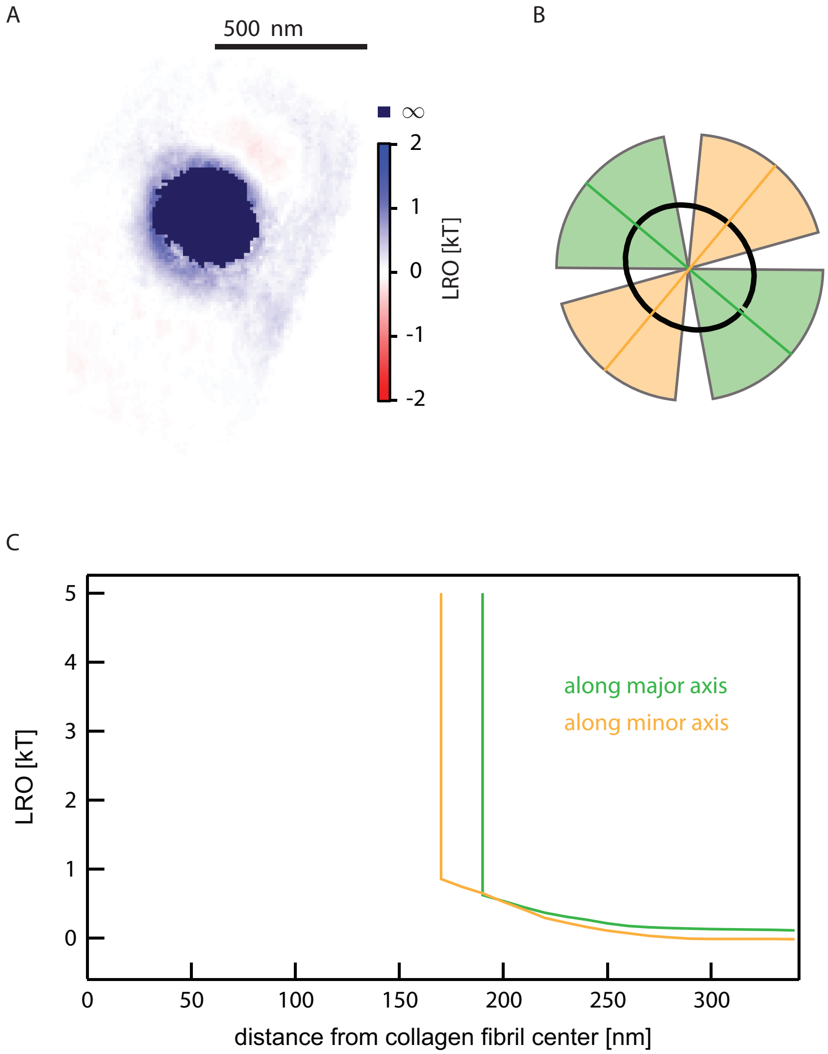

Figure 6.14: Cumulative LRO of a collagen fibril. **A** - Slice through the three-dimensional LRO, perpendicular to the fibril's local orientation. Same data as in figure 6.13. The excluded volume (infinite values of the LRO) was elliptical, and not circularly symmetric as expected. **B** - An ellipse was fitted to the excluded volume, and the radial behavior of the LRO found for the major and minor axis separately. For each of the two axes two cones were defined, and data with equal distance from the fibril's center were averaged within the corresponding cones. The resulting radial LROs are shown in **C**.

done for microtubules (section 5.3.2.3). Rather, two radial LROs were computed, one each for the behavior along the major and minor axis of the ellipse respectively. In order to average the two-dimensional data, two sets of cones were defined (figure 6.14B). The opening of the cones belonging to the major axis of length a is given by comparing a circle with radius $a/2$ centered at the center of the ellipse to the behavior of the ellipse: The cone describes the range over which circle and ellipse diverge by less than 5%. The cones for the minor axis were computed in an analogous fashion. Within each set of cones, data points of the two-dimensional LRO equidistant from the center of the excluded volume were averaged to yield the one-dimensional, radial LRO associated with the respective axis. Both radial LROs are plotted in figure 6.14C. Recall the one-dimensional LROs for a grafted microtubule with one free end. Voxels along energy barriers of up to $4\,k_BT$ can easily be reached by the particle's diffusion during the given observation time of 4 seconds per individual occupancy measurement. For the collagen fibril though, the highest explored LRO above zero effective interaction energy is $\sim 0.8\,k_BT$, after which the effective interaction energy immediately increases to infinity. The absence of voxels at high energy levels implies a very stiff filament without transversal fluctuations, since transversal fluctuations would introduce such voxels (see sections 5.3.2.2 and 5.3.2.3). The small change in effective interaction energy from the infinite energy barrier outwards is not yet understood. It is unlikely that this effect is caused by electrostatic interactions between the particle and the collagen fibril, since such interactions are shielded by the ions of the PBS buffer, and decay away over a Debye length of less than a nanometer [131]. The long range of the decay of over 100 nm therefore cannot be explained by electrostatics.

The infinite energy barriers are located at a distance of 170 nm and 190 nm from the fibril's center respectively. Assuming that the fibril is stationary, we may compute its diameter from these values. Since the value along the minor axis is likely distorted due to artifacts on the detector, we will consider the radius of the excluded volume to be 190 nm. With a tracer particle radius of 105 ± 15 nm equation 2.47 yields a fibril radius of 85 ± 15 nm, in excellent agreement with the fibril diameter extracted in section 6.3.1.5 for identical polymerization conditions.

6.4 Conclusions

In this chapter, quantitative thermal noise images of the local architecture of biopolymer networks are shown for the first time. Two major difficulties were overcome to facilitate these images: First, a method was developed to correct the signal on the detector for light scattered by the collagen fibrils. Second, an efficient scanning strategy based on a feedback mechanism was introduced, which can significantly reduce the total acquisition time for large scale images. The images of two junctions of collagen fibrils were discussed to demonstrate the wealth of information accessible by the novel technique.

Additionally, a method to compute the effective interaction energy (cumulative LRO) between the tracer particles and the filaments was introduced.

From its analysis, it was concluded that collagen fibrils do indeed behave like stiff rods and do not show any measurable transversal fluctuations. Further, the fibril diameter could be extracted from the data, and agrees well with expected diameters for the present polymerization conditions.

Together with chapter 5 these results pave the way for the imaging of networks of semi-flexible polymers, such as actin.

Chapter 7

Summary and future work

It is the goal of this work to develop a novel technique capable of imaging the local architecture of biopolymer networks with super resolution, while simultaneously extracting the distribution of forces acting on the individual cross-linked filaments. Such measurements are necessary for a deep understanding of the macroscopic mechanical properties of biopolymer networks, and are expected to help in the design of novel biomimetic materials. As was argued in the introduction (section 1.3.3), the transversal fluctuations of a semi-flexible filament report on its tension. If the transversal fluctuations of the filaments in a network can be measured, the distribution of forces in the network can be determined.

In this dissertation, it is shown that thermal noise imaging implemented using a PFM can accomplish both: The measurement of transversal fluctuations of individual microtubules is described in chapter 5, and the visualization of the submicroscopic local architecture of a network of collagen fibrils is shown in chapter 6.

Even though collagen fibrils in a network do not exhibit any measurable transversal fluctuations and behave like stiff rods (see section 6.3.2.3), their thermal noise images contain a wealth of information about their local architecture that had been inaccessible up to now. For example, as shown in section 6.3.1.5, thermal noise imaging can visualize the submicroscopic details of junctions in collagen networks. Thus, the local behavior of such junctions under local or global loads can now be studied under physiological conditions for the first time. The response of the network to local loads is of biological interest, since living cells in a collagen network induce and react to local stress variations in the network and locally remodel the network around them [142]. In order to model such local loads, magnetic beads with magnetic moment $\boldsymbol{m}$ can be embedded in the network and a force applied by a magnetic field gradient $\partial B_\alpha / \partial \alpha$, $\alpha = x, y, z$, created by a pair of anti-parallel current carrying coils (see figure 7.1) [140]. The force that each magnetic bead enacts on the network is then

$$\boldsymbol{F} = (\boldsymbol{m} \cdot \nabla) \, \boldsymbol{B}. \tag{7.1}$$

The size of the magnetic beads must be chosen to be on the order of or larger than the pore size of the network; otherwise the applied force will just move the bead through the network rather than applying a local load to it. Thus, for the networks used in this work the magnetic beads must be several microns in diameter. A pair of such coils is currently being implemented into the PFM used in this work. Once the integration has been completed junctions in the network can be imaged before and after the application of local loads of different magnitudes.

Global strains can be applied to the network by polymerizing the col-

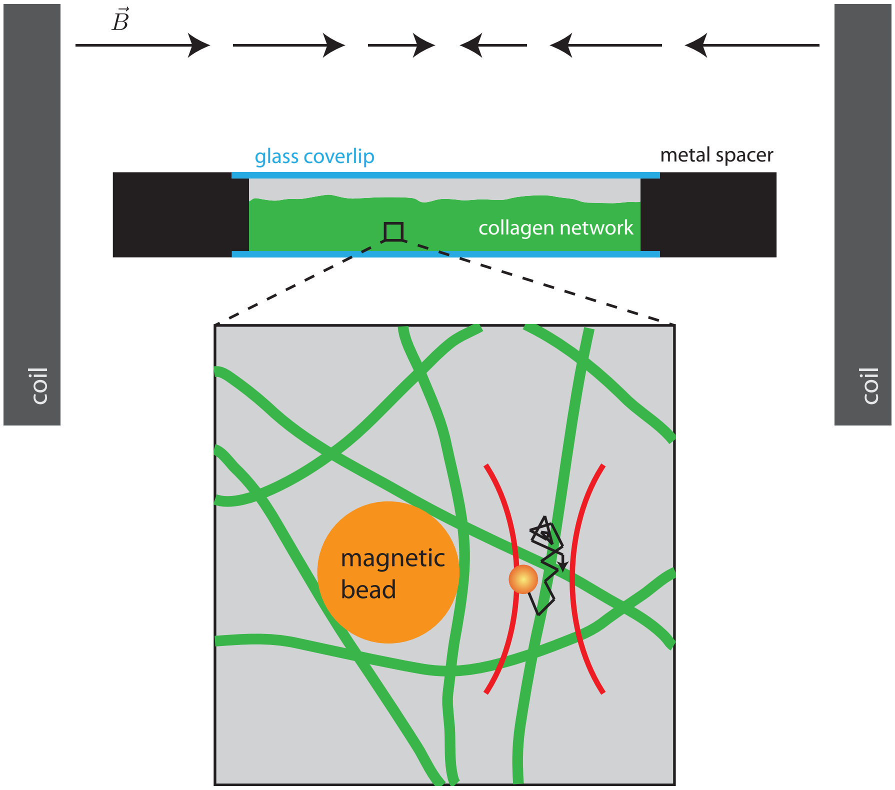

Figure 7.1: Application of local loads to a collagen network by magnetic beads. Magnetic beads with magnetic moment $\boldsymbol{m}$ are embedded in a collagen network, and a magnetic field gradient $\partial B_\alpha/\partial\alpha$, $\alpha = x, y, z$, is applied by two anti-parallel current carrying coils. The force acting on the bead is then $\boldsymbol{F} = (\boldsymbol{m} \cdot \nabla)\boldsymbol{B}$.

lagen gel in contact with both the top and the bottom coverslip of the sample chamber, and then shearing the coverslips against each other. Implementing this geometry, without impacting the exceptional long time scale stability of the instrument is challenging though.

In vivo, collagen molecules in fibrils are typically cross-linked, and such cross-linking has been speculated to have an impact on the junctions in the network [35, 142]. By thermal noise imaging, the effect of different cross-linking reagents on the submicroscopic behavior of individual junctions under local or global loads can now be directly measured, and is expected to yield valuable insights for the design of novel materials.

In order to gain good statistics of the behavior of junctions in a network under load, many junctions in the same network have to be imaged. However, as discussed in section 6.3.1.3, currently data acquisition is limited to ∼15 min of imaging, which corresponds to 225 individual occupancy measurements, each integrated for 4 seconds. While this is sufficient to image the volume around a single junction, a large part of the network covering several junctions cannot be explored. Recall that this limitation is due to the long timescale drift of the instrument of 10 nm/min. The particle's position signal must be corrected for the constant offsets introduced by light scattered by the collagen fibrils (see section 6.3.1.1). For that purpose the constant offsets $S_{\alpha,fibril}$, $\alpha = x, y, z$, caused by the collagen fibrils must be recorded at each grid position *after* acquisition of the signals $S_{\alpha,total}$ at each position of the grid. However, during 15 min of imaging (i.e. of acquiring the $S_{\alpha,total}$), the instrument drifts by approximately one collagen fibril diameter. Thus, when revisiting each grid position to acquire the signals $S_{\alpha,fibril}$ the fibrils are no longer present at their original positions, the signals $S_{\alpha,fibril}$ have changed, and the correction of the position signal fails. Thus, in order to facilitate large scale imaging, the already exceptionally small long timescale drift must either be further reduced, a very challenging endeavor, or the problem must be circumvented. One elegant solution that does not depend on a further reduction of the instrument's drift involves acquiring the signals $S_{\alpha,total}$, and immediately, before proceeding to the next grid position, the signals $S_{\alpha,fibril}$. By this approach the position offsets at a certain grid position in the sample are measured immediately after measuring the corresponding total signals, and the sample will have drifted by an insignificant amount between the measurements. One then proceeds to acquire data at the next grid position, again first measuring the total signals, and immediately afterwards the offsets. Thus, in principle one could then acquire data for as long a time and as large of a volume as desirable. Implementing this concept is non-trivial though: In order to acquire the signals $S_{\alpha,fibril}$ the particle must be released from the trap; however in order to measure the signals $S_{\alpha,total}$ at the next grid position a particle must be present in the trapping volume. This can be realized by use of a second optical trap (see figure 7.2). The red beam in figure 7.2 indicates the regular trapping and tracking beam, which is used during the acquisition of voxel occupancies. The optical trap indicated in blue has the sole purpose of providing a "storage position" for the tracer particle which keeps

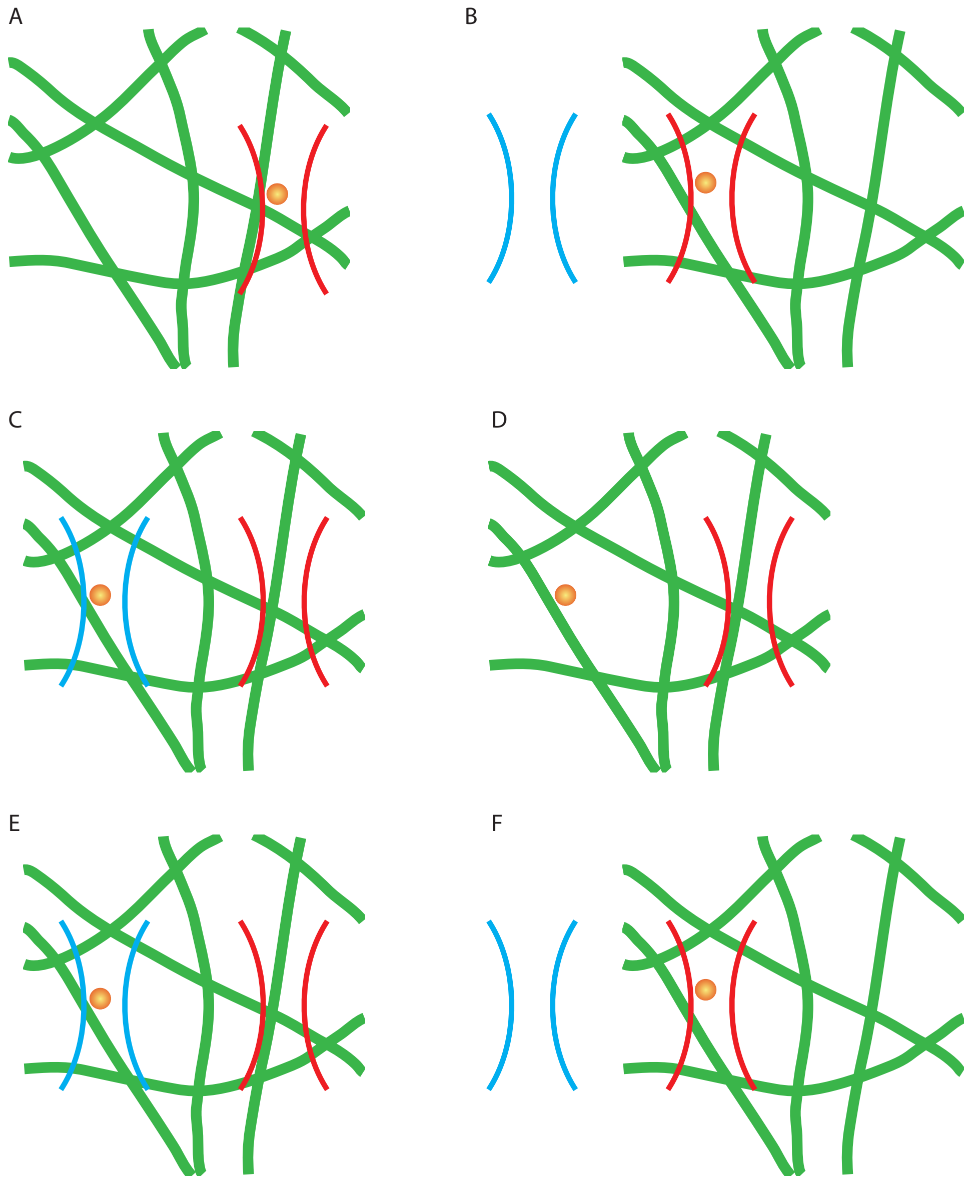

Figure 7.2: Strategy for immediate offset correction. See page 191 for a detailed description.

it from diffusing away when the red trapping volume needs to be empty so that the signals $S_{\alpha,fibril}$ can be recorded. The blue optical trap will therefore be referred to as the "storage" trap. Acquisition of data at each grid position then follows the following sequence: Initially (figure 7.2A) the storage trap is switched off, and the signals $S_{\alpha,total}$ are recorded. Subsequently, the sample is moved several micrometers relative to the trapped tracer particle (figure 7.2B), positioning the particle at a position in the network at which it can be temporarily stored, and the (blue) storage beam is switched on. The sample is then rapidly[1] positioned so that the (red) trapping beam overlaps the original grid position, while the probe particle is "ripped" out of the (red) optical trap and remains left behind at its new position in the sample. This new position must overlap with the trapping volume of the storage trap, in which the probe is now trapped (figure 7.2C). The signals $S_{\alpha,fibril}$ can now be acquired since the (red) trapping beam is only scattered by the collagen fibrils close to the focus, and not by the tracer particle. The (blue) storage beam may be causing artifacts on the detector, and it may be advantageous to "blink" it on and off, i.e. to switch between figure 7.2D and E. Switching the storage beam on and off fast enough keeps the stored particle from diffusing away, while short time traces of the offset signals $S_{\alpha,fibril}$ can be acquired every time the storage beam is off. After the position offset has been determined with sufficient fidelity, the sample is rapidly stepped to move the tracer particle back into

---

[1] Rapid positioning of the sample may cause large inertial forces which could deform the network. These forces can be avoided by moving the storage trap using beam steering optics instead of moving the sample.

the (red) trapping and tracking beam (figure 7.2F). The particle can then be moved to the next grid position, and the described acquisition sequence can be restarted from the beginning.

Integration of the electromagnetic coils and the storage trap into the PFM will enable the large scale visualization of biopolymer networks under loads. Thermal noise imaging may then be applied to networks of semi-flexible filaments. Their local architecture can be visualized, and their transversal fluctuations measured by combining what we have learned from the experiments on fluctuating microtubules and stiff collagen networks. These experiments are expected to yield the insights necessary to test existing theories, and to help in the design of novel biomimetic materials.

Bibliography

[1] B Alberts. *Molecular Biology of the Cell.* Garland Science, 5th edition, 2008.

[2] M W Allersma, F Gittes, M J deCastro, R J Stewart, and C F Schmidt. Two-dimensional tracking of ncd motility by back focal plane interferometry. *Biophys. J.*, 74(2):1074–1085, February 1998.

[3] L A Amos and J Löwe. How Taxol stabilises microtubule structure. *Chem. Biol.*, 6(3):R65–R69, March 1999.

[4] A E Aplin, A Howe, S K Alahari, and R L Juliano. Signal Transduction and Signal Modulation by Cell Adhesion Receptors: The Role of Integrins, Cadherins, Immunoglobulin-Cell Adhesion Molecules, and Selectins. *Pharmacol. Rev.*, 50(2):197–263, June 1998.

[5] A Ashkin. Forces of a single-beam gradient laser trap on a dielectric sphere in the ray optics regime. *Biophys. J.*, 61(2):569–582, February 1992.

[6] A Ashkin, JM Dziedzic, JE Bjorkholm, and S Chu. Observation of a single-beam gradient force optical trap for dielectric particles. *Opt. Lett.*, 11(5):288–290, May 1986.

[7] T F Bartsch, S Fisinger, M D Kochanczyk, R Huang, A Jonás, and E-L Florin. Detecting sequential bond formation using three-dimensional thermal fluctuation analysis. *ChemPhysChem*, 10(9-10):1541–1547, July 2009.

[8] A R Bausch and K Kroy. A bottom-up approach to cell mechanics. *Nat. Phys.*, 2:231–238, April 2006.

[9] P M Bendix and L B Oddershede. Expanding the Optical Trapping Range of Lipid Vesicles to the Nanoscale. *Nano lett.*, 11(12):5431–5437, December 2011.

[10] K Berg-Sørensen and H Flyvbjerg. Power spectrum analysis for optical tweezers. *Rev. Sci. Instrum.*, 75(3):594–612, March 2004.

[11] D E Birk, J M Fitch, J P Babiarz, K J Doane, and T F Linsenmayer. Collagen fibrillogenesis in vitro: interaction of types I and V collagen regulates fibril diameter. *J. Cell. Sci.*, 95(Pt 4):649–657, April 1990.

[12] D E Birk, J F Southern, E I Zycband, J T Fallon, and R L Trelstad. Collagen fibril bundles: a branching assembly unit in tendon morphogenesis. *Development.*, 107(3):437–443, November 1989.

[13] A Blocker, F F Severin, J K Burkhardt, J B Bingham, H Yu, J C Olivo, T A Schroer, A A Hyman, and G Griffiths. Molecular requirements for bi-directional movement of phagosomes along microtubules. *J. Cell. Biol.*, 137(1):113–129, April 1997.

[14] T P Burghardt and D Axelrod. Total internal reflection/fluorescence photobleaching recovery study of serum albumin adsorption dynamics. *Biophys. J.*, 33(3):455, March 1981.

[15] K G Campellone, N J Webb, E A Znameroski, and M D Welch. WHAMM Is an Arp2/3 Complex Activator That Binds Microtubules and Functions in ER to Golgi Transport. *Cell*, 134(1):148–161, July 2008.

[16] N O Carragher and M C Frame. Focal adhesion and actin dynamics: a place where kinases and proteases meet to promote invasion. *Trends Cell Biol.*, 14(5):241–249, May 2004.

[17] S Cermelli, Y Guo, S P Gross, and M A Welte. The lipid-droplet proteome reveals that droplets are a protein-storage depot. *Curr. Biol.*, 16(18):1783–1795, September 2006.

[18] S Chandrasekhar. Stochastic problems in physics and astronomy. *Rev. Mod. Phys.*, 15(1):1–89, 1943.

[19] H J Clercx and P P Schram. Brownian particles in shear flow and harmonic potentials: A study of long-time tails. *Phys. Rev. A*, 46(4):1942–1950, August 1992.

[20] R G Cox. The motion of long slender bodies in a viscous fluid. Part 1. General theory. *J. Fluid Mech.*, 44(4):791–810, December 1970.

[21] T L Culver-Hanlon, S A Lex, A D Stephens, N J Quintyne, and S J King. A microtubule-binding domain in dynactin increases dynein processivity by skating along microtubules. *Nat. Cell Biol.*, 8(3):264–270, March 2006.

[22] S W Deacon, A S Serpinskaya, P S Vaughan, M Lopez Fanarraga, I Vernos, K T Vaughan, and V I Gelfand. Dynactin is required for bidirectional organelle transport. *J. Cell Biol.*, 160(3):297–301, February 2003.

[23] W Demtröder. *Experimentalphysik 2.* Elektrizität und Optik. Springer, 2nd edition, 2008.

[24] A Desai and T J Mitchison. Microtubule polymerization dynamics. *Annu. Rev. Cell Dev. Biol.*, 13:83–117, November 1997.

[25] G A Di Lullo, S M Sweeney, J Korkko, L Ala-Kokko, and J D San Antonio. Mapping the ligand-binding sites and disease-associated mutations on the most abundant protein in the human, type I collagen. *J. Biol. Chem.*, 277(6):4223–4231, February 2002.

[26] H Dietz and M Rief. Elastic Bond Network Model for Protein Unfolding Mechanics. *Phys. Rev. Lett.*, 100(9):1–4, March 2008.

[27] D E Discher, P Janmey, and Y Wang. Tissue Cells Feel and Respond to the Stiffness of Their Substrate. *Science*, 310(5751):1139–1143, November 2005.

[28] S Dixit, M Singh-Zocchi, J Hanne, and G Zocchi. Mechanics of Binding of a Single Integration-Host-Factor Protein to DNA. *Phys. Rev. Lett.*, 94(11):118101, March 2005.

[29] C G dos Remedios, D Chhabra, M Kekic, I V Dedova, M Tsubakihara, D A Berry, and N J Nosworthy. Actin binding proteins: regulation of cytoskeletal microfilaments. *Physiol. Rev.*, 83(2):433–473, April 2003.

[30] G Drewes, A Ebneth, and E M Mandelkow. MAPs, MARKs and microtubule dynamics. *Trends Biochem. Sci.*, 23(8):307–311, August 1998.

[31] L Edelstein-Keshet and G B Ermentrout. Models for the length distributions of actin filaments: I. Simple polymerization and fragmentation. *Bull. Math. Biol.*, 60(3):449–475, May 1998.

[32] E F Eikenberry, B B Brodsky, and A S Craig. Collagen fibril morphology in developing chick metatarsal tendon: 2. Electron microscope studies. *Int. J. Biol. Macromolec.*, 4(7):393–398, December 1982.

[33] K Eom, P Li, D Makarov, and G Rodin. Relationship between the Mechanical Properties and Topology of Cross-Linked Polymer Molecules: Parallel Strands Maximize the Strength of Model Polymers and Protein Domains. *J. Phys. Chem. B*, 107(34):8730–8733, August 2003.

[34] E Eyal and I Bahar. Toward a Molecular Understanding of the Anisotropic Response of Proteins to External Forces: Insights from Elastic Network Models. *Biophys. J.*, 94(9):3424–3435, May 2008.

[35] D R Eyre and J-J Wu. Collagen Cross-Links. *Top. Curr. Chem.*, 247:207–229, 2005.

[36] H Felgner, R Frank, and M Schliwa. Flexural rigidity of microtubules measured with the use of optical tweezers. *J. Cell Sci.*, 109(2):509–516, February 1996.

[37] D A Fletcher and R D Mullins. Cell mechanics and the cytoskeleton. *Nature*, 463(7280):485–492, January 2010.

[38] E-L Florin, V Moy, and H Gaub. Adhesion forces between individual ligand-receptor pairs. *Science*, 264(5157):415–417, April 1994.

[39] E-L Florin, A Pralle, E Stelzer, and J Hörber. Photonic force microscope calibration by thermal noise analysis. *Appl. Phys. A*, 66(1):S75–S78, 1998.

[40] D Ganic, X Gan, and M Gu. Exact radiation trapping force calculation based on vectorial diffraction theory. *Opt. Express*, 12(12):2670–2675, June 2004.

[41] M K Gardner, A J Hunt, H V Goodson, and D J Odde. Microtubule assembly dynamics: new insights at the nanoscale. *Curr. Opin. Cell. Biol.*, 20(1):64–70, February 2008.

[42] A Gautieri, S Vesentini, A Redaelli, and M J Buehler. Hierarchical structure and nanomechanics of collagen microfibrils from the atomistic scale up. *Nano lett.*, 11(2):757–766, February 2011.

[43] A Gholami, J Wilhelm, and E Frey. Entropic forces generated by grafted semiflexible polymers. *Phys. Rev. E*, 74(4):041803, October 2006.

[44] F Gittes, B Mickey, J Nettleton, and J Howard. Flexural rigidity of microtubules and actin filaments measured from thermal fluctuations in shape. *J. Cell Biol.*, 120(4):923–934, February 1993.

[45] N M Green. Avidin. *Adv. Protein Chem.*, 29:85–133, 1975.

[46] S P Gross. Hither and yon: a review of bi-directional microtubule-based transport. *Phys. Biol.*, 1(2):R1–R11, June 2004.

[47] S P Gross, M A Welte, S M Block, and E F Wieschaus. Dynein-mediated cargo transport in vivo. A switch controls travel distance. *J. Cell. Biol.*, 148(5):945–956, March 2000.

[48] H Grubmüller, B Heymann, and P Tavan. Ligand binding: molecular mechanics calculation of the streptavidin-biotin rupture force. *Science*, 271(5251):997, February 1996.

[49] K Y Han, K I Willig, E Rittweger, F Jelezko, C Eggeling, and S W Hell. Three-Dimensional Stimulated Emission Depletion Microscopy of Nitrogen-Vacancy Centers in Diamond Using Continuous-Wave Light. *Nano Lett.*, 9(9):3323–3329, September 2009.

[50] J Happel and H Brenner. *Low Reynolds number hydrodynamics: with special applications to particulate media.* Martinus Nijhoff Publishers, The Hague, 1983.

[51] Y Harada and T Asakura. Radiation forces on a dielectric sphere in the Rayleigh scattering regime. *Opt. Commun.*, 124(5-6):1–13, March 1996.

[52] A G Hendricks, E L F Holzbaur, and Y E Goldman. Force measurements on cargoes in living cells reveal collective dynamics of microtubule motors. *PNAS*, 109(45):18447–18452, November 2012.

[53] A G Hendricks, E Perlson, J L Ross, H W Schroeder, M Tokito, and E L F Holzbaur. Motor coordination via a tug-of-war mechanism drives bidirectional vesicle transport. *Curr. Biol.*, 20(8):697–702, April 2010.

[54] C Heussinger and E Frey. Stiff Polymers, Foams, and Fiber Networks. *Phys. Rev. Lett.*, 96(1):017802, January 2006.

[55] D F Holmes, M J Capaldi, and J A Chapman. Reconstitution of collagen fibrils in vitro; the assembly process depends on the initiating procedure. *Int. J. Biol. Macromolec.*, 8(3):161–166, June 1986.

[56] R Huang. *Brownian Motion at Fast Time Scales and Thermal Noise Imaging.* PhD thesis, The University of Texas at Austin, 2008.

[57] R Huang, I Chavez, K M Taute, B Lukić, S Jeney, M G Raizen, and E-L Florin. Direct observation of the full transition from ballistic to diffusive Brownian motion in a liquid. *Nat. Phys.*, 7(7):576–580, March 2011.

[58] H E Huxley. Past, present and future experiments on muscle. *Philos. Trans. R. Soc. Lond. B Biol. Sci.*, 355(1396):539–543, April 2000.

[59] S Izrailev, S Stepaniants, M Balsera, and Y Oono. Molecular dynamics study of unbinding of the avidin-biotin complex. *Biophys. J.*, 72(4):1568–1581, April 1997.

[60] J D Jackson. *Classical Electrodynamics.* John Wiley & Sons, 3rd edition, January 2007.

[61] P A Janmey and D A Weitz. Dealing with mechanics: mechanisms of force transduction in cells. *Trends Biochem. Sci.*, 29(7):364–370, July 2004.

[62] P A Janmey, J P Winer, M E Murray, and Q Wen. The hard life of soft cells. *Cell. Motil. Cytoskeleton.*, 66(8):597–605, August 2009.

[63] M E Janson and M Dogterom. A Bending Mode Analysis for Growing Microtubules: Evidence for a Velocity-Dependent Rigidity. *Biophys. J.*, 87(4):2723–2736, October 2004.

[64] S Jeney, E Stelzer, H Grubmuller, and E-L Florin. Mechanical properties of single motor molecules studied by three-dimensional thermal force probing in optical tweezers. *ChemPhysChem*, 5(8):1150–1158, August 2004.

[65] K E Kadler, Y Hojima, and D J Prockop. Collagen fibrils in vitro grow from pointed tips in the C- to N-terminal direction. *Biochem. J.*, 268(2):339, June 1990.

[66] K E Kadler, D F Holmes, J A Trotter, and J A Chapman. Collagen fibril formation. *Biochem. J.*, 316(1):1–11, May 1996.

[67] J Käs, H Strey, J X Tang, D Finger, R Ezzell, E Sackmann, and P A Janmey. F-actin, a model polymer for semiflexible chains in dilute, semidilute, and liquid crystalline solutions. *Biophys. J.*, 70(2):609–625, February 1996.

[68] L J Kaufman, C P Brangwynne, K E Kasza, E Filippidi, V D Gordon, T S Deisboeck, and D A Weitz. Glioma expansion in collagen I matrices: analyzing collagen concentration-dependent growth and motility patterns. *Biophys. J.*, 89(1):635–650, July 2005.

[69] F W Keeley, C M Bellingham, and K A Woodhouse. Elastin as a self-organizing biomaterial: use of recombinantly expressed human elastin polypeptides as a model for investigations of structure and self-assembly of elastin.
Philos. Trans. R. Soc. Lond. B Biol. Sci., 357(1418):185–189, February 2002.

[70] S J King and T A Schroer. Dynactin increases the processivity of the cytoplasmic dynein motor. *Nat. Cell Biol.*, 2(1):20–24, January 2000.

[71] M D Kochanczyk. *Development of Quantitative Three-Dimensional Thermal Noise Imaging of Biopolymer Filaments.* PhD thesis, The University of Texas at Austin, 2012.

[72] M D Kochanczyk, T F Bartsch, K M Taute, and E-L Florin. Power spectral density integration analysis and its application to large bandwidth, high precision position measurements. In *SPIE NanoScience + Engineering*, page 84580H. SPIE, September 2012.

[73] L Le Goff, O Hallatschek, E Frey, and F Amblard. Tracer Studies on F-Actin Fluctuations. *Phys. Rev. Lett.*, 89(25):258101, December 2002.

[74] G U Lee, D A Kidwell, and R J Colton. Sensing Discrete Streptavidin-Biotin Interactions with Atomic Force Microscopy. *Langmuir*, 10(2):354–357, February 1994.

[75] C Leidel, R A Longoria, F M Gutierrez, and G T Shubeita. Measuring molecular motor forces in vivo: implications for tug-of-war models of bidirectional transport. *Biophys. J.*, 103(3):492–500, August 2012.

[76] J R Levy and E L F Holzbaur. Cytoplasmic dynein/dynactin function and dysfunction in motor neurons. *Int. J. Dev. Neurosci.*, 24(2-3):103--111, April 2006.

[77] J-T Li, K D Caldwell, and N Rapoport. Surface Properties of Pluronic-Coated Polymeric Colloids. *Langmuir*, 10(12):4475–4482, December 1994.

[78] S Lindström, D Vader, A Kulachenko, and D Weitz. Biopolymer network geometries: Characterization, regeneration, and elastic properties. *Phys. Rev. E*, 82(5):051905, November 2010.

[79] X Liu, Y Zhou, H Gao, and J Wang. Anomalous Flexural Behaviors of Microtubules. *Biophys. J.*, 102(8):1793–1803, April 2012.

[80] B Lukić, S Jeney, Ž Sviben, A Kulik, E-L Florin, and L Forro. Motion of a colloidal particle in an optical trap. *Phys. Rev. E*, 76(1):011112, July 2007.

[81] E Mandelkow and E M Mandelkow. Microtubules and microtubule-associated proteins. *Curr. Opin. Cell. Biol.*, 7(1):72–81, February 1995.

[82] A Meller, R Bar-Ziv, T Tlusty, E Moses, J Stavans, and S A Safran. Localized Dynamic Light Scattering: A New Approach to Dynamic Measurements in Optical Microscopy. *Biophys. J.*, 74(3):1541–1548, March 1998.

[83] R Merkel, P Nassoy, A Leung, K Ritchie, and E Evans. Energy landscapes of receptor-ligand bonds explored with dynamic force spectroscopy. *Nature*, 397(6714):50–53, January 1999.

[84] W Mickel, S Munster, L M Jawerth, D A Vader, D A Weitz, A P Sheppard, K Mecke, B Fabry, and G E Schroder-Turk. Robust pore size

analysis of filamentous networks from three-dimensional confocal microscopy. *Biophys. J.*, 95(12):6072–6080, December 2008.

[85] D Mizuno, C Tardin, C F Schmidt, and F C MacKintosh. Nonequilibrium mechanics of active cytoskeletal networks. *Science*, 315(5810):370–373, January 2007.

[86] S M Moghimi and A C Hunter. Poloxamers and poloxamines in nanoparticle engineering and experimental medicine. *Trends Biotechnol.*, 18(10):412–420, October 2000.

[87] V Moy, E-L Florin, and H Gaub. Intermolecular forces and energies between ligands and receptors. *Science*, 266(5183):257–259, October 1994.

[88] N Mücke, L Kreplak, R Kirmse, T Wedig, H Herrmann, U Aebi, and J Langowski. Assessing the flexibility of intermediate filaments by atomic force microscopy. *J. Mol. Biol.*, 335(5):1241–1250, January 2004.

[89] K Murakami, T Yasunaga, T Q Noguchi, Y Gomibuchi, K X Ngo, T Q Uyeda, and T Wakabayashi. Structural basis for actin assembly, activation of ATP hydrolysis, and delayed phosphate release. *Cell*, 143(2):275–287, October 2010.

[90] J W Murray, E Bananis, and A W Wolkoff. Reconstitution of ATP-dependent Movement of Endocytic Vesicles Along Microtubules In Vitro:

An Oscillatory Bidirectional Process. *Mol. Biol. Cell*, 11(2):419–433, February 2000.

[91] K Neuman, E Chadd, G Liou, K Bergman, and S M Block. Characterization of photodamage to Escherichia coli in optical traps. *Biophys. J.*, 77(5):2856–2863, November 1999.

[92] A A R Neves, A Camposeo, S Pagliara, R Saija, F Borghese, P Denti, M A Iatì, R Cingolani, O M Maragò, and D Pisignano. Rotational dynamics of optically trapped nanofibers. *Opt. Express*, 18(2):822–830, January 2010.

[93] T Nishida, K Yasumoto, T Otori, and J Desaki. The network structure of corneal fibroblasts in the rat as revealed by scanning electron microscopy. *Invest. Ophthalmol. Vis. Sci.*, 29(12):1887–1890, December 1988.

[94] F Oosawa and M Kasai. A theory of linear and helical aggregations of macromolecules. *J. Mol. Biol.*, 4:10–21, January 1962.

[95] F Pampaloni and E-L Florin. Microtubule architecture: inspiration for novel carbon nanotube-based biomimetic materials. *Trends Biotechnol.*, 26(6):302–310, June 2008.

[96] F Pampaloni, G Lattanzi, A Jonas, T Surrey, E Frey, and E Florin. Thermal fluctuations of grafted microtubules provide evidence of a

length-dependent persistence length. *PNAS*, 103(27):10248–10253, July 2006.

[97] R J Pelham and Y l Wang. Cell locomotion and focal adhesions are regulated by substrate flexibility. *PNAS*, 94(25):13661–13665, December 1997.

[98] J C Phillips and G J Mattamal. Effect of number of carboxyl groups on liquid density of esters of alkylcarboxylic acids. *J. Chem. Eng. Data*, 23(1):1–6, January 1978.

[99] N Pollock, M P Koonce, E L de Hostos, and R D Vale. In vitro microtubule-based organelle transport in wild-type Dictyostelium and cells overexpressing a truncated dynein heavy chain. *Cell Motil. Cytoskeleton*, 40(3):304–314, 1998.

[100] A Pralle, E-L Florin, E H K Stelzer, and J K H Hörber. Local viscosity probed by photonic force microscopy. *Appl. Phys. A*, 66(1):S71–S73, March 1998.

[101] A Pralle, P Keller, E Florin, K Simons, and J K H Horber. Sphingolipid-Cholesterol Rafts Diffuse as Small Entities in the Plasma Membrane of Mammalian Cells. *J. Cell Biol.*, 148(5):997–1008, March 2000.

[102] A Pralle, M Prummer, E-L Florin, E H Stelzer, and J K H Hörber. Three-dimensional high-resolution particle tracking for optical tweezers

by forward scattered light. *Microsc. Res. Tech.*, 44(5):378–386, February 1999.

[103] L Pugliese, A Coda, M Malcovati, and M Bolognesi. Three-dimensional structure of the tetragonal crystal form of egg-white avidin in its functional complex with biotin at 2.7 A resolution.
J. Mol. Biol., 231(3):698–710, June 1993.

[104] J Quispe, J Damiano, S E Mick, D P Nackashi, D Fellmann, T G Ajero, B Carragher, and C S Potter. An improved holey carbon film for cryo-electron microscopy. *Microsc. Microanal.*, 13(5):365–371, October 2007.

[105] V H Ramey, H-W Wang, Y Nakajima, A Wong, J Liu, D Drubin, G Barnes, and E Nogales. The Dam1 ring binds to the E-hook of tubulin and diffuses along the microtubule. *Mol. Biol. Cell*, 22(4):457–466, February 2011.

[106] V Redeker, R Melki, D Promé, J P Le Caer, and J Rossier. Structure of tubulin C-terminal domain obtained by subtilisin treatment. The major alpha and beta tubulin isotypes from pig brain are glutamylated. *FEBS letters*, 313(2):185–192, November 1992.

[107] F Reif. *Fundamentals of Statistical and Thermal Physics.* Waveland Pr Inc, December 2008.

[108] C A Reinhart-King, M Dembo, and D A Hammer. Cell-cell mechanical communication through compliant substrates. *Biophysical Journal*,

95(12):6044–6051, December 2008.

[109] B Richards and E Wolf. Electromagnetic Diffraction in Optical Systems. II. Structure of the Image Field in an Aplanatic System. *Proc. R. Soc. A*, 253(1274):358–379, December 1959.

[110] S L Rogers, I S Tint, P C Fanapour, and V I Gelfand. Regulated bidirectional motility of melanophore pigment granules along microtubules in vitro. *PNAS*, 94(8):3720–3725, April 1997.

[111] A Rohrbach. Stiffness of optical traps: quantitative agreement between experiment and electromagnetic theory. *Phys. Rev. Lett.*, 95(16): 168102, October 2005.

[112] A Rohrbach and E H K Stelzer. Optical trapping of dielectric particles in arbitrary fields. *J. Opt. Soc. Am. A*, 18(4):839–853, April 2001.

[113] A Rohrbach and E H K Stelzer. Three-dimensional position detection of optically trapped dielectric particles. *J. Appl. Phys.*, 91(8):5474–5488, January 2002.

[114] A Rohrbach and E H K Stelzer. Trapping forces, force constants, and potential depths for dielectric spheres in the presence of spherical aberrations. *Appl. Opt.*, 41(13):2494–2507, May 2002.

[115] M Rubinstein and R H Colby. *Polymer Physics*. Oxford University Press, USA, 2003.

[116] E Schaffer, S Norrelykke, and J Howard. Surface forces and drag coefficients of microspheres near a plane surface measured with optical tweezers. *Langmuir*, 23(7):3654–3665, March 2007.

[117] M Schliwa and G Woehlke. Molecular motors. *Nature*, 422(6933):759–765, April 2003.

[118] C A Schneider, W S Rasband, and K W Eliceiri. NIH Image to ImageJ: 25 years of image analysis. *Nat. Methods*, 9(7):671–675, July 2012.

[119] M J Schnitzer and S M Block. Kinesin hydrolyses one ATP per 8-nm step. *Nature*, 388(6640):386–390, July 1997.

[120] T Scholz, S M Altmann, M Antognozzi, C Tischer, J K H Horber, and B Brenner. Mechanical Properties of Single Myosin Molecules Probed with the Photonic Force Microscope. *Biophys. J.*, 88(1):360–371, January 2005.

[121] K Schulten and I Kosztin. *Lectures in Theoretical Biophysics*. University of Illinois at Urbana-Champaign, April 2000.

[122] J E Seebergh and J C Berg. Evidence of a hairy layer at the surface of polystyrene latex particles. *Colloids Surf. A Physicochem. Eng. Asp.*, 100:139–153, July 1995.

[123] P C Seitz, E H K Stelzer, and A Rohrbach. Interferometric tracking of optically trapped probes behind structured surfaces: a phase correction method. *Appl. Opt.*, 45(28):7309–7315, October 2006.

[124] M K Shaw, H L Compton, D S Roos, and L G Tilney. Microtubules, but not actin filaments, drive daughter cell budding and cell division in Toxoplasma gondii. *J. Cell Sci*, 113(7):1241–1254, April 2000.

[125] G T Shubeita, S L Tran, J Xu, M Vershinin, and S Cermelli. Consequences of Motor Copy Number on the Intracellular Transport of Kinesin-1-Driven Lipid Droplets. *Cell*, 135(6):1098–1107, December 2008.

[126] P A Sims and X S Xie. Probing Dynein and Kinesin Stepping with Mechanical Manipulation in a Living Cell. *ChemPhysChem*, 10(9-10):1511–1516, July 2009.

[127] M Singh-Zocchi, S Dixit, V Ivanov, and G Zocchi. Single-molecule detection of DNA hybridization. *PNAS*, 100(13):7605–7610, May 2003.

[128] S B Smith, L Finzi, and C Bustamante. Direct mechanical measurements of the elasticity of single DNA molecules by using magnetic beads. *Science*, 258(5085):1122–1126, November 1992.

[129] V Soppina, A K Rai, A J Ramaiya, P Barak, and R Mallik. Tug-of-war between dissimilar teams of microtubule motors regulates transport and fission of endosomes. *PNAS*, 106(46):19381–19386, November 2009.

[130] M Sotomayor and K Schulten. Single-molecule experiments in vitro and in silico. *Science*, 316(5828):1144–1148, May 2007.

[131] E Stern, R Wagner, F J Sigworth, R Breaker, T M Fahmy, and M A Reed. Importance of the Debye screening length on nanowire field effect transistor sensors. *Nano Lett.*, 7(11):3405–3409, November 2007.

[132] C Storm, J J Pastore, F C MacKintosh, T C Lubensky, and P A Janmey. Nonlinear elasticity in biological gels. *Nature*, 435(7039):191–194, May 2005.

[133] T P Straatsma, H J C Berendsen, and A J Stam. Estimation of statistical errors in molecular simulation calculations. *Mol. Phys.*, 57(1):89–95, January 1986.

[134] K Svoboda and S M Block. Force and velocity measured for single kinesin molecules. *Cell*, 77(5):773–784, June 1994.

[135] K Taute, F Pampaloni, E Frey, and E-L Florin. Microtubule Dynamics Depart from the Wormlike Chain Model. *Phys. Rev. Lett.*, 100(2):028102, January 2008.

[136] R Timpl, H Rohde, P G Robey, S I Rennard, J M Foidart, and G R Martin. Laminin–a glycoprotein from basement membranes. *J. Biol. Chem.*, 254(19):9933–9937, October 1979.

[137] C Tischer, S Altmann, S Fisinger, J K H Hörber, and E-L Florin. Three-dimensional thermal noise imaging. *Appl. Phys. Lett.*, 79(23):3878--3881, September 2001.

[138] C Tischer, A Pralle, and E-L Florin. Determination and Correction of Position Detection Nonlinearity in Single Particle Tracking and Three-Dimensional Scanning Probe Microscopy. *Microsc. Microanal.*, 10(04):1–10, August 2004.

[139] S F Tolić-Nørrelykke, E Schäffer, J Howard, F S Pavone, F Jülicher, and H Flyvbjerg. Calibration of optical tweezers with positional detection in the back focal plane. *Rev. Sci. Instrum.*, 77(10):103101, 2006.

[140] X Trepat, M Grabulosa, L Buscemi, F Rico, B Fabry, J J Fredberg, and R Farré. Oscillatory magnetic tweezers based on ferromagnetic beads and simple coaxial coils. *Rev. Sci. Instrum.*, 74(9):4012, September 2003.

[141] G Uhlenbeck and L Ornstein. On the Theory of the Brownian Motion. *Phys. Rev.*, 36(5):823–841, September 1930.

[142] D Vader, A Kabla, D Weitz, and L Mahadevan. Strain-Induced Alignment in Collagen Gels. *PLoS ONE*, 4(6):e5902, June 2009.

[143] R D Vale. The molecular motor toolbox for intracellular transport. *Cell*, 112(4):467–480, February 2003.

[144] S VandeVondele, J Vörös, and J A Hubbell. RGD-grafted poly-L-lysine-graft-(polyethylene glycol) copolymers block non-specific protein adsorption while promoting cell adhesion. *Biotechnol. Bioeng.*, 82(7):784–790, June 2003.

[145] R B Vernon and E H Sage. Contraction of fibrillar type I collagen by endothelial cells: A study in vitro. *J. Cell Biochem.*, 60(2):185–197, February 1998.

[146] M Wang and G Uhlenbeck. On the Theory of the Brownian Motion II. *Rev. Mod. Phys.*, 17(2-3):323–342, April 1945.

[147] C Weaver, C Leidel, L Szpankowski, N M Farley, G T Shubeita, and L S B Goldstein. Endogenous GSK-3/Shaggy Regulates Bidirectional Axonal Transport of the Amyloid Precursor Protein. *Traffic*, 14(3):295–308, March 2013.

[148] M A Welte. Bidirectional Transport along Microtubules. *Curr. Biol.*, 14(13):R525–R537, July 2004.

[149] M A Welte. Proteins under new management: lipid droplets deliver. *Trends Cell Biol.*, 17(8):363–369, August 2007.

[150] C H Wiggins, D Riveline, A Ott, and R E Goldstein. Trapping and Wiggling: Elastohydrodynamics of Driven Microfilaments. *Biophys. J.*, 74(2):1043–1060, February 1998.

[151] J Wilhelm and E Frey. Radial distribution function of semiflexible polymers. *Phys. Rev. Lett.*, 77(12):2581–2584, 1996.

[152] J Wilhelm and E Frey. Elasticity of Stiff Polymer Networks. *Phys. Rev. Lett.*, 91(10):108103, September 2003.

[153] T Wittmann and C M Waterman-Storer. Cell motility: can Rho GTPases and microtubules point the way? *J. Cell Sci.*, 114(21):3795–3803, November 2001.

[154] G C Wood and M K Keech. The formation of fibrils from collagen solutions 1. The effect of experimental conditions: kinetic and electron-microscope studies. *Biochem. J.*, 75(3):588–598, June 1960.

[155] A K Wright and M R Thompson. Hydrodynamic structure of bovine serum albumin determined by transient electric birefringence. *Biophys. J.*, 15(2 Pt 1):137–141, February 1975.

[156] K Xu, H P Babcock, and X Zhuang. Dual-objective STORM reveals three-dimensional filament organization in the actin cytoskeleton. *Nat. Methods*, 9(2):185–188, February 2012.

[157] H Yamakawa. *Modern theory of polymer solutions.* Harper and Row, 1971.

[158] L Yang, K O van der Werf, C F C Fitié, M L Bennink, P J Dijkstra, and J Feijen. Mechanical properties of native and cross-linked type I collagen fibrils. *Biophys. J.*, 94(6):2204–2211, March 2008.

[159] G Zocchi. Mechanical measurement of the unfolding of a protein. *Europhys. Lett.*, 35(8):633, September 1996.

Vita

Tobias Fabian Bartsch was born in Munich, Germany in 1983. After graduating from the Ludwig-Thoma-Gymnasium in Prien am Chiemsee in 2002, he started studying physics at the Julius-Maximilians-Universitaet in Wuerzburg, Germany. He passed the Vordiplom in 2004 “sehr gut” (very good). In 2005, he applied for enrollment in the graduate physics program at the University of Texas at Austin as an exchange student. He was accepted and started studies the same year. After receiving a Master’s degree in December 2006 he briefly conducted research in molecular physics at the Technical University of Berlin, Germany, before returning to the University of Texas at Austin in June 2007 to pursue a PhD in physics.

E-mail: tobias.bartsch@utexas.edu

This dissertation was typeset with LaTeX[†] by the author.

[†] LaTeX is a document preparation system developed by Leslie Lamport as a special version of Donald Knuth’s TeX Program.